NASA/TM-20250003807



Prediction Uncertainty Reduction Tech Challenge: Final Report

James Bridges and David B. Stephens
Glenn Research Center, Cleveland, Ohio

Gerrit-Daniel Stich
Analytical Mechanics Associates, Inc., Mountain View, California

Gregory R. Busch
Glenn Research Center, Cleveland, Ohio

Mehdi R. Khorrami
NASA Langley Research Center, Hampton, Virginia

Brenda S. Henderson, Edmane Envia, Alexander A. Svetgoff, William V. Banks, and Khairul Zaman
Glenn Research Center, Cleveland, Ohio

June 2025

NASA STI Program Report Series

Since its founding, NASA has been dedicated to the advancement of aeronautics and space science. The NASA scientific and technical information (STI) program plays a key part in helping NASA maintain this important role.

The NASA STI program operates under the auspices of the Agency Chief Information Officer. It collects, organizes, provides for archiving, and disseminates NASA's STI. The NASA STI program provides access to the NTRS Registered and its public interface, the NASA Technical Reports Server, thus providing one of the largest collections of aeronautical and space science STI in the world. Results are published in both non-NASA channels and by NASA in the NASA STI Report Series, which includes the following report types:

- TECHNICAL PUBLICATION.
  Reports of completed research or a major significant phase of research that present the results of NASA programs and include extensive data or theoretical analysis. Includes compilations of significant scientific and technical data and information deemed to be of continuing reference value. NASA counterpart of peer-reviewed formal professional papers but has less stringent limitations on manuscript length and extent of graphic presentations.

- TECHNICAL MEMORANDUM.
  Scientific and technical findings that are preliminary or of specialized interest, e.g., quick release reports, working papers, and bibliographies that contain minimal annotation. Does not contain extensive analysis.

- CONTRACTOR REPORT.
  Scientific and technical findings by NASA-sponsored contractors and grantees.

- CONFERENCE PUBLICATION.
  Collected papers from scientific and technical conferences, symposia, seminars, or other meetings sponsored or cosponsored by NASA.

- SPECIAL PUBLICATION.
  Scientific, technical, or historical information from NASA programs, projects, and missions, often concerned with subjects having substantial public interest.

- TECHNICAL TRANSLATION.
  English-language translations of foreign scientific and technical material pertinent to NASA's mission.

Specialized services also include organizing and publishing research results, distributing specialized research announcements and feeds, providing information desk and personal search support, and enabling data exchange services.

For more information about the NASA STI program, see the following:

- Access the NASA STI program home page at http://www.sti.nasa.gov

NASA/TM-20250003807



Prediction Uncertainty Reduction Tech Challenge: Final Report

James Bridges and David B. Stephens
Glenn Research Center, Cleveland, Ohio

Gerrit-Daniel Stich
Analytical Mechanics Associates, Inc., Mountain View, California

Gregory R. Busch
Glenn Research Center, Cleveland, Ohio

Mehdi R. Khorrami
NASA Langley Research Center, Hampton, Virginia

Brenda S. Henderson, Edmane Envia, Alexander A. Svetgoff, William V. Banks, and Khairul Zaman
Glenn Research Center, Cleveland, Ohio

National Aeronautics and
Space Administration

Glenn Research Center
Cleveland, Ohio 44135

June 2025

Acknowledgments

This work was supported by NASA's Commercial Supersonic Technology Project.

Trade names and trademarks are used in this report for identification only. Their usage does not constitute an official endorsement, either expressed or implied, by the National Aeronautics and Space Administration.

Level of Review: This material has been technically reviewed by technical management.

This report is available in electronic form at https://www.sti.nasa.gov/ and https://ntrs.nasa.gov/

NASA STI Program/Mail Stop 050
NASA Langley Research Center
Hampton, VA 23681-2199

Executive Summary

In 2018, several companies were requesting that the Federal Aviation Administration (FAA) establish a regulation for certifying commercial supersonic aircraft, including their noise during landing and takeoff (LTO). Regulators, having no technical data to judge reasonable noise levels for such aircraft, were turning to NASA and other experts to use their noise prediction models to guide the formulation of such regulations. Ultimately, a Notice of Proposed Rulemaking was released by the FAA, largely based on studies using the best prediction methods available. However, during these studies it became clear that the uncertainty in aircraft noise predictions, when applied to supersonic vehicles, was much greater than what regulators were accustomed to, leaving the regulators on shaky ground in making new noise rules.

As a result of a January 2021 Tollgate review, the Advanced Air Vehicles Program approved a new Technical Challenge (TC) to be run out of the Commercial Supersonic Technology (CST) Project. The TC was called "Prediction Uncertainty Reduction (PUR)." The final TC statement was *"Produce data and demonstrate tools that reduce the uncertainty in predicting Landing & Takeoff Noise levels of supersonic-relevant designs by 5 EPNdB and are ready for use in studies to inform FAA rule-making."*

During the 90-day initial baseline Uncertainty Quantification study that followed, a key performance metric and Progress Indicator was created and approved by the Program. The key performance metric was the cumulative error in predicting the certification noise levels of propulsion components appropriate for supersonic flight as they impacted the total aircraft noise. It was shown that when this metric was applied to conventional aircraft, such as the 737-800, the cumulative error was 1.5 EPNdB; when applied to the study vehicle being used in International Civil Aviation Organization studies of supersonic noise regulations, the cumulative error was 7.8 EPNdB. The TC goal of 5 EPNdB reduction would bring the uncertainty of predicting supersonic aircraft noise to nearly as low as that of predicting conventional aircraft.

To make the required improvements in noise prediction methods for supersonic aircraft, noise data for supersonic configurations would need to be acquired. Historically, this was done using scale-model testing. However, there was neither time nor budget for these tests, estimated to cost $30 to 40M and requiring 10 years to complete. Instead, NASA decided to validate and use high-fidelity numerical simulations to acquire the needed noise data. Such simulation tools have been in development by NASA for several decades. For fan noise, Unsteady Reynolds Average Navier-Stokes (URANS) numerical codes specialized for turbomachinery are now available from commercial vendors, along with codes that compute acoustic propagation in complex geometries using linearized Euler equations. For jets, large-eddy simulation methods compute the unsteady motions of a jet plume to the smallest scales needed for acoustics and recently have successfully simulated scale-model experiments. Of course, before using the results of the simulations, the uncertainties of the simulation methods would be assessed as part of the TC.

High-fidelity simulations require high-fidelity designs. For the fan noise component, NASA procured the design of a two-stage propulsor behind a supersonic inlet designed by General Electric Aviation. The design captures much of the company's expertise being concurrently applied to a commercial product for the supersonic market. For the jet noise component, NASA used the design guidance acquired from recent contracts with General Electric (GE) and Rolls-Royce to design its own internally mixed, variable geometry exhaust system.

For validation of the simulation methods, NASA used existing noise data acquired in its 9- by 15-Foot Low-Speed Wind Tunnel and Aero-Acoustic Propulsion Laboratory for conventional aircraft configurations. For both fan and jet noise methods, the model-scale data was simulated and deviations from measured data were quantified for a range of flow conditions to establish the validity of the

methods. For the fan, the discrepancies with rig data for tone power had a 7.3 dB standard deviation; fan test repeatability for the same rig in the same facility had a standard deviation of 1.3 dB. In the baseline uncertainty assessment, the fan models had a deviation of 9.5 dB. For the jet, the discrepancies with rig data had a standard deviation of 0.72 EPNdB, comparable to the discrepancies between different physical rig tests (0.96 EPNdB). This work was reviewed by an outside panel of experts, who concurred with NASA's assessment of the simulation errors.

The high-fidelity simulation methods were then used on the supersonic configurations under the assumption that the physics embodied by the simulation tools were the same for both conventional and supersonic configurations. Due to its dominance, our focus was on the fan tones propagating out the inlet. When applied to the noise of a two-stage fan and supersonic inlet, internal checks were used to confirm that known physics were being respected and initial assumptions regarding the use of symmetries were valid. Several long-held assumptions about this configuration, such as the importance of rotor-stator interaction in the aft stages on forward fan noise, were evaluated quantitatively for the first time. The impact of inlet details, such as the auxiliary door openings and its actuators, the centerbody and its struts, the impact of angle of attack, were quantified for future engineers. The noise database as a function of geometric and flow parameters provided corrections to the empirical noise modeling effort, as well as adding new input variables to the models to describe the complexities added by the supersonic-specific design features.

When large-eddy simulations were applied to the internally mixed exhaust configurations, the results were less successful. A key aspect of the noise produced by internally mixed nozzles was missing in the simulated noise. This deficiency in the simulation methodology was definitively confirmed by comparisons with data acquired in a test of a supersonic nozzle just prior to the start of the TC and by corroborating work by colleagues outside NASA. Although great insight has been gained during the TC, the simulations are not yet deemed reliable enough to use in place of physical experiments for improving jet noise models. For the purposes of fulfilling the TC requirements, the insights gained from the large-eddy simulations were supplemented by noise data from historical and small contemporary tests. The combination allowed the creation of improved and extended noise models that significantly improved the prediction accuracy for noise of supersonic-specific exhaust systems.

When the improved noise prediction models were tested against the small data sets from supersonic-relevant configurations, their accuracy was greatly increased relative to the original models. Statistically, the new models were better on average and were able to predict the acoustic impact of supersonic-specific features, making them more reliable in studies where such features might be varied. The statistically quantified uncertainties for the noise components were run through a model of the entire aircraft, where the weighting of the components on the total aircraft noise was accounted for using a Monte Carlo methodology. The reduction in uncertainty was dramatically improved, reducing the uncertainty from the baseline 7.8 EPNdB at the beginning of the TC to 2.0 EPNdB at the end.

The 5.8 EPNdB reduction in the key performance metric more than meets the stated TC goal of 5 EPNdB reduction, making the Prediction Uncertainty Reduction TC a success. More importantly, new prediction models, with documented uncertainty, are being published that will improve the accuracy of system studies used in decisions that will shape the future of civilian supersonic aviation. This report concludes with a list of observed gaps in high-fidelity prediction tools and ideas for noise reduction that arose from the PUR TC.

Contents

Executive Summary iii
1.0 Introduction 1
1.1 Problem Addressed by the Prediction Uncertainty Reduction Technical Challenge 1
1.2 Technical Challenge Objectives 2
1.3 Technical Challenge Approach 2
2.0 Technical Background 3
2.1 Prior Propulsion Studies 3
2.1.1 Fan Design Background 4
2.1.2 Exhaust System Design Background 5
2.2 Assessment of STCA Aircraft Noise Using 2018 Noise Models 6
3.0 Design of Supersonic Propulsion Components for Noise Database 12
3.1 Inlet and Fan Designs 12
3.1.1 Supersonic-Specific Aspects of Fan Design 14
3.2 Exhaust System Designs 15
3.2.1 Exhaust System Design Process 16
3.2.2 Development of Thrust Validation Capability 18
3.2.3 Final Designs 20
3.2.4 Lessons Learned in Exhaust System Design 21
3.3 Airframe Design 22
4.0 Fan Noise Model Development—Simulation and Modeling 22
4.1 Simulation Tool Description 22
4.1.1 FUN3D 23
4.1.2 Fidelity Fine Turbo 23
4.1.3 Actran 24
4.2 Validation Exercises for Fan Noise Toolchain 26
4.2.1 Summary of SDT Validation and External Review 26
4.2.2 Liner Property Investigation Using COMSOL 27
4.3 Simulations of SuperFan and Variants 30
4.3.1 Assessment of Inlet Distortion from Auxiliary Inlets on Tone Sources 30
4.3.2 Assessment of IGV-Rotor Spacing on Tone Sources 34
4.3.3 Propagation of Tones from Downstream Stages to Inlet 35
4.3.4 Assessment of Acoustic Liner Placement 35
4.3.5 Assessment of Axisymmetric Propagation from Source to Far Field 36
4.3.6 Assessment of Azimuthal Features on Propagation of Tones to Far Field 37
4.4 Extensions to Heidmann Fan Model 39
5.0 Jet Noise Model Development—Simulation and Modeling 44
5.1 Simulation Tool Description 44
5.2 Validation Exercises for Jet Noise Tools 45
5.3 Validation on Single-Flow Nozzles 48
5.4 Validation on Internal Mixers—Gaps in Simulation of Plug20 52
5.5 Historical Data Sets Used—Excess Noise Source Physics for Modeling 54
5.6 Validation of Rig Data Against Flight Data 56
5.7 Improvements to Jet Noise Models 60
5.7.1 Improved Noise Prediction Method for Single-Stream Jets 60

5.7.2 Improved Noise Prediction Method for Internally Mixed Exhaust Systems 60
6.0 Airframe Noise Modeling 61
6.1.1 Previous Studies 61
6.1.2 Generic Low-Boom Concept (GLBC) 62
6.1.3 Model Description 62
6.1.4 Computational Data 63
6.1.5 Synthetic Phased Microphone Array 63
6.1.6 Synthetic Array Data Processing and Integration Regions 64
6.1.7 Effects of End Caps and Spatial Resolution 65
6.1.8 Source Localization (Beamform) Maps 66
6.1.9 Overhead Versus Sideline Far-Field Noise Levels 68
6.1.10 Angle-of-Attack (AoA) Effects 69
6.1.11 Velocity Scaling for Far-Field Noise Levels 69
6.1.12 Comparison With Semiempirical Models 70
7.0 Uncertainty Assessments 72
7.1 STCA-Based Total Aircraft Noise Uncertainty 72
7.2 Fan Noise Component Uncertainty Assessment 73
7.3 Jet Noise Component Uncertainty Assessment 75
7.4 Evolution of Total Aircraft Uncertainty 77
8.0 Knowledge Gaps Identified 79
8.1 Aft Fan Noise Simulations 79
8.2 Broadband Fan Noise Modeling 79
8.3 Empirical Fan Noise Shielding Models 80
8.4 Acoustic Liners in Hot, High-Speed Flows 80
8.5 Improve LES of Internal Noise Sources 80
8.6 Improve LES for Shock Noise 80
8.7 More Efficient LES Methods 81
8.8 Expand Cycle Range (BPR) of Jet Noise Models 81
8.9 Explore Porous Plug, Nozzle Concepts 81
8.10 Airframe Noise From Supersonic Configurations 82
8.11 Low-Noise Operations 82
9.0 Summary of Results 82
Appendix A.—Acronyms and Abbreviations 85
References 87

Prediction Uncertainty Reduction Technical Challenge: Final Report

James Bridges and David B. Stephens
National Aeronautics and Space Administration
Glenn Research Center
Cleveland, Ohio 44135

Gerrit-Daniel Stich
Analytical Mechanics Associates, Inc.
Mountain View, California 94035

Gregory R. Busch
National Aeronautics and Space Administration
Glenn Research Center
Cleveland, Ohio 44135

Mehdi R. Khorrami
National Aeronautics and Space Administration
Langley Research Center
Hampton, Virginia 23681

Brenda S. Henderson, Edmane Envia, Alexander A. Svetgoff, William V. Banks, and Khairul Zaman
National Aeronautics and Space Administration
Glenn Research Center
Cleveland, Ohio 44135

1.0 Introduction

1.1 Problem Addressed by the Prediction Uncertainty Reduction Technical Challenge

In 2014, several companies were developing supersonic aircraft for commercial transport. While being a risky venture by itself, the industry faced a regulatory hurdle, even if they did not plan to operate supersonically over land—no airport noise certification rule was in place to tell them how quiet they had to be in landing and takeoff (LTO). The Federal Aviation Administration (FAA) and International Civil Aviation Organization (ICAO) regulations specifically omitted supersonic aircraft other than the Concorde. Without such requirements in the certification regulations, there was considerable risk that an aircraft designed would not be allowed to fly once a regulation was put into place at a lower noise level than the aircraft could achieve. Given that engineering considerations for LTO noise are generally diametrically opposed to those for range or payload, it is important to know the noise tollgate as the designer strives to maximize profitability of the aircraft.

On the other side, regulators were stymied in their process for creating the necessary noise regulations for supersonic aircraft. Historically, noise regulations are established using international consensus based on technical data from existing aircraft. Without existing commercial supersonic aircraft to establish the achievable trade between economic benefit and environment impact, regulators did not have the data needed to reach a consensus and establish noise rules. Feeling pressure from constituents, and acting under congressional mandate, on 30 March 2020, the FAA filed a Notice of Proposed Rule Making for small commercial supersonic aircraft. This Notice was based heavily on low-fidelity studies of business-class supersonic aircraft, primarily from NASA but approved by industry advisors. Further progress in rule-making will require international collaboration, which will require more information with strong credibility.

A key study vehicle being used in international deliberations, the Supersonic Technology Concept Aeroplane (STCA), used empirical noise prediction methods from NASA's Aircraft Noise Prediction Program (ANOPP), itself a product of decades of research into noise of conventional aircraft. NASA had shown that, when applied to conventional aircraft, such as the Boeing 737-800, the system prediction tools used in the STCA study matched well with published certification noise levels. However, technical experts were unsettled by some of the assumptions and extrapolations being used to apply the tools to the STCA, which had several supersonic-specific features. Furthermore, there was no way to establish the uncertainty of the projected noise levels. Again, lacking the traditional noise databases typically used to establish accuracy of the empirical noise models, there was concern about the accuracy of the noise estimates being used to establish noise policies in what could be a very expensive mistake.

This state of affairs was the motivation for the Prediction Uncertainty Reduction Technical Challenge (PUR TC) as formulated in 2019 to 2020 and officially established by the Advanced Air Vehicles Program in January 2021.

1.2 Technical Challenge Objectives

- Assess accuracy of models being used to predict LTO noise in international studies of commercial supersonic aircraft.
- Extend noise models to cover features and flow regimes relevant to supersonic aircraft and provide uncertainty metric for these models.

1.3 Technical Challenge Approach

Procure/create realistic near-term propulsion and airframe designs with high fidelity: geometric and flow specifications. From industry partners and internal expertise, establish the design space for which LTO noise models are needed. High-fidelity flow lines will be required.

Establish baseline uncertainty of noise models. Identify database of existing noise data relevant to supersonic designs for evaluation of noise models. This database will be very sparce due to a dearth of previous testing for these configurations. Most noise data will be from rig tests of propulsion components (fan, jet). Applying the existing noise models to these configurations as a practicing engineer would makes it possible to quantify the error of the predictions. Expressed statistically on a component basis, the impact of errors in separate noise sources will be combined as to compute the uncertainty of noise prediction for the total aircraft.

Validate physics-based simulation methods for far-field noise. State-of-the-art simulation methods will be applied to the realistic propulsion and airframe designs and their errors quantified. The first step is to establish best-practices numerical toolchains to simulate propulsion and airframe noise sources. The second step is to establish the accuracy of these simulation toolchains using nonsupersonic configurations for which there is quality noise data. Because even supersonic aircraft will need to be quiet in LTO operation, the flows will be similar to conventional aircraft, even if the geometric configurations are not. Thus, flow physics of the simulation methods should be the same for supersonic and conventional aircraft and the accuracy of the supersonic-relevant simulations can be quantified.

Create noise database for supersonic-specific components using validated physics-based simulations. The numerical toolchains validated in the previous step will be deployed on the realistic designs to create databases of far-field noise. Parametric variation in the designs will be explored to determine what aspects of the supersonic designs are critical in creating new empirical noise models.

Improve/extend empirical noise models using new noise databases. New empirical noise models will be created that reflect the findings of the physics-based simulations. These models will be compatible with existing system-level prediction methods but extend their validity to near-term supersonic aircraft.

Track improvements to empirical noise models. As new empirical models are created, their efficacy will be evaluated against the limited database of supersonic-specific experimental noise data used in the initial baseline assessment of prediction uncertainty. The reduction in the error of the prediction methods for noise sources should result in a reduction in prediction uncertainty for the total aircraft. This metric will be used as a Progress Indicator for the TC.

A shorter version of this Technical Memorandum was presented at the 2025 AIAA SciTech Forum (Ref. 1).

2.0 Technical Background

2.1 Prior Propulsion Studies

The PUR effort was largely influenced by system studies conducted by the NASA Commercial Supersonics Technology (CST) Project and its predecessors in 2010 to 2016 (Refs. 2 to 6). The N+2 and N+3 studies headed by Lockheed Martin and Boeing in partnership with General Electric (GE) Aviation, GE Global Research, and Rolls-Royce LibertyWorks brought out many of the features that would be required of civil supersonic aircraft. Critically, these studies produced engine cycles and component concepts that were needed for higher fidelity analysis such as was undertaken in the PUR TC. Studies of inlet design and exhaust system requirements and how they integrated with the core turbomachinery formed much of the basis for designs used in the PUR TC.

Prior work on inlets includes studies at the NASA Glenn Research Center (Ref. 7) of the Low-Boom Flight Demonstrator. The study considered an axisymmetric spike, like the present report, although a simpler pitot inlet was chosen for use on the X-59 aircraft (Ref. 8).The axisymmetric spike inlet is efficient at cruise but has insufficient open area to allow safe engine operation at low speeds during takeoff and landing. The study concluded that the appropriate flight speed for transitioning between open and closed auxiliary inlet configurations was Mach 0.6. This flight speed is well above the 250-knot noise certification speed limit specified in FAR 36 (Ref. 9), so the relevant configuration for acoustic analysis is with the auxiliary inlet open.

The CST Project sponsored a study by GE Aviation, Lockheed Martin, and Stanford University (Ref. 5) that developed a concept vehicle called the LM1044, a Mach 1.7, 80-passenger trijet. This concept vehicle also utilized an axisymmetric spike inlet with a translating cowl auxiliary inlet. The design of this engine inlet included details such as struts and cowl support actuators, similar to the present geometry. As described in Section 7.2 of Reference 5, a linearized Navier-Stokes code was used for computational aeroacoustics (CAA) to study noise propagation through the inlet, auxiliary doors and consider the presence of struts. A few observations were made, such as the auxiliary opening being a significant noise leakage path. The study also concluded that the auxiliary inlet will be open at all noise certification points.

The F120 fan model (Ref. 10) was developed during the NASA High Speed Research (HSR) program and is based on test data from a single engine with a three-stage fan tested on a stand with a bellmouth inlet. As part of the HSR program, research was conducted into the effect of inlet geometry on the fan noise. This included several studies at Virginia Tech (Refs. 11 and 12) and an investigation at the Boeing Low-Speed Aero-acoustic Facility (LSAF) (Ref. 10), which was used to develop a correction for a two-dimensional (2D) bifurcated inlet. Four corrections are available, for the three aircraft noise rating conditions of sideline, approach, and flyover, also called centerline. The centerline correction is provided both with the auxiliary

inlet doors open and closed. The disposition of the doors for the other two cases is not clear. Because these corrections were developed with a fan model, they include the effect of the inlet geometry combined with the resulting flow distortion on the fan source.

In summary, studies on the acoustics of a representative supersonic passenger jet suggested that fan noise at approach condition is likely to be a major contributor to the overall certification noise level of a commercial supersonic aircraft and auxiliary inlet doors will be required.

2.1.1 Fan Design Background

The requirement of variable inlet area and multistage fans raised the question of how well current fan noise models would be able to predict the unconventional configurations. Even inlets that were essentially uninstalled and axisymmetric had features such as a centerbody and support structure that could be expected to produce distortions into the fan. Experience and theory indicate that distortions hitting the fan face produce significant levels of noise. More complicated nonaxisymmetric inlets would introduce even more irregularities and are thought to be worse. Having multiple stages of rotor-stators was another area raising acoustic uncertainty. NASA studies in 2016 showed that even near-term commercial supersonic aircraft would likely need two stages of propulsor to meet their range and performance goals. Senior technologists at engine companies working on supersonic propulsion were asking NASA for insight into how to predict the noise of multistage fans. Historically, acousticians assumed that noise sources associated with rotor-stator interaction downstream of the first stator did not propagate through the first blade row and therefore could be ignored in the inlet noise component. But this assumption had never been tested, and the additional noise sources were not in any fan noise prediction method.

To gain insight into how fan tones propagated out of supersonic inlets, a small-scale model of the inlet used in the Lockheed N+2 study was fabricated and mated with a duct instrumented with piezoelectric acoustic drivers to produce known duct acoustic modes. The model was operated in an anechoic chamber with an array of microphones to sample to the far field. Measurements found that the directivity difference between a conventional inlet and the supersonic inlet was minimal. Estimates of the impact on EPNL found the difference to be less than 1 EPNdB. However, this study was done without flow. Further details can be found in Reference 13.

The problem of multistage rotor-stator sources and their propagation was more difficult to address. At the end of the NASA HSR Program of the 1990s, a two-stage fan, the Quiet Supersonic Platform (QSP) was designed by the Program's partners, primarily Pratt & Whitney and GE Aircraft Engines. Some additional details on the aero design of the fan system are given in Reference 14. An abbreviated test of the fan system, without a supersonic inlet, was conducted in 2002 under Defense Advanced Research Projects Agency (DARPA) funding and GE oversight. The purpose of the test was to obtain a baseline acoustic signature for HSR-era fans. The fan model was tested with two sets of inlet guide vanes (IGVs), variable spacing between IGV and the first fan (R1), along with variable R1 and stator spacing. The IGVs were variable pitch and operated on a schedule with fan speed such that the IGVs unloaded the fan at low speeds. The first stator set pitch angle was also variable. A 2D bifurcated inlet was designed and manufactured, but testing was only conducted using a subsonic inlet, as shown in Figure 1. The 0.48-m (19-in.) rig test was operated up to 91.2 percent speed or 16,270 rpm. A number of hardware configurations were tested in the NASA Glenn 9- by 15-Foot Low-Speed Wind Tunnel (9×15 LSWT), including IGV-R1 spacing and an inter-stage acoustic liner. The acoustic far-field data from this test was held by NASA , although the design, including fan shape geometry, of the test articles does not belong to NASA. This acoustic data is unique for multistage fans, but with the age of the design and the lack of detailed geometry, it is not very useful to inform current practice or to validate high-fidelity simulation tools. It is, however, useful in the PUR TC as the data set to assess the uncertainty of the fan noise empirical tools for supersonic aircraft.



Figure 1.—Quiet Supersonic Platform (QSP) fan model in the 9×15 LSWT in 2002.

In 2019, GE Aviation was developing the Affinity engine to power Aerion's supersonic business jet. NASA negotiated to partner on fan noise tests in the NASA Glenn 9×15 LSWT. This would have provided the needed acoustic data, with detailed geometry, for a modern multistage fan behind a supersonic inlet. However, funding did not materialize from both parties for the tens of millions of dollars required to fund the test. In fact, the engine development effort collapsed in 2020, leaving GE with a NASA contract to deliver an early version of their fan design, which they did in November 2020. This design, dubbed the SuperFan, is the subject of the high-fidelity simulations used in the PUR TC to answer the questions originally raised in the onset of the development effort, and is the basis for the improved empirical fan noise models that resulted from the TC. Indeed, it is hard to overstate the importance of low-level technical interactions between NASA and GE during the development of the Affinity in increasing the relevance and realism of NASA's work in the PUR TC.

2.1.2 Exhaust System Design Background

On the exhaust end of the engine, the aforementioned N+2 studies had clearly delineated the importance of using an internally mixed exhaust system to reduce boattail drag. The desire to minimize sonic boom in flight also encourages minimizing shocks from changes in nacelle outer flow lines. This in turn encouraged the inclusion of an external plug architecture to minimize nacelle boattail and improve cruise thrust. In the Rolls-Royce and GE portions of the N+2 Validation contracts, including tests conducted at NASA's Aero-Acoustic Propulsion Lab (AAPL), three-stream engine cycles had been explored. Rolls-Royce had proposed and built scale models of a clamshell mixer-ejector nozzle system. This configuration was plagued by flow unsteadiness that manifested in a howl and was not considered a success. GE Aviation proposed and tested an exhaust system that split the primary fan stream, mixing roughly half with the core stream while feeding the other half of the flow to the inner annulus around an external plug. The secondary, variable fan stream was fed to a partial outer annulus as a shielding flow for high mass flow LTO operations. Although the complicated configuration did result in a slight noise reduction relative to a fully mixed nozzle, the complexity of creating the inverted velocity profile, along with the multiple sliding cowling components required to adjust station 9 areas, made the nozzle difficult to consider for near-term commercial application.

Historically, internally mixed exhaust systems have used forced mixers to mix the core and bypass streams as fully as possible. Experience and intuition indicated that a fully mixed jet exit flow condition would yield the lowest jet noise. However, it was noted that a fully mixed condition was not easily achieved without generating internal noise from the mixer. NASA had hosted many industry tests in the

1995 to 2006 timeframe where multiple mixer designs, intended for subsonic aircraft, had been tested for noise. Although NASA retained the data and the right to use it, there had not been much effort to analyze the data as the industry partners developed proprietary noise models and published those portions of their efforts as they deemed fit. The main lesson learned from this experience working with industry was that predicting and reducing the internal noise of the mixer was very difficult. However, the data and gross geometric properties were used in the PUR TC in lieu of missing high-fidelity simulations.

The historical database of internally mixed nozzles, all having an internal plug, was supplemented by a critical test program run in 2020, the Plug20 test. The Plug20 test was conceived as having interchangeable mixers, internal/external plug, and a variation in mixing length, all with common flow areas and engine conditions. A very abbreviated test was carried out in the days before the Covid-19 pandemic closed onsite testing at NASA in March 2020, and this test data was critical in several aspects. First, it confirmed the behavior of internal noise found in the previous subsonic tests. Second, it extended the range of applicability to much higher engine pressure and temperature conditions more representative of supersonic aircraft. Third, it showed the acoustic impact of having an external plug instead of an internal one. Fourth, having full geometry descriptions of the test hardware, the test provided an important validation of the high-fidelity simulation tools used in the PUR TC. And finally, the Plug20 database, along with a database of fully mixed jets, was used in assessing the uncertainty in the jet noise models for supersonic applications.

2.2 Assessment of STCA Aircraft Noise Using 2018 Noise Models

The baseline LTO noise assessment for the PUR TC was selected to be that of the NASA-developed 55-tonne Supersonic Technology Concept Aeroplane (STCA). The STCA is a notional research aircraft created to perform investigative studies and provide information to the International Civil Aviation Organization's (ICAO) Committee on Aviation Environmental Protection (CAEP) to assist in future regulation efforts for supersonic aircraft. The 55-t (121-klb) STCA is an eight-passenger trijet aircraft that is intended to be representative of early-entry supersonic business jets currently in development by industry. The aircraft was designed for Mach 1.4 supersonic cruise with a range of 4,243 nmi. The 55-t STCA is not intended to be a low-boom aircraft and only operates at supersonic conditions over water. A summary of the aircraft characteristics is shown in Table 1. A model of the STCA aircraft is shown in Figure 2. Technical details of the STCA aircraft are available in Reference 15.

TABLE 1.—55T STCA TRIJET CHARACTERISTICS

Max. takeoff weight, klb	121
Passengers	8
Cruise Mach	1.4
Engines (×3)	CFM56-derived
Overall length, ft	135
Span, ft	67
Wing reference area, ft^2	1,619
Wing aspect ratio	2.7
Wing taper ratio	0.09
Wing loading, lb/ft^2	74
Wing fuel, klb	24
Fuselage fuel, klb	36
Fuel fraction	0.50

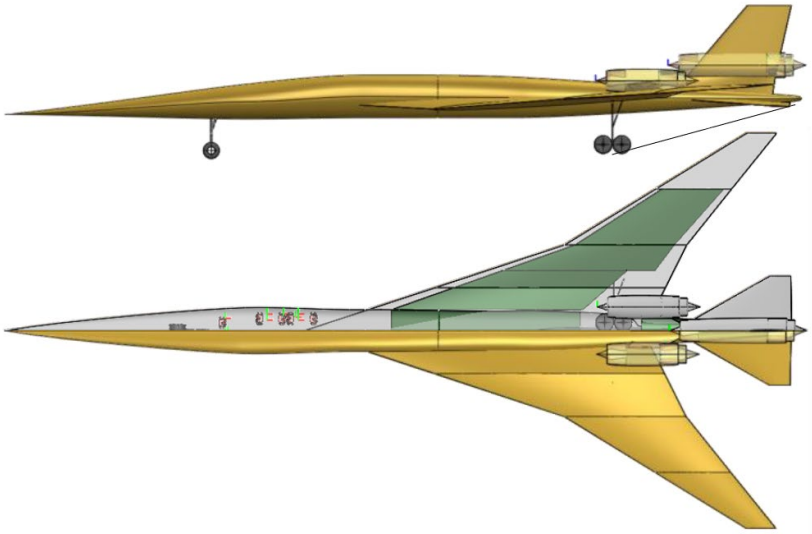


Figure 2.—Model of 55-t STCA trijet concept aircraft.

TABLE 2.—ENGINE PERFORMANCE SUMMARY FOR 55-T STCA TRIJET ENGINE

	M 1.4, 50 kft, ISA	M 0.25, sea level, ISA+27 °F	Sea level static, ISA+27 °F
Net thrust, lb/engine	3330	14,140	16,620
Specific fuel consumption, lb/h/lb	0.943	0.588	0.479
Bypass ratio	2.9	2.9	3.0
Burner temperature, °R	3,300	3,150	3,130
Turbine inlet temperature, °R	3,180	3,040	3,020
Compressor exit temperature, °R	1,450	1,440	1,430
Overall pressure ratio	22	21	21
Fan pressure ratio	2.0	1.9	1.9
Compressor pressure ratio	11.2	11.1	11.2
Extraction ratio	1.1	1.1	1.1
Nozzle pressure ratio	5.9	1.9	1.8

The reference STCA aircraft has three overwing-mounted, CFM56-7B-derived engines that were analytically redesigned using the Numerical Propulsion System Simulation (NPSS) software (Refs. 16 and 17). The redesign of the engine for supersonic applications includes a higher pressure ratio single-stage fan on the low-pressure spool that operates at peak efficiency at a pressure ratio of 2.2. The engine redesign also features an internally mixed flow with a single-stream convergent-divergent plug nozzle. The center body plug and nozzle throat are fixed while the divergent flaps are variable. Table 2 summarizes the engine performance characteristics at relevant conditions for both cruise performance and LTO acoustic performance. Figure 3 depicts models of the CFM56-7B engine and the notional modified supersonic variant for the STCA.

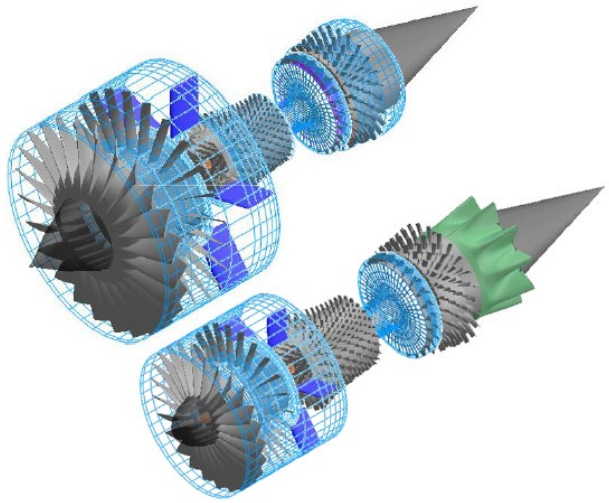


Figure 3.—Engine models of CFM56-7B (top) and notional modified supersonic variant (bottom).

NASA used several conceptual design tools to synthesize and assess the notional STCA model. A solid modeling tool (Ref. 18) is used to define the outer mold lines of the airplane, to guide interior packaging, and to estimate internal fuel volume. The model also informs component weight and vehicle aerodynamic analyses. Lift-dependent drags, lift-independent drags, and wave drags are calculated by the methods described in References 19 and 20. A weight estimate of the STCA wing is made using physics-based factors based on its gross geometry, while weight estimates of other major structures and systems are made using statistical-empirical relations. The airframe weight estimation methods are discussed in Reference 21. The mission performance assessment of the STCA was done using NASA's Flight Optimization System (FLOPS) (Ref. 22). All LTO noise predictions for the STCA are made using NASA's Aircraft Noise Prediction Program (ANOPP) (Refs. 9 and 10). An in-depth description of the development of the 55-t STCA model can be found in Reference 11.

For the PUR TC, the reference 55-t STCA was modified to move the overwing-mounted engines to underneath the wing, a configuration more commonly proposed. This modification was also made to remove the uncertainty associated with noise-shielding effects and to isolate the source-noise uncertainty for fan inlet radiated noise as much as possible. A depiction of this variant is shown in Figure 4. For the baseline noise assessments of the STCA, the existing internal source-noise modules of ANOPP were used without modification, aside from the fan noise source and the airframe noise source. The fan source-noise predictions include acoustic treatment suppression based on empirical methods in Reference 23 for both the inlet-radiated and discharge-radiated fan noise. The airframe noise predictions are initially calculated using ANOPP's Fink airframe noise prediction method (Ref. 24) and then adjusted based on acoustic testing of the high-speed civil transport airframe (HSCT) in 1996 (Ref. 25). Currently, there is discussion amongst regulation authorities to permit future supersonic aircraft to utilize Variable Noise Reduction Systems (VNRS) during takeoff and landing operations to reduce the amount of airport noise generated by these aircraft. VNRS are automatic changes allowed during the operation of the aircraft to abate noise without the intervention of the flight crew. Examples of VNRS include programmed thrust lapse and programmed high-lift devices. However, to focus the uncertainty assessments on source-noise predictions, all evaluations of the STCA LTO noise for this effort are conducted without any VNRS deployed. All the LTO noise predictions are made using a standard takeoff/landing trajectory for noise certification, in



Figure 4.—Underwing engine STCA variant used for PUR TC.

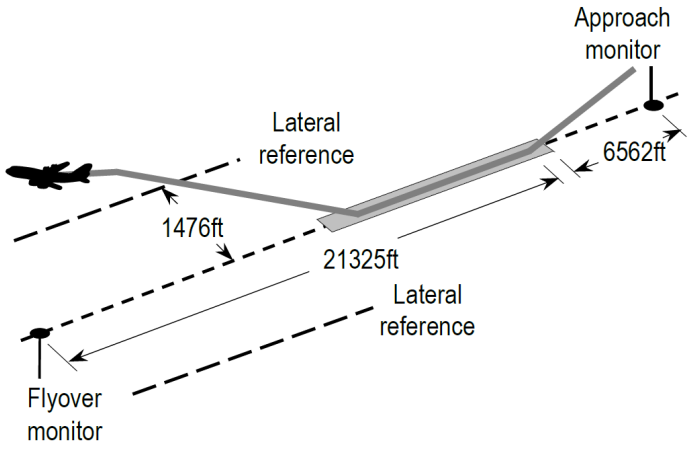


Figure 5.—Noise certification monitor arrangement relative to takeoff and landing flight paths.

accordance with the requirements for subsonic transports in 3.6.2 of Reference 26. Atmospheric absorption, ground reflections and lateral attenuation effects are included in the LTO noise assessments according to methods described in Reference 27.

The aircraft system-level uncertainty assessments for the TC are conducted relative to the LTO noise certification metric regulated by ICAO, Effective Perceived Noise Level (EPNL). The cumulative EPNL is used as an aggregate metric of separate EPNL calculations occurring at three noise monitor locations: Lateral, Flyover, and Approach as defined in Figure 5. Instantaneous Sound Pressure Levels (SPLs) are determined throughout the operational trajectory and converted to Perceived Noise Levels (PNLs) using a noy table to account for human annoyance. The PNLs are then corrected for tonal content and differences to Tone-Corrected Perceived Noise Levels (PNLTs). The maximum PNLT is determined and the PNLTs within a 10-dB difference of that maximum (commonly called the 10-dB down period) are then used for the EPNL calculation, accounting for the duration of the 10-dB down period (Ref. 26).

The benchmark LTO noise assessment of the baseline STCA model resulted in a cumulative EPNL of 280.1 EPNdB. A breakdown of the individual noise sources and their contributing noise levels is shown in Figure 6. These results show that the jet noise component is very dominant relative to other noise sources at the lateral and flyover noise monitors, which is expected for a supersonic aircraft with low bypass ratio engines and high nozzle exit velocities. At the approach noise monitor, the dominant noise sources are the jet noise, fan inlet noise, and fan exit noise. In fact, the fan inlet tonal noise is equivalent in EPNL contribution to the jet noise for approach. As a result of this analysis, the TC investigators focused the uncertainty reduction efforts on the jet noise source and fan inlet radiated noise source. It was decided not to include the aft fan noise sources, core noise source, and airframe noise sources in the initial uncertainty reduction efforts due to their lessor contributions to the airport LTO EPNLs. Additionally, there are currently fewer data sets and studies available to use in uncertainty reduction efforts for these

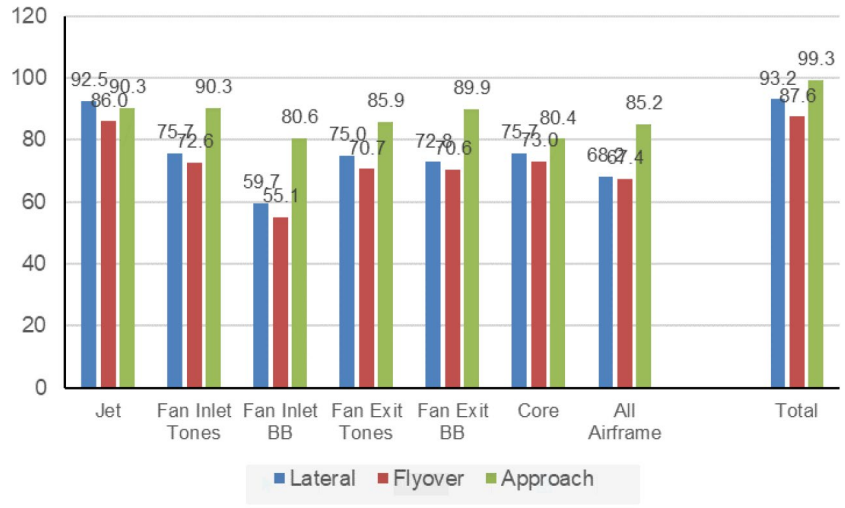


Figure 6.—Benchmark prediction of STCA, underwing engine variant.

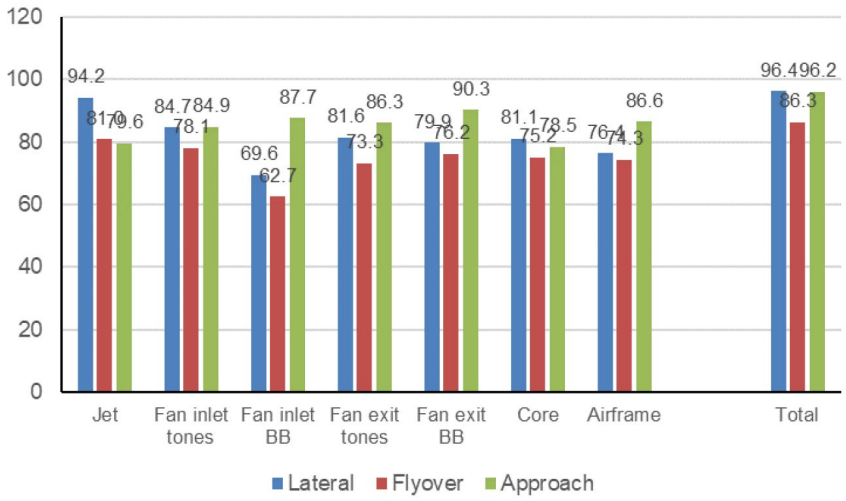


Figure 7.—Benchmark prediction of 737-800/CFM56-7B.

ancillary noise sources, but they should be considered for future studies to improve the overall LTO EPNL uncertainty for supersonic aircraft. It should also be noted that the relative importance of each noise-source component is based on the configuration, size, and capabilities of the STCA vehicle and could be slightly different for other supersonic aircraft concepts. To have a comparison point to the STCA model, a benchmark LTO noise assessment was performed using a 737-800/CFM56-7B aircraft model. The 737-800 assessment resulted in a cumulative EPNL of 278.9 EPNdB and a breakdown of the individual noise sources is shown in Figure 7.

It can be observed in a comparison of the two aircraft that the core noise and airframe noise of the 737-800 were predicted to be louder than that of the STCA. The difference in the core noise, even though both models are using a CFM-56B core model, is a result of the engine power setting differences at sideline/flyover conditions between the two models. The STCA is overpowered at takeoff and therefore is using a de-rate of 10 percent at takeoff and Programmed Lapse Rate (PLR) during the flyover phase of the trajectory, whereas the 737-800 is operating at maximum thrust for takeoff, resulting in higher core

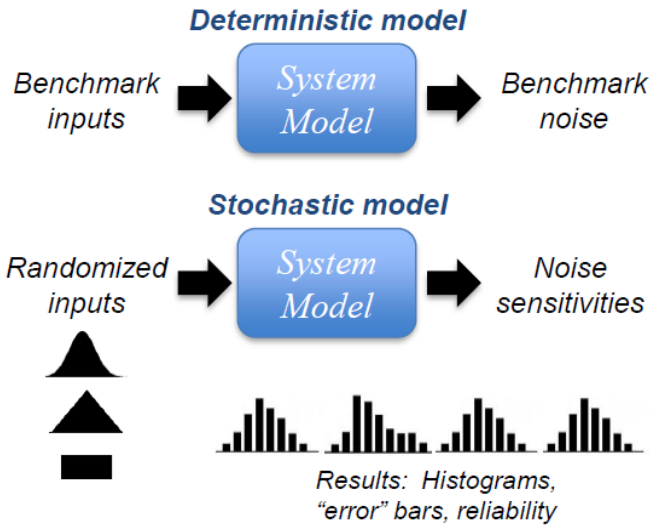


Figure 8.—Deterministic versus stochastic modeling.

noise levels. The airframe noise is lower for the STCA than the 737-800 due to delta-wings having less trailing edge span to generate noise and a simpler flap/slat system than the 737-800 model.

After the benchmark EPNL numbers were generated for both the STCA model and the conventional 737-800 model, an uncertainty assessment for each vehicle was performed. Because the fan inlet noise and jet noise were determined to be the focus of the current TC, these noise sources were included as normal distributions in the system uncertainty assessments (SUA). The term "system" in this context is defined as the entire aircraft system to include both engine and airframe noise sources. The benchmark values for both aircraft models were determined through a deterministic model where the inputs to the system noise model are fixed values generating unique source-noise spectra for each noise component (see Figure 8). This deterministic approach generates a single fixed output noise value for each model, representing the cumulative EPNL. For the SUA, a stochastic modeling approach was used. This entails creating a randomized probability distribution function (PDF) for the three noise-source components subject to uncertainty: jet noise, fan inlet tone noise, and fan inlet broadband noise. The PDFs for these noise sources are described using a standard deviation and offset from the mean value to create a normal distribution. The noise sources not included in the current uncertainty efforts (aft-radiated fan noise, core noise, airframe noise, and gear noise) are modeled deterministically. Therefore, the resulting output of the stochastic model are EPNL noise sensitivities that capture the uncertainty only from the fan inlet-radiated noise and jet noise (see Figure 8).

The output of the SUA is described as a mean EPNL value with a corresponding standard deviation. The SUA of the 737-800 model resulted in a mean value of 276.1 EPNdB with a standard deviation of 1.5 EPNdB. The initial SUA of the STCA model resulted in a mean value of 279.7 EPNdB with a standard deviation of 7.8 EPNdB, which is 6.3 EPNdB greater than the standard deviation of the conventional subsonic aircraft. The primary goal of the TC is to work to reduce this standard deviation value for the STCA by 5 EPNdB to bring the uncertainty associated with modeling supersonic jet noise and fan inlet noise down to 2.8 EPNdB, closer to the subsonic uncertainty value of 1.5 EPNdB. Further details describing the initial SUAs for both models, including the input distributions used can be found in Reference 28. For reference, a cumulative error of 2.8 dB, if split evenly between the three measurement points, would correspond to an error of 25 percent in sound power. Given that most measurements of sound in the real world have an uncertainty of roughly 1 dB, a cumulative uncertainty of 2.8 EPNdB in prediction over three measurements would be hard to measure.

3.0 Design of Supersonic Propulsion Components for Noise Database

High-fidelity simulations for noise require high-fidelity designs. By high fidelity, we mean three-dimensional (3D) flow lines with details down to where they change noise sources. For fan noise, this means inlets with flow lines, liner impedances, and structural details such as struts and actuators. It means fan and stator blades with full 3D surfaces, preferably in the shapes they assume with loading. For jet noise, this means full flow lines from the turbine rear frame. Internal mixers and lip treatments should be defined near manufacturing tolerances, not as simple shapes.

Having access to this level of detail is a challenge. For starters, it requires that the mission and performance requirements be established down to the component level. Aircraft drag polars are needed to establish power requirements, angles of attack, airspeed, and altitudes. Engines must be designed to a level where component pressure and temperature rise are known, along with basic dimensions to give aero performance targets. It requires analysis and optimization of component flow lines for aero and acoustic performance.

Few organizations have this depth of expertise over the range of disciplines. NASA leveraged its industry connections to narrow the conceptual design space and, in the case of the fan, it procured the full propulsor design, the SuperFan, from inlet through stators. NASA's internal airframe design and NPSS expertise was used to create aircraft drag polars and one-dimensional engine flow designs that reproduced industry thinking about near-term designs. The exhaust system was designed by creating in-house expertise in mixer and plug aero design and then creating nozzle designs that mated with the SuperFan engine (a refanned version of the CFM56 core). Variations in the designs were guided by acoustic impact but were carefully created to keep aero performance. Significant effort was put into the designs that were simulated to make sure the acoustic database represented realistic designs that might come from an industry engineer's efforts. For airframe noise, it was not possible to get an airframe design with enough fidelity for credible high-fidelity simulation of noise, so a different approach was pursued. The uncertainty of existing empirical airframe noise models was assessed on an existing high-fidelity supersonic geometry, the X-59. Details of this assessment are given in Section 6.0.

3.1 Inlet and Fan Designs

In 2020, NASA contracted with GE Aviation (contract NNC15BA05B/80GRC019F0174) to deliver a fan and inlet design for a supersonic commercial passenger aircraft. NASA provided the SUPIN (Ref. 29) inlet design tool and provided guidance on its use. GE Aviation provided to NASA a design representing their engineering process up through preliminary design. To become a product, the design would need to be modified for aeroelastic and aeromechanical requirements, as well as possible manufacturing requirements. The design was evaluated for stall margin at the level required by the company at this stage of development. Its aero efficiency was evaluated as being on target for a product, which was confirmed by NASA's independent analysis. The design includes significant aeroacoustic design input, including specification of liner treatments. Within NASA, the design is known as the SuperFan, being a design appropriate for a commercial supersonic aircraft. A NASA rendering of the delivered inlet and fan design is given in Figure 9.

The SuperFan has an axisymmetric spike inlet designed for Mach 1.4 operation at 50,000-ft altitude. The axisymmetric and on-design geometry was modified to meet other requirements (see Figure 10). Mechanical features were added, such as struts to hold the spike in place. The center spike was tapered to zero thickness, such that the duct geometry transitions from annular to circular upstream of the engine. For low-speed operation, an axisymmetric auxiliary inlet was added by splitting the outer cowl and translating the upstream portion forward. Actuators were added to the geometry to support the translating

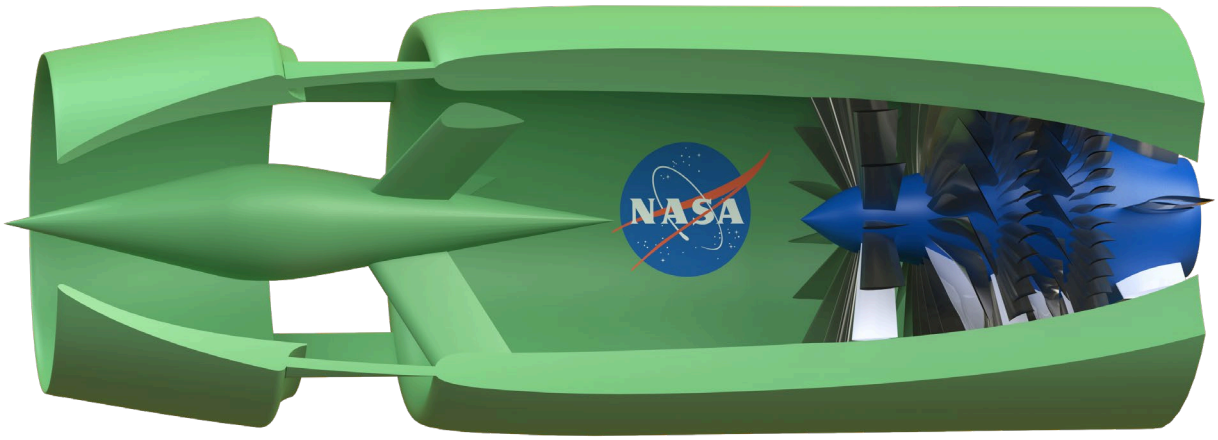


Figure 9.—Render of SuperFan inlet and two-stage fan.

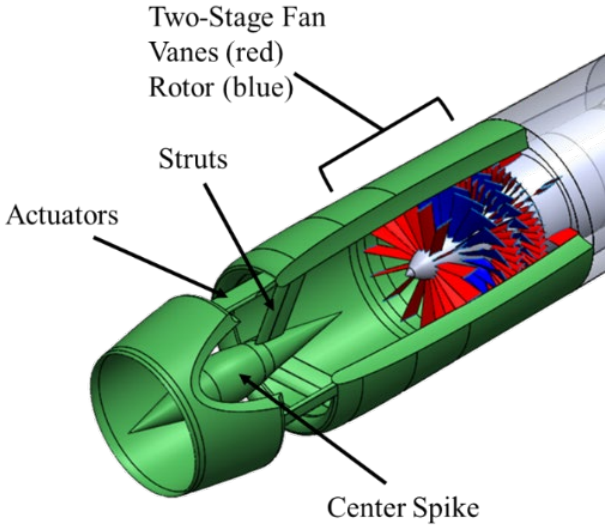


Figure 10.—Components of SuperFan inlet.

cowl. This fan-inlet combination is a preliminary design that includes the principal expected features of a supersonic engine and represents a good starting point for acoustic analysis.

Critically, the inlet and fan design is not proprietary; NASA owns the flow lines and analysis of the SuperFan. Because the design incorporates much of the expertise needed to design weapons-grade propulsors, the geometry is publicly available but only to parties with an export control license. This allows the design to be evaluated by qualified organizations and so serves as a validation test bed for fan noise simulation methods. Unfortunately, the design is not appropriate for model-scale production and testing, lacking aeromechanical analysis and design modifications for scaling.

3.1.1 Supersonic-Specific Aspects of Fan Design

The SuperFan is significantly different than typical subsonic examples in a number of ways. Figure 11 illustrates the significant differences between a conventional inlet and fan and that required for a supersonic aircraft. The inlet is long, has a centerbody, and includes an actuated auxiliary inlet and struts. In the figure, the inlet is shown with the leading portion of the cowl extended forward, creating an auxiliary inlet. This is required for low-speed flight because although the inlet is sized for the relatively low mass flow of supersonic cruise, the engine requires more air flow at LTO. To provide the extra airflow, an extra opening must be provided to supplement the airflow captured by the sharp-lipped supersonic inlet.

The propulsor or fan consists of an inlet guide vane (IGV), two rotors, and two stator stages. The difference between a conventional fan and the supersonic fan are the IGV, the second rotor-stator stage, and the small spacing between blade rows required to minimize engine length. All these features promise to change, and likely increase, the sources of noise from the rotating machinery.

The SuperFan was designed with both aerodynamic and acoustic considerations. Blade and vane counts were chosen to reduce fan tone noise caused by Tyler-Sofrin rotor/stator interaction. This is a typical approach for fan design, where a small change to blade counts can have a significant impact on noise. A fan inlet acoustic liner was also specified by GE, with complex impedance selected to reduce inlet tone noise. Advanced or specialized design features such as blade tip sculpting or acoustically treated vanes were not included.

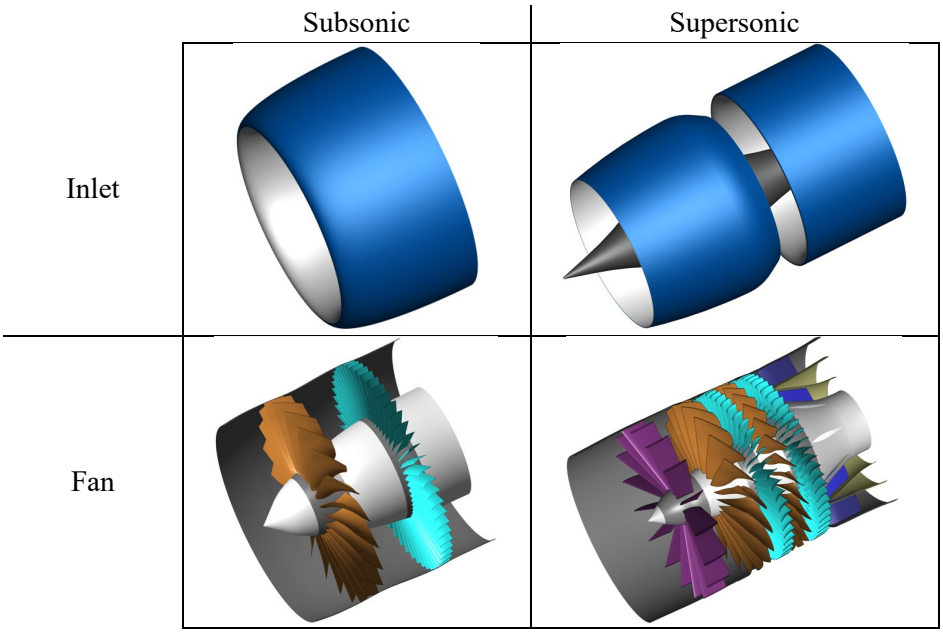


Figure 11.—Difference between subsonic and supersonic inlet and fan designs. Rotors are shown here in brown, stators are cyan, and IGV are purple.

3.2 Exhaust System Designs

Although off-the-shelf designs could be purchased from industry partners for a supersonic fan and inlet and the X-59 airframe, no such designs were available for suitable exhaust nozzles. To address this, an in-house nozzle design capability was needed. The output from the Numerical Propulsion System Simulation (NPSS) of the 55-t STCA analysis, provided by Berton (Ref. 15), was used as a starting point. This provided the team with duct areas, mass flow, pressures and temperatures. With the STCA flow conditions roughly matching the GE SuperFan design procured for the fan noise work, the SuperFan outer nacelle area at the fan section was adopted as a constraint for the exhaust system. An internally mixed configuration was chosen for the nozzle architecture.

The STCA engine did not require a variable nozzle throat but did require a variable final exit area. In military applications, flap-and-seal nozzles are often used to accomplish this variability. These designs require maintenance at a rate much higher than commercial use would find acceptable. In addition, a design decision was made to keep the nacelle outer diameter constant over the nacelle as much as possible, reducing boattail and shocks contributing to boom signature. This decision led to the adoption of an external plug architecture as the fully expanded engine flow would not fill the area of the nacelle. A notional sketch of the combined propulsion system is given in Figure 12. An external plug would make up the difference in area while having the boattail area change occur over the plug and expansion of the plume. This did have the effect of transferring the boattail losses from the nacelle to the nozzle in standard thrust bookkeeping practices. Thrust coefficient values for the nozzle with the flow separation on the plug were in the range of 0.95 to 0.96 as a result of this decision, making the design of the external plug important. Based on limited experimental data, the separations on the external plug were assumed to not produce excessive noise, although this assumption has not been extensively tested.

For the PUR studies, both a translating plug and translating cowl were considered as methods to vary A9, in lieu of a flap-and-seal design seen on military converging-diverging nozzles. A translating plug, similar to the aerospike inlet on the Lockheed SR-71 Blackbird, was initially favored, as it allowed the team to take advantage of legacy design work and knowledge. However, it became apparent that actuation hardware would need to be housed within the turbine rear frame or plug shaft, exposing it to high temperatures. A translating cowl has been the presumptive configuration, as actuation hardware will require far less cooling.

To design the exhaust system, Reynolds-Averaged Navier-Stokes (RANS) simulations were adopted as the most appropriate tool. Using RANS simulations, hundreds of potential designs were assessed for thrust performance once an analysis process had been established.

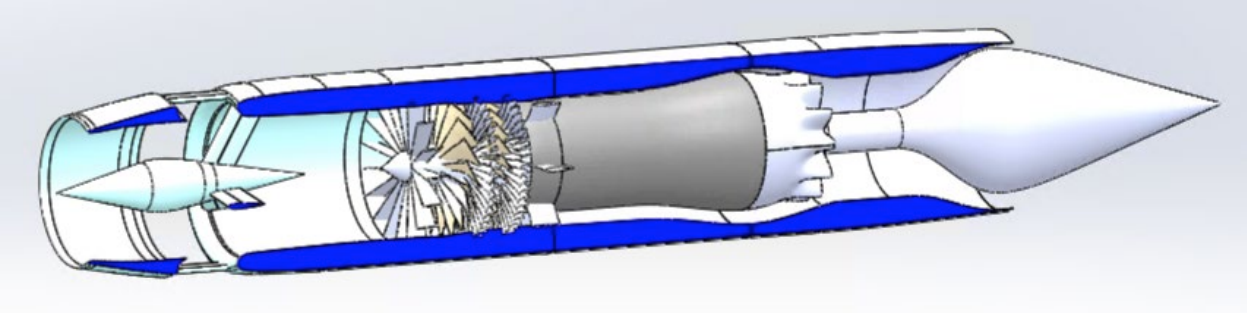


Figure 12.—Notional supersonic propulsion system for PUR studies.

3.2.1 Exhaust System Design Process

The design task was subdivided into two parts: one focusing on the aero performance of the internal mixer and duct, assuming a common simple external plug design, and another analyzing the external plug contour, assuming a fully mixed internal flow. Early checks on the assumption that the impact of an imperfectly mixed flow from a lobed mixer did not impact the plug design were favorable. For both mixer and plug design work, parametric studies were performed using RANS simulations, and reduced-order models were generated from the large database, with the ultimate goal of selecting a small pool of designs for experimental and large-eddy simulation (LES) efforts. The final designs chosen performed well aerodynamically while offering a diversity of design features and flow-field properties whose acoustic impact could be explored in large-eddy simulations and tests.

To begin, literature was reviewed of previous plug design efforts, given in Reference 30. Next, a variety of plug design techniques were examined, largely centering on some method of axisymmetric contouring. Plugs designed using the Method of Characteristics (MoC), typically employed for the contouring of the divergent section of converging-diverging rocket engine nozzles, were initially considered but rejected due to their incompatibility with the low-boattail angle design goal. Instead, a method of parameterizing the plug geometry was devised along with the automated grid generation strategies to allow studies of the design space using RANS simulations.

Ultimately, a conic section using three parameters was chosen as the axisymmetric contouring methodology. An optimization study was conducted using a Latin Hypercube design of experiments methodology to model the parameter space, with thrust and flow coefficients as performance metrics (Ref. 31). Optimized plug contours were found for both takeoff and cruise conditions (shown in Figure 13), as well as a compromise design optimized for both mission points simultaneously.

Similar to the plug effort, a literature review, presented in References 32 and 33, informed geometric parameter and performance metric selection for the mixer studies. An extensive workflow that incorporated automated surface mesh and grid generation for RANS simulation was developed.

To best generalize mixer analysis, area-change effects were removed by freezing duct areas from the inflow plane through the entrance to the converging duct segment. In the phase I study (Ref. 32), mixer surface contours were defined via two equations in cylindrical coordinate space, with influence from five parameters. These parameters described relatively simple lobed mixers having n-fold symmetry, planar exit, and no total area divergence but varied mixer length and lobe height and width. Four performance metrics were tracked relating to thrust, mixing effectiveness, and flow-field uniformity. Examples of the lobed mixer designs produced during the phase I study are shown in Figure 14. In the phase II study Ref. 33), scarfing and scalloping features (illustrated in Figure 15) were explored in a four-parameter space using the same four performance metrics.

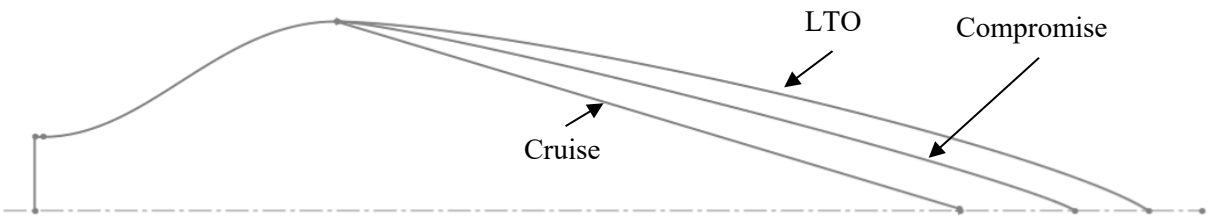


Figure 13.—Plug profiles optimized for STCA cruise, landing, and takeoff, and compromise shape.

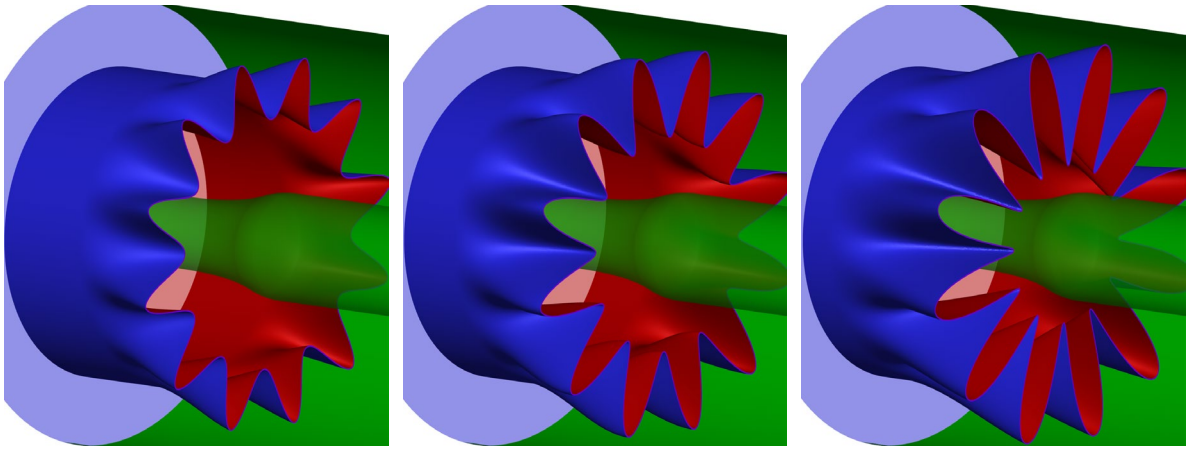


Figure 14.—Representative mixer designs from phase I study.

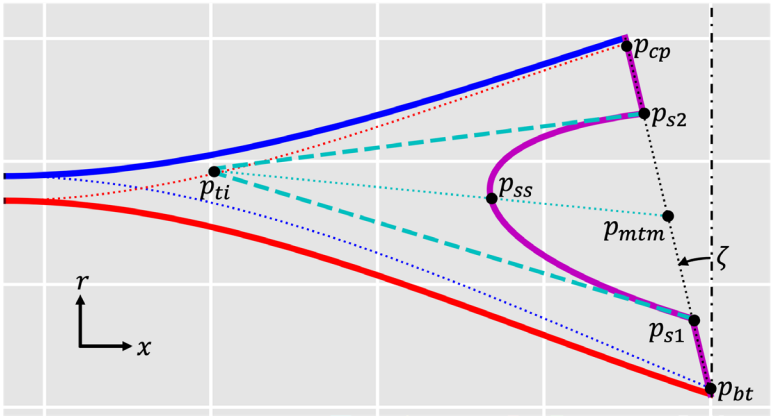


Figure 15.—Scalloping and scarfing parameters from phase II study.

Effects on these metrics were strong for the initial five-parameter set, with values of thrust coefficient C_{fg} ranging from 0.9409 to 0.9532. A reduced-order model was extracted, which was able to match metrics calculated in an example computational case to within 3.33 percent. An optimization scheme was input to Design-Expert® software (Stat-Ease, Inc.) to determine the best-performing mixer, and this became the basis geometry for the study performed in phase II.

In phase II of the mixer study, commonly used geometric features of scarfing and scalloping were added, using four geometric parameters to describe them. The aero performance impact of using scarfing and scalloping techniques was not very strong, with values of thrust coefficient ranging from 0.9518 to 0.9541. However, temperature contours at the nozzle exit reveal that the underlying mixing mechanisms are changed by varying the design parameters. The lessons learned from these studies were used to inform the designs delivered for high-fidelity predictions.

Computer code called Supersonic Parametric Nozzle Design (SPAND), written in the Python® language (Python Software Foundation), was developed to automatically generate supersonic nozzle geometries and grids for this design application from an input parameter set. Inputs dictate all nozzle dimensions, not just mixer parameters. The code leverages the pyGlyph API in the Pointwise® grid generation software (Cadence Design Systems, Inc.), and was used in its various stages of development for the published mixer parametric studies. Future work aims to develop the code further into a distributable module with a larger parameter suite and postprocessing capability.

3.2.2 Development of Thrust Validation Capability

A thrust measurement rig has been installed with the open jet facility in the test cell CW17 at NASA Glenn (Figure 16). A floating plenum chamber is fed radially with compressed air and axial thrust is measured by a load cell. Thrust is obtained from measured forces using calibration data from ASME standard nozzles. After several iterations and stages of improvement, the rig provides thrust coefficient data with enough accuracy for comparisons with parametric variations. An example data set, compared to computational fluid dynamics (CFD) predictions, is shown in Figure 17. Here, a 16° conic plug is used and the crown location relative to the cowl exit is varied by attaching cylindrical lip-extension pieces of different length. As can be seen, the comparison of the data trends between the experiment and CFD are reasonably good. The rig is still not adequate for providing absolute thrust coefficient with good accuracy. Efforts are underway for improvement.

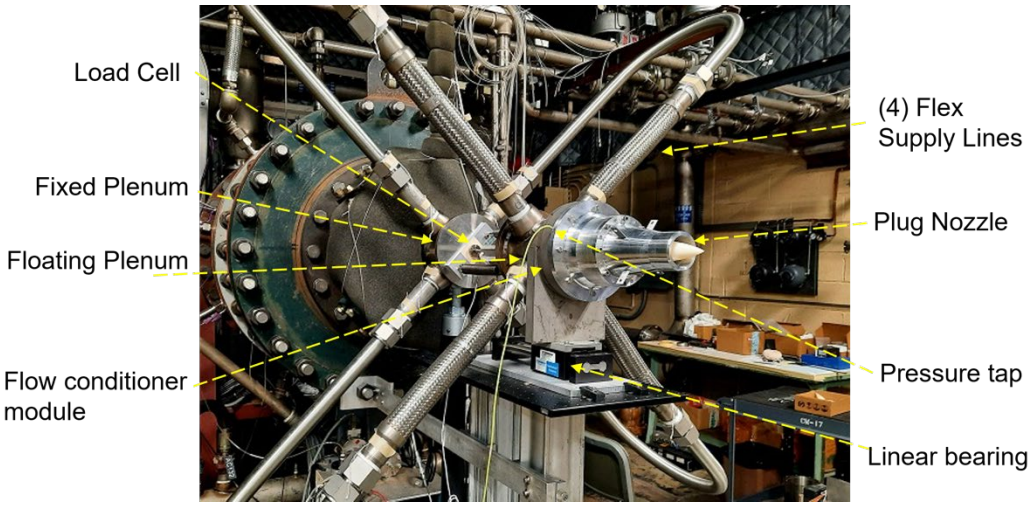


Figure 16.—Thrust measurement apparatus in ERB CW17. Plug nozzle with cylindrical cowl is mounted.

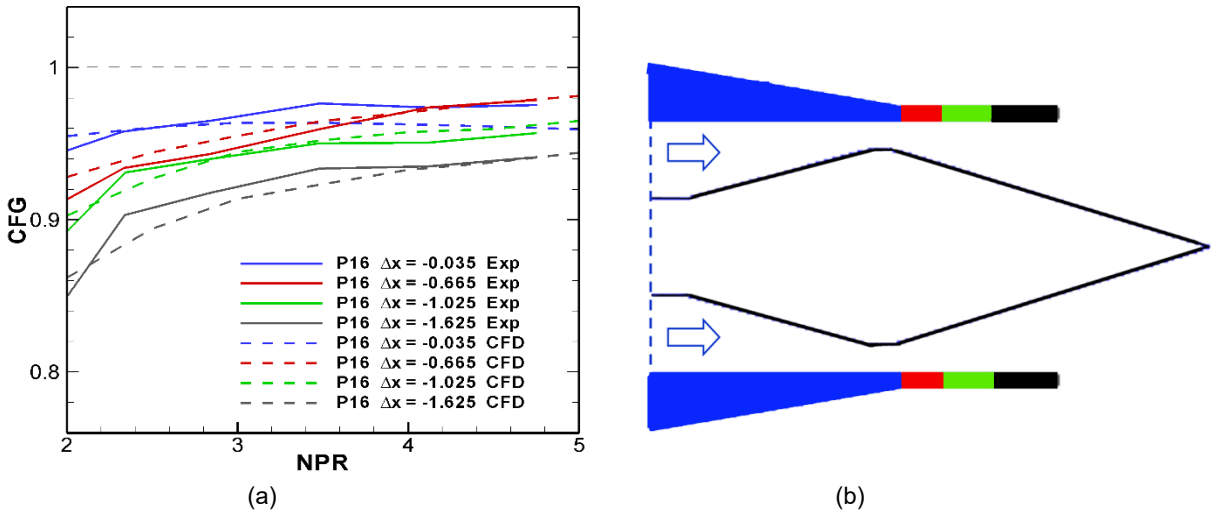


Figure 17.—Thrust coefficient of 16° conic plug for different lip extensions. (a) CFG versus nozzle pressure ratio (NPR); solid lines: experimental results, dashed lines: CFD results. (b) Schematic of four lip extensions (corresponding plug crown locations relative to cowl exit, △x, are indicated in the legend of (a)).

In addition to measuring thrust of the plug nozzles, the small jet rig in CW17 was used to screen concepts for acoustic impact. Although the facility is not anechoic, the changes in sound level are usually reliable indicators of the results to be found in an anechoic facility. For example, the three optimized plug shapes were evaluated and their far-field acoustic spectra at 90° compared (Figure 18). The plot generally confirms the expectation that plug shapes without separation should be quieter. It also confirms that the trade-offs made in performance for the compromise shape produced significant acoustic benefits for the small loss in cruise performance.

Other acoustic explorations undertaken in CW17 include porous plugs for shock noise reduction and porous surfaces on the nozzle to forestall separation in a contracting-diverging nozzle operating at subcritical pressure ratios. Although it is expected that engine cycles at LTO conditions will have to be subcritical, that is, without shocks in the plume, being able to slightly increase the pressure ratio without incurring the dramatic onset of shock noise might be beneficial in some designs. Parametric tests of porosity (porosity, hole size, placement, plug length, etc.) were undertaken with additively manufactured plugs to understand how the shocks and noise were modified (Refs. 34 to 36).

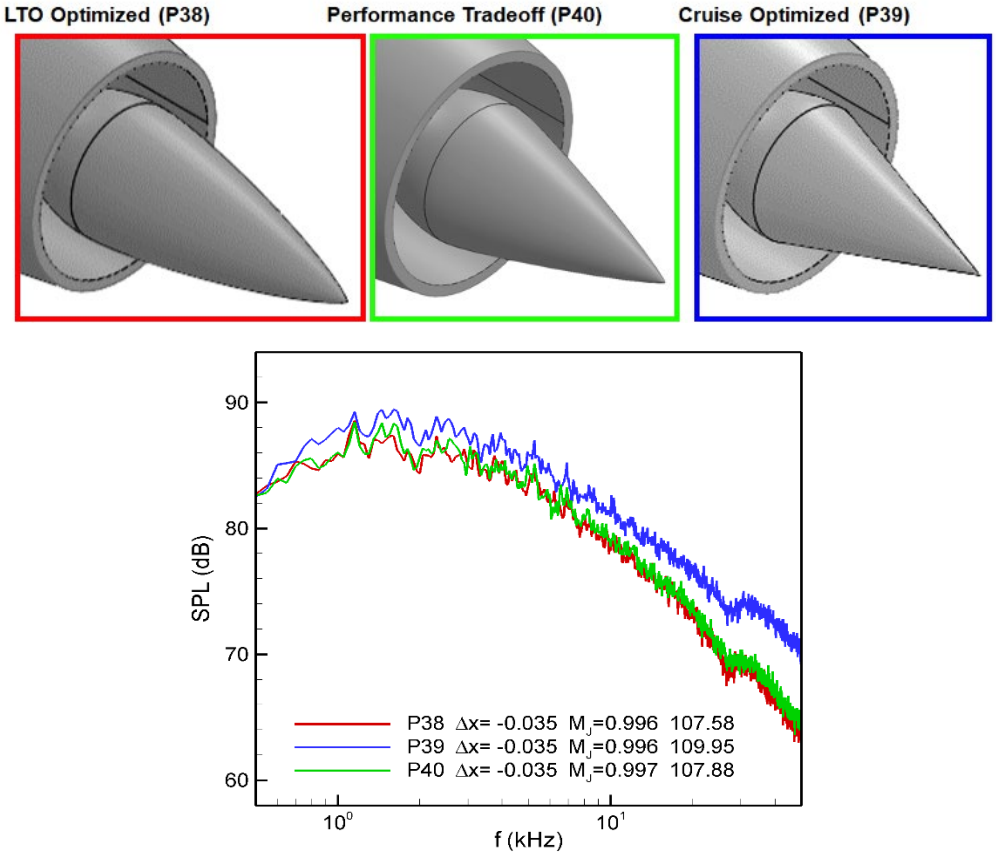


Figure 18.—Sound pressure level (SPL) spectra at polar angle 90° for three plugs developed in plug optimization study.

Because cruise performance is the most critical requirement for the exhaust nozzle, it must have near-ideal divergence while at cruise. However, at LTO flow conditions, such a geometry will separate in the divergent section, which results in extra noise production. This is why an actuated nozzle, such as the translating cowl design, is required for supersonic aircraft. But if the separation in the divergent section could be mitigated in a way that required less mechanical complexity and weight, then the nozzle could remain fixed without noise penalty and the reduction in weight would make a significant improvement on the overall aircraft performance. Again, porous surfaces, both on the nozzle and on the plug, were investigated in the regime of overexpanded flows as a noise reduction concept. The results were significant enough to file patent disclosures and to warrant further study.

3.2.3 Final Designs

A notional engine design (Figure 19) was created to size components and justify design assumptions. The nozzle designs ultimately provided for LES analysis differed in their configuration from that used in the mixer performance studies. The mixer studies were performed with a constant area duct, while an engine has a sizeable centerbody at the turbine rear frame, which typically is reduced in diameter to allow lower velocities in the mixer nozzle pipe. The STCA NPSS input deck provided target values for mass flows and total pressures for both streams, and the GE SuperFan design provided a target value for the cowl outer diameter. Neither of these specifies the bypass duct annulus around the core of the engine. To establish upstream duct geometry, a combination of Mach number limits and current practice was employed. Working inward, the fan duct outer radius was set by continuing the SuperFan nacelle design. The fan duct area, and thus the inner fan duct radius, was set based on a maximum duct Mach number of 0.4 required to keep duct losses low. The outer core stream duct radius was set by allowing a 2.25-in. annular outer flange on the turbine rear frame. The duct Mach number limit of 0.4 set the inner radius of the turbine rear frame.

Moving downstream, the delivered plug stem design included a divergent section, coincident with the mixer, to more accurately represent the transition from turbine rear frame to nozzle duct. The delivered design was assessed for possible flow separation sans mixer and determined to be low risk. At the downstream end of the duct, the inner stem expands to become the external plug while the inner duct radius shrinks to allow room for actuation and LTO stowage of the cowl extension. Towards the exit of the duct, the nacelle outer radius decreases, bringing the trailing edge lip, which includes the cowl extension, down to the trailing edge lip thickness of 3/8 in. Plug throat radius was determined from the required throat area at LTO conditions.

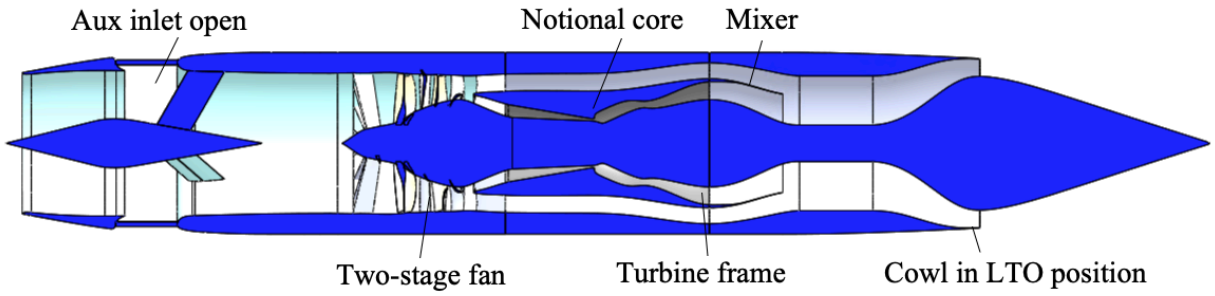


Figure 19.—Flow lines for benchmark SuperFan engine in LTO configuration with axisymmetric mixer for clarity.



(a) (b) (c)

Figure 20.—Three mixers designed for high-fidelity simulation. (a) Benchmark 12-lobed mixer. (b) 20-lobed variant. (c) Vortical variant.

Inside the duct, the required Area Ratio (AR) between streams was determined from a combination of an analytical model, as given in Reference 37, and empirical corrections informed by CFD (Ref. 32). A baseline nozzle was generated with an axisymmetric splitter, which was assigned a trailing edge thickness of 1/8 in. to provide an assumed level of reasonable structural support.

Three mixer designs were delivered for LES analysis on this full-scale platform, shown in Figure 20. Two were parallel mixers, which bore higher lobe penetration factors and had trailing edges running parallel to the flow direction. These were intended to generate mixing via increased shear layer surface area between the core and bypass streams. A 12-lobe and a 20-lobe design were delivered using this base design. The final mixer was a vortical mixer, which bore a lower lobe penetration factor but had trailing edges flared out to 22° to the flow direction. This design was intended to mix flow via increased axial vorticity generated by imparting contrary radial velocities to the core and bypass flows, while reducing the physical footprint of the mixer itself.

3.2.4 Lessons Learned in Exhaust System Design

Several significant lessons were learned in the design efforts for the exhaust system:

- The bypass ratio of the exhaust system is very sensitive to the extraction ratio, the ratio of bypass to core pressure ratios. The area ratio of the bypass and core ducts is a very important part of this sensitivity.
- The divergence of the duct area from the turbine frame to the mixer exit plane must not be made too strong or the flow will separate in the duct.
- The divergence of the lobe walls must not be too strong or the flow in the lobes will diverge. Keeping the area ratio constant over the lobes helps.
- The axial profile of the duct downstream of the mixer can influence the bypass ratio. For example, if the contraction is on the nacelle side of the duct, the bypass stream may feel a backpressure and bypass ratio will be less than when an external plug is used and the contraction is on the core stream side of the duct. For the external plug nozzle, the core stream is back-pressured and the bypass ratio goes up. The closer the contraction is to the mixer exit, the more this effect is noticed.

3.3 Airframe Design

The most obvious shortcoming in creating a representative commercial supersonic aircraft for this study was the lack of open, representative airframe concepts. Most concepts were created with cruise efficiency as their focus and rarely have low-speed features such as landing gear, flaps, and other high-lift devices with sufficient geometric fidelity for a study of airframe noise. Because of the dearth of designs and therefore lack of experimental and computational studies, very little is known about airframe noise sources and their contribution to far-field noise for this class of aircraft.

Given the typically poor low-speed aerodynamic characteristics of a supersonic aircraft, design and implementation of efficient high-lift devices to this class of transport are key to maintaining reasonable landing speeds, which in turn impact directly the vehicle's overall airframe noise level. Yet, no clear understanding of what a representative landing speed range for this class of transport can be found in the open literature. Depending on aircraft weight, a typical subsonic transport lands at a velocity (V) between 140 and 150 kts, with the airframe component of total noise scaling with velocity to the sixth power (V^6). An increase of 20 percent in landing speed for supersonic aircraft would cause a 5-dB increment in airframe noise levels. Therefore, assumptions made on the relative importance of airframe noise for supersonic vehicles during landing need to be justified by quantitative studies.

The STCA airframe design used in ICAO studies and in our uncertainty assessments did not have high-lift features detailed, only a nominal lift augmentation specified to allow reasonable trajectories to be calculated, thus establishing nominal landing speeds. As initial predictions of airframe noise using these trajectories were found to be significantly lower than that of the propulsion noise, the uncertainties in the prediction of the airframe noise were not expected to impact the uncertainty of the total aircraft noise prediction. However, an effort was made to justify, if not validate, the prediction methods used to make this assumption. Details of that effort are given in Section 6.0.

4.0 Fan Noise Model Development—Simulation and Modeling

4.1 Simulation Tool Description

A complete computational simulation capturing all the relevant physics over the entire necessary domain is outside the scope of the available resources at this time. Instead, a series of connected tool paths was used, with each tool covering a specific aspect of the simulation and exporting the relevant solution components to the next tool. This is discussed in Reference 54 but will briefly be summarized here. A number of variations on this toolchain were tried, but the final workflow is shown in Figure 21.

The inlet and fan geometry and the engine operating conditions are used to define a set of simulations. A steady RANS simulation is run for the incoming flow into the inlet, matching the engine operating conditions. In the latest version of the toolchain, the RANS code FUN3D (Ref. 55) was used for this step as its unstructured grid accommodated geometric details and its output matched the input requirements of the subsequent tools. The flow solution is then fed to parallel workflow paths.

The turbomachinery branch of the toolchain uses the external flow simulation as its upstream boundary condition for the commercial code Fidelity Fine Turbo (Cadence Design Systems). A steady RANS solution is first computed through the turbomachinery. Next, a specialized version of an unsteady RANS (URANS) solver, which solves a Fourier-decomposed version of the flow field as a perturbation on the URANS solution, is run. This yields unsteady pressure fields that contain the acoustic waves from the rotor-stator interactions—the fan tones. This solution then sampled at a plane inside the inlet just upstream of the fan system and handed to an acoustics simulation for propagation to the far field.

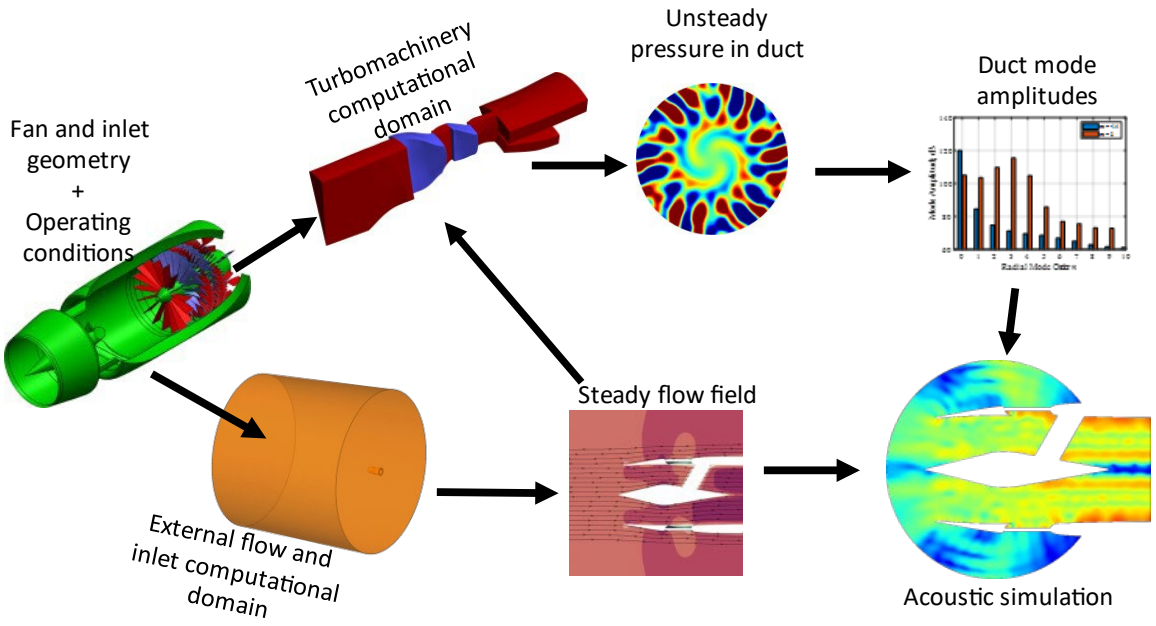


Figure 21.—Fan noise workflow.

The far-field propagation portion of the toolchain solves the convected wave equation for the flow field given by the RANS simulation of the inlet with an unsteady source (duct mode amplitudes) specified by the URANS of the turbomachinery. Attenuation by an acoustic liner in the inlet duct is also considered in this step. The commercial code Actran (Hexagon AB) was used to solve the wave equation, yielding the acoustic waves at the far-field observer locations required for aircraft noise prediction.

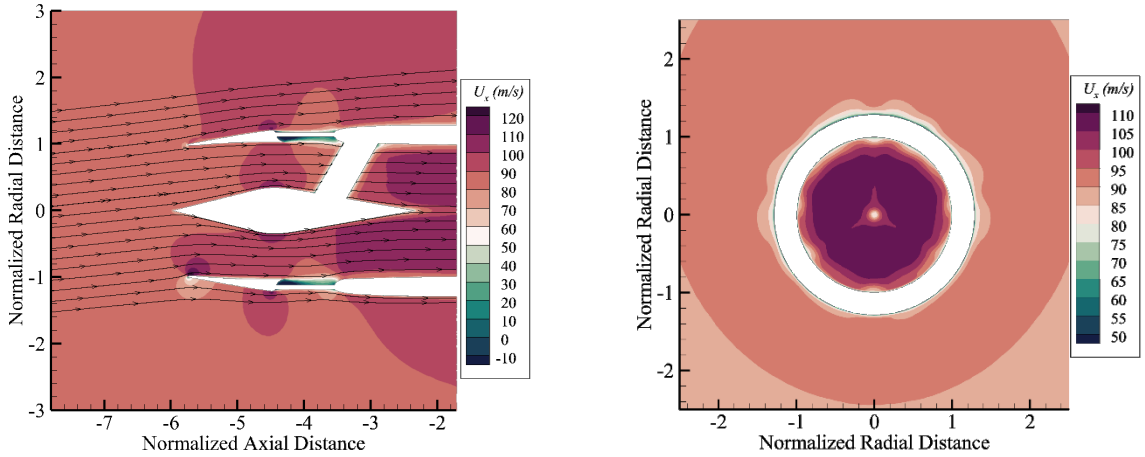
4.1.1 FUN3D

The steady RANS inlet flow field used as input for both URANS of the fan stages and for the subsequent propagation of sound was computed using the NASA code FUN3D. The mesh used for the simulation was created using Pointwise® grid generation software (Cadence Design Systems) and contained about 69 million cells. The approach and lateral flight conditions were interrogated with and without an angle of attack. Furthermore, simulations with and without the cowl actuators and centerbody spike supports for the 0° AoA cases were also conducted to determine what effect, if any, the supports have on the flow upstream of the fan stacking axis. Figure 22 is the mean flow velocity for the approach case, corresponding to a Mach 0.26 external flow with and without a 5.2° AoA.

This is one of six cases run, for two different fan speeds, two different angles of attack, and two different external flow speeds. In all cases, the flow was well attached and showed similar characteristics inside and outside of the nacelle. However, at angle of attack, the streamlines show that some of the flow near the lower part of the nacelle inlet is diverted into the duct. The flow rate inside the duct upstream of the fan stacking axis for both cases is very similar and symmetrical, providing very similar inflow conditions. Both runs show that the flow is largely attached through the inlet with the exception of downstream of the forward cowl.

4.1.2 Fidelity Fine Turbo

Due to the large disparity between the aerodynamic and acoustic scales involved in the fan-inlet systems, it was mathematically more tractable to decouple and treat the fan and inlet separately. In this work, they are decoupled in the acoustic sense. The aerodynamic coupling is retained by imposing the



(a) (b)

Figure 22.—Flow solution for axial velocity for approach condition. (a) With no angle of attack. (b) At angle of attack.

inflow distortion from the inlet (computed by steady RANS code) as a boundary condition on the fan. The modeling approach used here is a synthesis of high-resolution unsteady Reynolds Averaged Navier-Stokes (URANS) simulations for the fan source noise prediction, and computational aeroacoustic (CAA) simulations for the inlet noise propagation to the far field. The initial focus has been on the fan inlet tone noise, but, in principle, the methodology is applicable to the fan exhaust tone noise as well, provided that the acoustic propagation through the mixed flow of the exhaust system can be computed.

A full URANS simulation that is adequately resolved to provide the necessary accuracy of the acoustic perturbations in the vicinity of the fan stage is very computer-resource intensive and not practical for the purposes of this study. As a work-around, we relied on an approximation of URANS known as the nonlinear harmonic (NLH) method. In the NLH approximation, only a preselected set of frequencies are tracked in the simulation, which results in significant reductions in the computational resource requirements. For most applications, it is sufficient to retain the first three harmonics of the blade passing frequency of each blade row. The particular implementation of the NLH that was used in this work is that incorporated into the commercial turbomachinery aerodynamic software package called Fidelity Fine Turbo. It is a density-based URANS solver that incorporates a number of spatial numerical schemes, including finite-difference and upwind, and temporal schemes such as explicit time-marching Runge–Kutta. It features a number of convergence acceleration strategies, including local time-stepping, multigrid, and implicit residual smoothing. It offers a menu of optimized turbulence models and is a Message Passing Interface (MPI)-parallelized code.

4.1.3 Actran

The acoustic portion of the pressure perturbation field is quantified by using the Actran iTM tool. This utility extracts pressure and velocity on a plane and reconstructs a full wheel. The result of this process for the approach condition is shown in Figure 23. As discussed in the companion report to the present report (Ref. 56), the most important interaction noise source was determined to be between the inlet guide vanes (IGVs) and rotor 1. These blade rows have counts of 17 and 20, respectively. This interaction leads to strong interference patterns of orders 3 and –14, with the negative sign indicating rotation in the opposite direction from the rotor. The patterns of 3 and 14 are apparent by inspection of

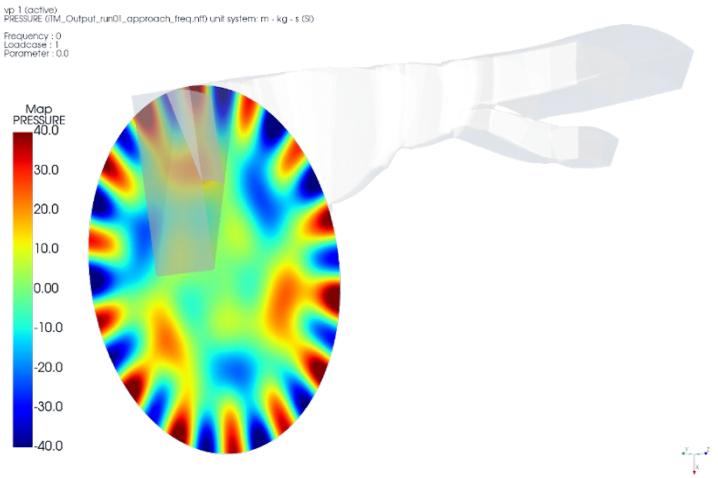


Figure 23.—Full wheel reconstruction of blade passing frequency 1,511 Hz at approach.

Figure 23. The reconstructed full wheel is used by Actran iTM to quantify the duct mode amplitudes using the single-plane pressure-velocity (SPPV) method described in the Actran manual (Ref. 57).

The output of Actran iTM is a table of radial and azimuthal duct mode complex pressure amplitudes, including upstream and downstream traveling components. These complex pressures are used as the boundary conditions for the subsequent acoustic simulations.

Acoustic simulations presented here were conducted using Actran 2022 (Ref. 57) employing the Actran TM turbomachinery workflow. The frequency domain method solves the Möhring Analogy, which is the Navier-Stokes equations rewritten as a wave operator on enthalpy. It handles convected acoustic waves in cases where the flow is reversible, adiabatic, and irrotational. The solution is found with a matrix inversion method. The 2D inlet geometry was wrapped in a semicircular domain of 3.4 m (135 in.) radius, centered on the midpoint between the front inlet and auxiliary inlet. This domain topology was chosen as providing a largely reflection-free computational domain when using the infinite element boundary condition. A quadratic grid with element size of 8 mm (0.315 in.) gives four points per convected wavelength up to the frequency of about 4,500 Hz, depending on the local flow speed. This results in approximately 550,000 elements and solution times on the order of a minute per frequency on a laptop. An arc of virtual microphones at 46 m (150 ft) gives the sound radiation in the far field. Actran uses an *infinite element* method to model the sound radiation from the finite element domain through a uniform medium to the specified field points. For the present simulations, these virtual microphones are in a flow convecting with the flight speed of the inlet. The layout is shown in Figure 24.

The acoustic content, extracted from the URANS simulations using the Actran iTM tool, can now be used as the modal input (i.e., boundary condition) at the fan face. The corresponding radiation simulations provide a series of sound maps like that shown in Figure 25. In this case, the real part of the pressure is plotted with 11 input radial modes included simultaneously and with their respective phases preserved. The richness of the wavefield hints at how difficult it is to approximate the propagation of duct modes through complex inlet geometry without an accurate solver like Actran. Even getting the balance of sound power propagating out the auxiliary inlet relative to the main inlet right would not be easy, much less getting the phase between the two correct to find the nulls in the far field where the two paths destructively interfere. In fact, getting the directivity correct is very difficult because of the importance of phase with multiple paths.

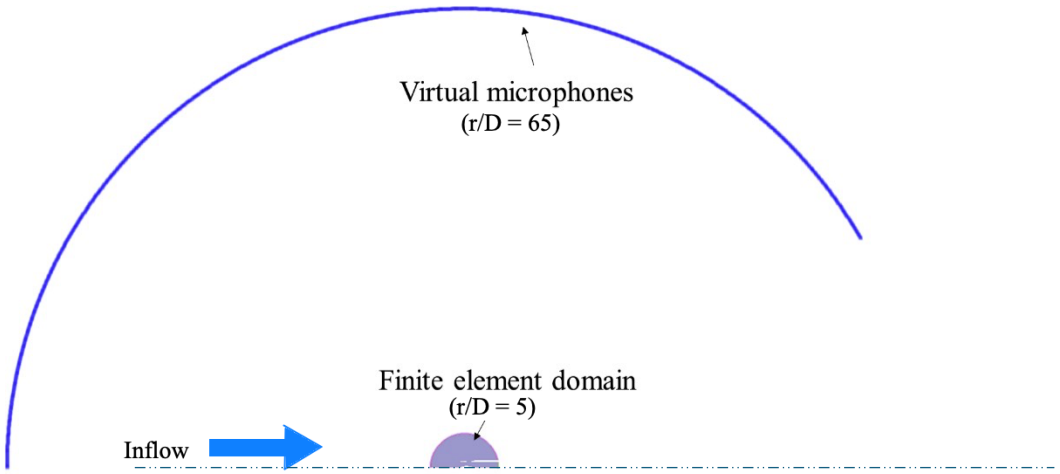


Figure 24.—Actran computational domain.

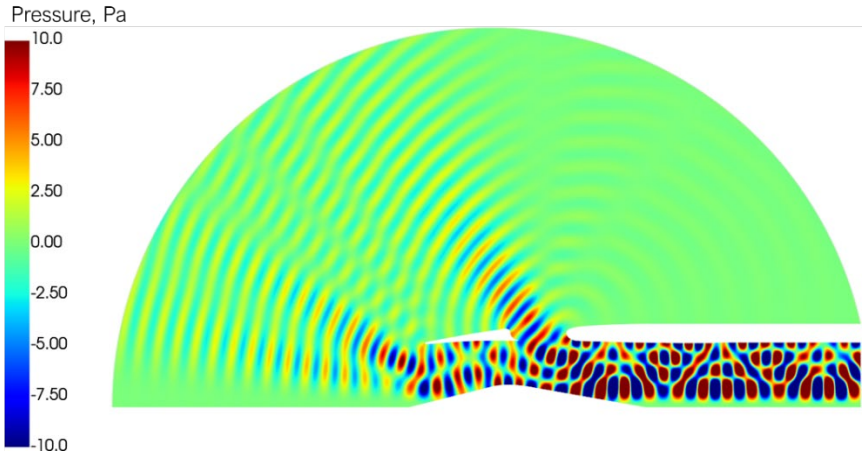


Figure 25.—Real part of frequency domain peak-to-peak complex pressure for approach conditions, azimuthal mode m = 3, blade passing frequency 1,511 Hz.

The simulated far-field tonal amplitude for the approach operating condition is shown in Figure 26. The upstream radiated noise (along the axis near 0°) is dominated by the $m = 3$ contribution. At approach, the radiated sound peaks at an angle of 50° and at an amplitude of 80 dB. Results for other operating conditions are presented in Reference 58. At cutback and sideline conditions, the levels are approximately 20 dB higher and more forward-radiated. Inlet levels for all conditions fall off rapidly for angles past 90°. These predictions can be used in system noise analyses where an aircraft trajectory is used to predict sound observed by a receiver on the ground. All cases presented in this reference were simulated with axisymmetric inflow and no additional noise due to distortion.

4.2 Validation Exercises for Fan Noise Toolchain

4.2.1 Summary of SDT Validation and External Review

The accuracy of the NLH approach was assessed using the Source Diagnostics Test (SDT) fan stage for which aerodynamic and acoustic wind tunnel data exist (Refs. 59 and 60). The SDT fan had 22 rotor blades and 54 stator vanes. Figure 27 shows an illustration of the SDT fan stage and the associated NLH computational domain. The simulations were carried out for a range of fan tip speeds and the results were

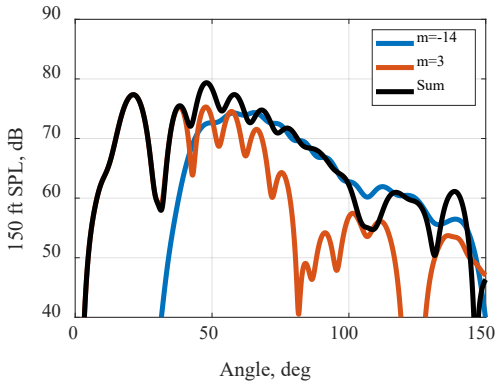


Figure 26.—Far-field tone amplitude predicted versus inlet polar angle for blade passing frequency (BPF) at approach condition.

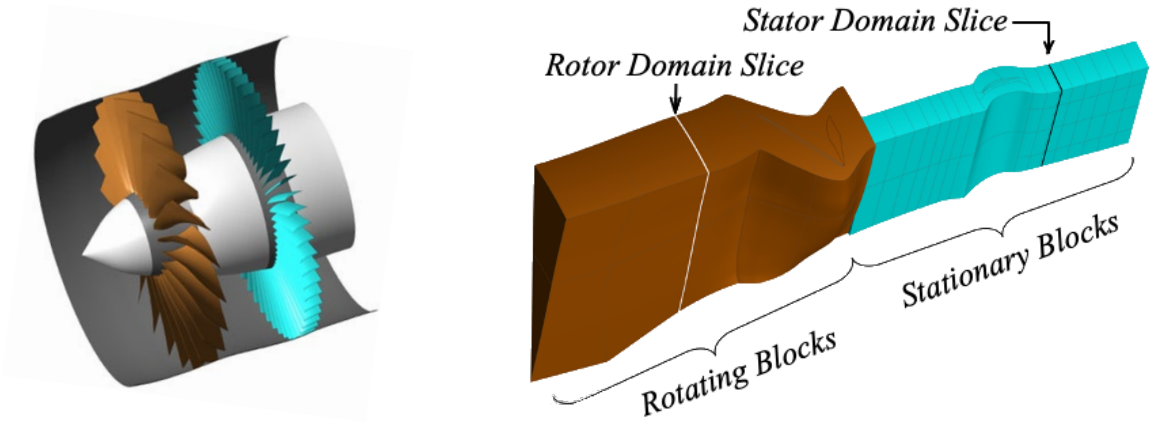


Figure 27.—SDT fan stage (left) and corresponding NLH computational domain (right).

analyzed to establish the accuracy and robustness of the simulations for predicting the acoustic content. These are summarized in Reference 54. The NLH simulation results (in the form of the CGNS files) are provided to the inlet team for use with Actran, the acoustic propagation code used in this work.

A presentation based on this physics-based fan noise prediction work was given to a two-person external review panel in February 2023. The panel concurred with our proposed workflow but cautioned that some aspects of the total fan noise source are beyond our present scope of work. They emphasized the importance of experimental testing and validation of simulations on relevant geometry.

4.2.2 Liner Property Investigation Using COMSOL

To demonstrate the inlet noise prediction capability with an acoustically lined inlet, the Advanced Ducted Propulsor (ADP) was chosen as the candidate to compare with simulations. Due to the limited knowledge of the liner properties for the ADP test from 1995/1996, design reports were used as geometry inputs to a COMSOL Multiphysics prediction code used to compute the acoustic liner impedance (Ref. 61). These values were then compared to the published optimum and full-scale impedance values to determine viability of this predicted impedance. ADP's single degree-of-freedom liner contained a 112 Rayl wire mesh facesheet over a 0.312-in.-deep Nomex® (DuPont Safety & Construction, Inc.) honeycomb with a cell width of 3/16 in. The two degrees-of-freedom liner utilized a 3/16-in. honeycomb

with a total depth of 0.307 in., a 68 Rayl wire mesh septum located at 0.227 in. above the backing cavity, and a 78 Rayl wire mesh facesheet.

The COMSOL Multiphysics simulation was set up to reduce the impedance in accordance with NASA Langley Research Center's Normal Incidence Tube (Ref. 62). An overall sound pressure level of 120 dB was used to propagate one-third-octave band frequencies from 50 to 10,000 Hz. The facesheet model implemented was the Two-Parameter Model, which includes linear and nonlinear contributions in the DC flow resistance (Refs. 63 and 64). A diagram of the simulated normal incidence tube is shown in Figure 28.

The results from the simulation, as compared against the design intent, are given in Figure 29 while more discussion can be found in Reference 65, along with the detailed description of this validation effort. The full-scale impedance data is not available at lower than 3,000 Hz due to the design frequency range on the full-scale fan model. The predicted normalized reactance match was, on average, within 1 percent of the scaled normalized reactance, but the normalized resistance is underpredicted by 58 percent compared to the scaled normalized resistance. As a note, it would be possible to use a portable impedance meter and measure the impedance directly on the nacelle, but the wire mesh facesheet and septum have likely degraded over time and would not reflect an accurate measurement of what was designed and used for the test 26 years earlier. Because it was not possible to obtain a more accurate value for the as-tested impedance for the 2DOF liner, the simulated values were used for the liner properties in the propagation simulations.

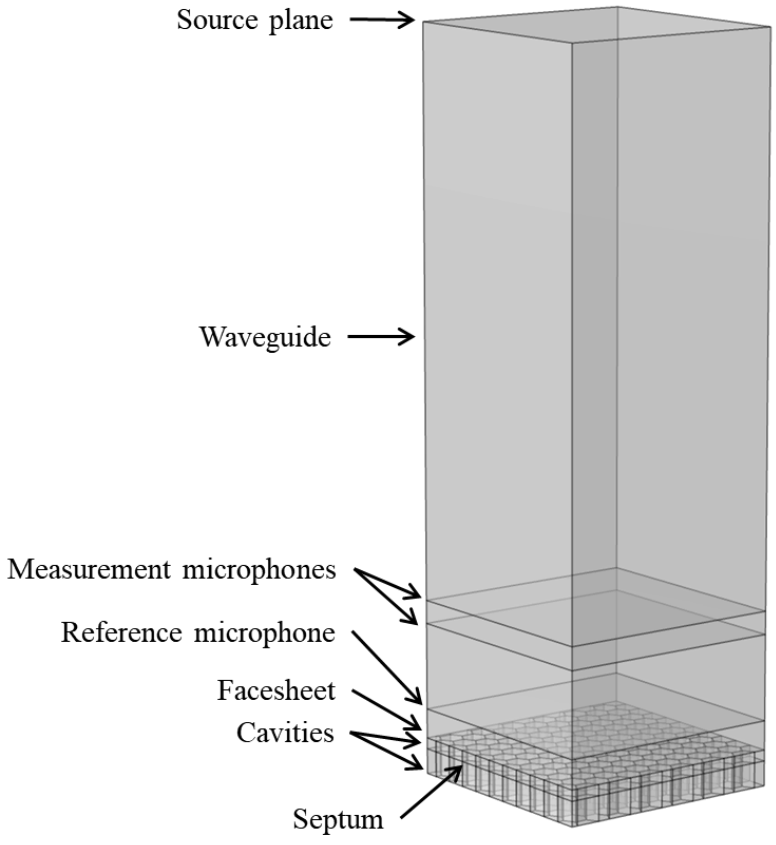


Figure 28.—COMSOL Finite Element Model of normal incidence tube at NASA Langley Research Center in Liner Technology Facility used for computing impedance of acoustic liner.

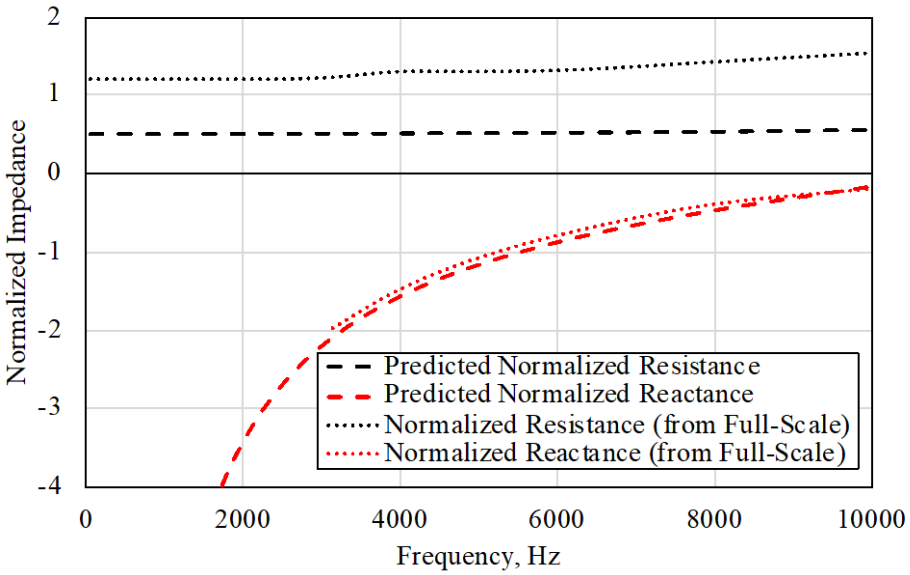


Figure 29.—Comparison of normalized impedance values for two-degrees-of-freedom liner in ADP test, documented design intent from full-scale versus predicted from measurements of test hardware.

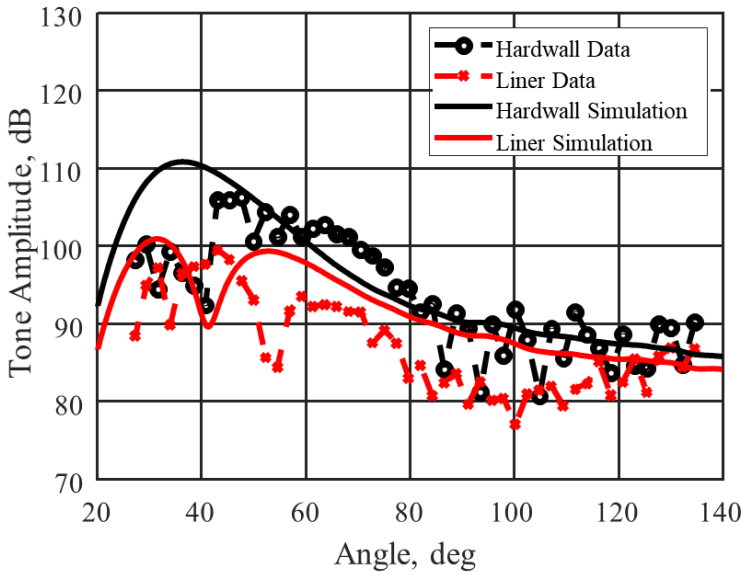


Figure 30.—Comparison of measured and simulated hardwall versus acoustically lined two-degrees-of-freedom inlet liner, ADP fan at 5,425 rpm.

The workflow to perform simulations of lined inlets is similar to the previously described fan inlet noise workflow except that the sound source comes from a different simulation, as described in Reference 65. The prediction method was found to work reasonably well, with a good example given as Figure 30.

In summary, the predicted attenuation of the liner agreed quite well on a sound power basis, as shown in Figure 31. Similar results were found for the single-degree-of-freedom liner, not shown here. By taking the standard deviation for this new data set, including both the SDOF and 2DOF lined cases, the error standard deviation is 3.2 and the average delta is 2.3 dB.

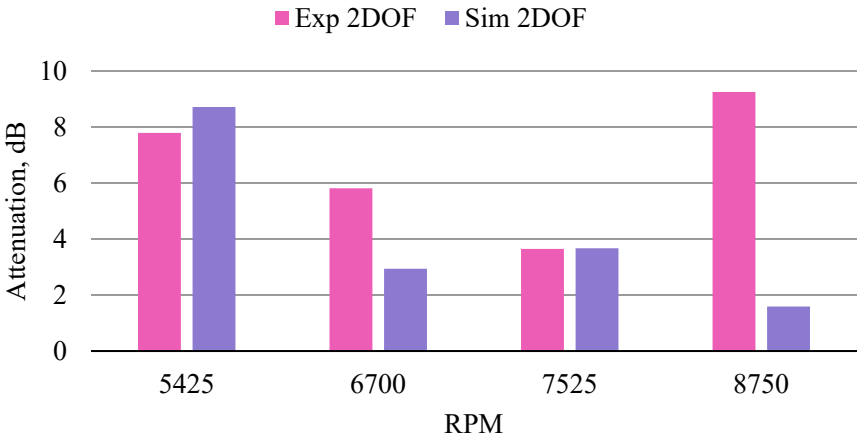


Figure 31.—Comparison between experiment and simulation of two-degrees-of-freedom liners for ADP fan at four speeds.

4.3 Simulations of SuperFan and Variants

In discussions with acousticians in industry, a few questions about fan noise from supersonic propulsion were commonly raised:

- What noise will the distortions from the centerbody and its struts, and from the auxiliary opening and its actuators produce?
- Will the strut and actuator count impact the noise like rotor and stator counts do?
- What is the impact of angle of attack on these inlets with multiple openings?
- What is the noise sensitivity of the close rotor-stator spacing of a two-stage fan?
- Will noise from the second rotor-stator be heard coming from the inlet through the first stage or can it be ignored?

Only one known acoustic test has been performed on a multistage fan (Quiet Supersonic Propulsor, or QSP, in 2002) (Refs. 14 and 66) and that was operated with a simple conventional inlet. Data from the QSP test was not analyzed due to budget and programmatic issues, thus the simulation and analysis of the SuperFan is very important for the development of supersonic propulsion. If these supersonic-specific features are critical, then empirical fan noise models must incorporate them so that trades between inlet performance and noise can be reconciled at the system level.

To address these questions and provide the fan noise modeling effort with acoustic data, a succession of simulations were done on variations of the SuperFan design. First, under assumptions of axisymmetry, the impact of the auxiliary opening in the inlet on the fan noise source and its propagation out the inlet were investigated. Next, different nonaxisymmetric aspects, such as struts and actuators and angle of attack, were introduced and simulated. Finally, given the importance of rotor-stator spacing on the length of a multistage fan, the SuperFan geometry was stretched to change the location of the IGV relative to the first rotor.

4.3.1 Assessment of Inlet Distortion from Auxiliary Inlets on Tone Sources

As discussed in Section 4.1.2, the aerodynamic impact of the inflow distortion caused by the airflow through the auxiliary doors and around the struts and actuators is modeled as a boundary condition for the

fan NLH simulations. Using RANS simulations, the flow field around and through the inlet was computed and total pressure and total temperature profiles were extracted at the fan inflow domain, near the tip of the spinner (shown as the red dashed line in Figure 32). Examples of the computed total pressure contours are shown in Figure 32 for the 0° and 5° AoA at the approach condition. The wakes of the three inlet struts are visible in both contours, as are the subtle circumferential distortions caused by the four actuators of the translating cowl. For the AoA case, additional circumferential distortion is also visible around the circumference of the contour plot. Radial profiles of total pressure and total temperature as a function of circumferential angle were extracted and supplied as the inflow boundary conditions for the NLH fan stage simulations.

The NLH computational domain for SuperFan is shown in Figure 33, in which the blocks associated with each blade row are shown in different colors for clarity. Change of color from one set of blocks to the other represents the transition from one frame of reference to another, starting with the stationary blocks for the IGV shown in dark purple. This high-resolution grid, which contains one passage of each blade row, is comprised of roughly 19.8 million points. By contrast, the equivalent full wheel grid needed for a URANS simulation would have required 413 million grid points. The NLH simulations for SuperFan were typically run, computing the first three harmonics of the blade passing frequency for each blade row. For each operating condition of interest, average static pressure conditions were set at the bypass and core duct exit plane to achieve the total target mass flow rate for SuperFan at that condition. The resulting predicted mass flow split, as well as the fan pressure ratio in each simulation, were consistent with those supplied by General Electric.

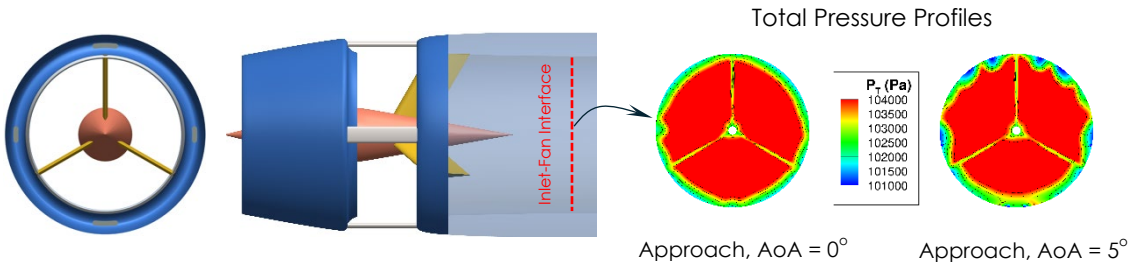


Figure 32.—Predicted contours of total pressure in distorted inflow upstream of SuperFan.

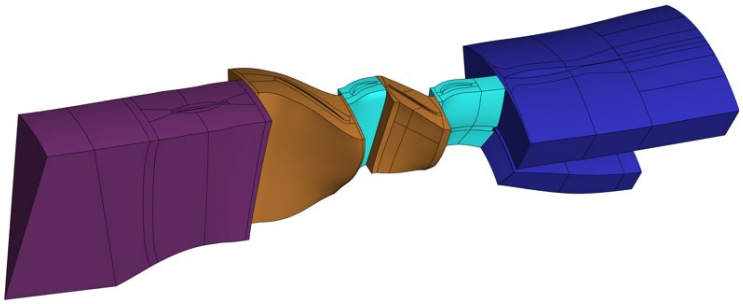


Figure 33.—SuperFan NLH computational domain with various blade row bocks highlighted. Spinner and IGV block is dark purple, rotor blocks are brown, and stator blocks are cyan. Exit duct is dark blue.

The SuperFan simulations took around 76 h to run for 4,000 iterations to achieve convergence of the relevant criteria. The flow solutions include a large set of the mean flow and thermodynamic variables as well as the real and imaginary parts of the associated harmonic perturbations. An example of the simulation results for the real part of the harmonic pressure perturbations is shown in Figure 34 for an axial slice of the computational domain just upstream of the spinner nose at the sideline operating condition with open auxiliary doors and the inlet at 7° AoA. The 1×BPF harmonic pressure perturbations are clearly dominant upstream of the IGV and are in the range from –500 to 500 Pa. The corresponding 2×BPF harmonic levels are an order of magnitude smaller, and the 3×BPF harmonic levels are much smaller yet and from –1 to 1 Pa. The dominant propagating Tyler-Sofrin circumferential modes at 1×BPF are $m = +3$ and $m = -14$. These modes are clearly discernable in the contour plots for 1×BPF showing a 14-interlaced pattern in the outer portion of the contour surrounding a 3-interlaced pattern in the inner region. There are, of course, several other propagating circumferential orders at this frequency, but they are much weaker and do not contribute significantly to the total sound pressure level at 1×BPF.

The simulation process has been documented in much more detail in Reference 67.

To investigate the impact of the inlet components on the inflow distortion noise levels generated by the fan, a parametric study was carried out by systematically removing various hardware components of the inlet and running NLH simulations with the resulting inflow distortion patterns. The configurations studied are depicted in Figure 35. Part (a) shows the baseline configuration in which the translating cowl is removed; it is essentially a conventional axisymmetric inlet causing no inflow distortion. Part (b) depicts the complete inlet with the translating cowl in the forward position, so the auxiliary inlet doors are fully open. This configuration represents the most realistic inlet configuration for LTO operability. Part (c) is the same as the full inlet but with the inlet centerbody struts removed.

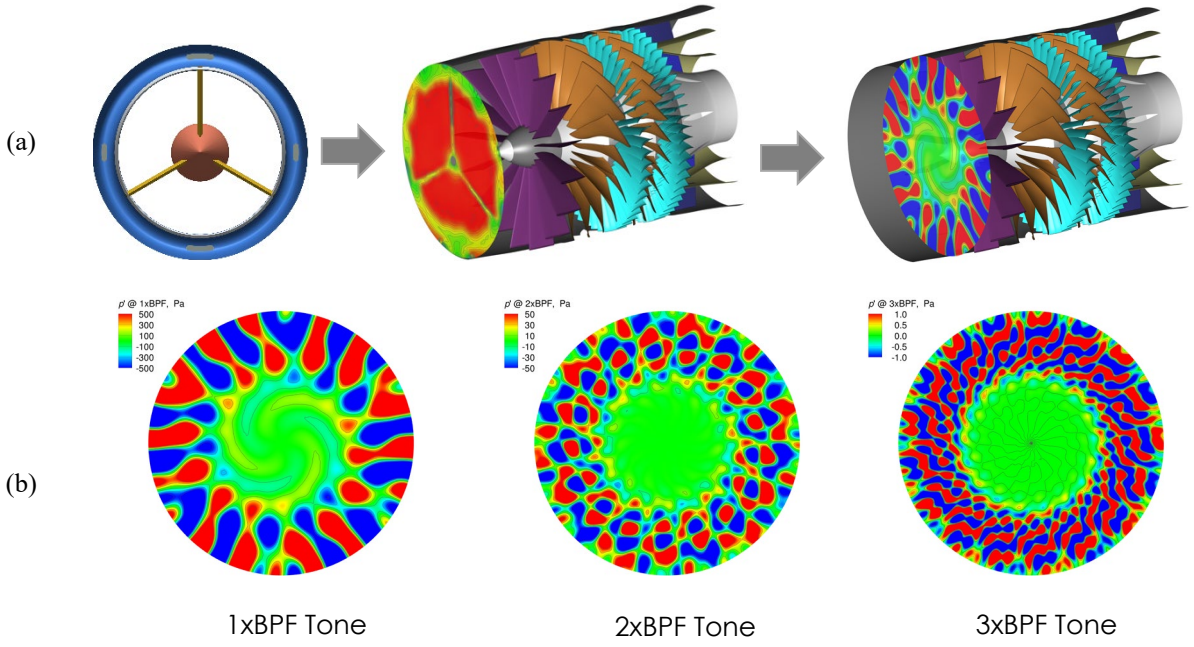


Figure 34.—NLH simulation steps for SuperFan subject to inlet flow distortion. (a) Inflow distortion profile is boundary condition for fan simulations. Example of resulting harmonic pressure perturbations upstream of IGV. (b) Contours of real part of pressure perturbations for first three harmonics of blade passing frequency.

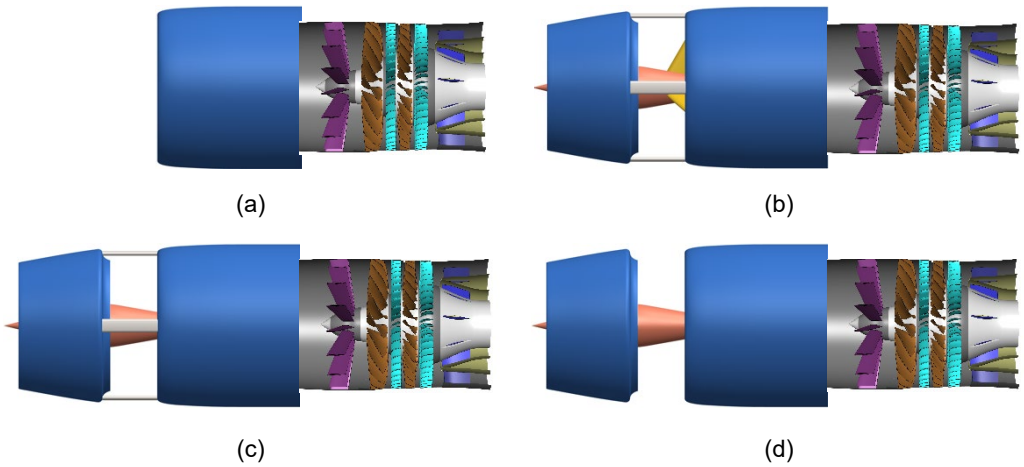


Figure 35.—Inlet configurations investigated. (a) Configuration 1: axisymmetric baseline inlet configuration with all hardware removed. (b) Configuration 2: complete inlet configuration with inlet cowl in forward position. (c) Configuration 3: same as (b) but with centerbody struts removed. (d) Configuration 4: same as (c) but with translating cowl actuators removed.

Part (d) is the inlet without either the centerbody struts or the inlet actuators. Simulations were run with and without an AoA for each configuration except for the baseline configuration, which was run only at the 0°AoA to serve as the reference noise level. Two fan operating conditions were considered: approach and sideline. The inlet AoA for approach is 5° and for sideline is 7°. In all cases, the first three harmonics of the blade passing frequency of each blade row were included in the simulations. Acoustic contents were extracted at an axial location just upstream of the spinner nose in order to compute a first-order estimate of the impact of the various inlet configurations on the inlet source acoustic tone levels. A more accurate estimate is obtained by propagating the computed acoustic field through the inlet and its auxiliary doors to calculate the impact on the far-field noise level.

Given the large number of propagating radial modes present, acoustic power level was deemed the best metric for judging the impact of the various inlet configurations on the noise source levels. By computing the acoustic power for all the inlet configurations shown in Figure 35, the influence of the various contributors to the inflow distortion noise can be explicitly shown. The results are summarized in Figure 36. In this figure, the baseline acoustic power level is shown as black bars. The acoustic power levels for the inlet configurations (b) to (d) are shown as colored bars. For the 0 AoA cases, they are shown as yellow, orange, and brown bars. The corresponding cases for the AoA cases are shown as light, medium, and dark blue bars. The results for the approach case are shown in the top part of the figure and those for the sideline condition in the bottom part. For each operating condition, the power levels for the blade passing frequencies 1×BPF to 3×BPF are plotted. The introduction of the inflow distortion generally increases the inlet noise levels as was expected. Note that for the sideline case, the 3×BPF acoustic power level is less than 90 dB and not visible in the plot. The power level increases are significantly larger at the sideline condition (e.g., ~3.5 dB at 1×BPF) than for the approach condition (e.g., ~0.5 dB at 1×BPF). Comparing the power level increases for the various inlet configurations makes it clear that the increase is primarily caused by the inflow distortion through the open auxiliary doors but is otherwise essentially insensitive to the details of the inlet hardware. Furthermore, it is clear that the AoA has a negligible effect on the tone power levels.

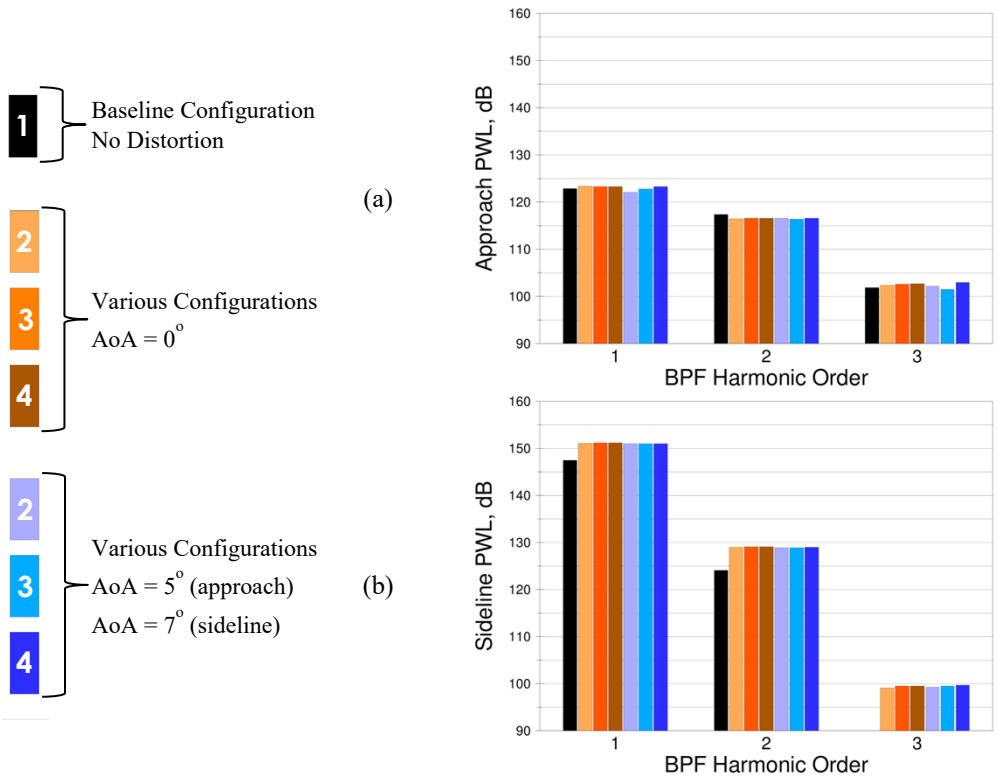
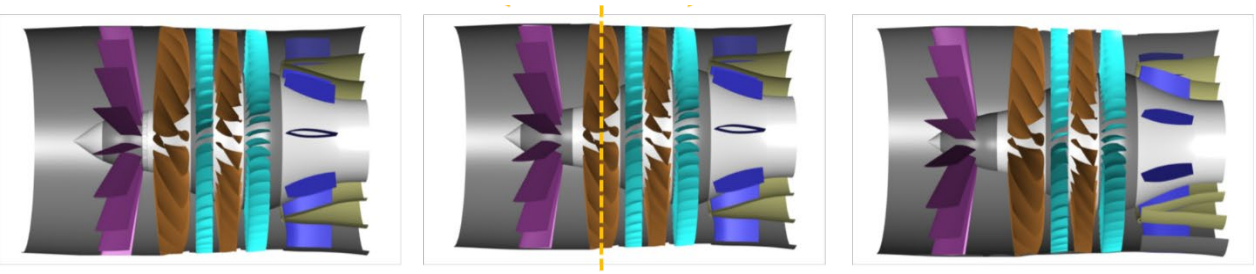


Figure 36.—Impact of inlet distortion on tone acoustic power levels for various inlet configurations shown in Figure 35. (a) Approach operating condition. (b) Sideline operating condition.

4.3.2 Assessment of IGV-Rotor Spacing on Tone Sources

Two of the biggest differences between conventional subsonic propulsors and multistage fans appropriate for supersonic aircraft are the presence of inlet guide vanes (IGVs) and multiple fan stages. The presence of IGVs mostly means that the initial stage will be stationary and will have less blockage to spiraling acoustic modes than a wide-chord fan stage. Multiple stages dictates that rotor-stator spacing will be much smaller in supersonic engines, generally increasing the strength of the rotor-stator interaction, and possibly making potential field interactions acoustically significant. More on the impact of potential fields versus wakes is found in Reference 56.

To explore how rotor-stator interactions might impact the tones produced by small spacings, the SuperFan geometry was altered to move the IGV forward and aft of its designed position by ±26 percent. The geometric variations are shown in Figure 37, with the IGV-R1 spacing quantified by s*, the tip spacing normalized by IGV tip chord. The geometry was first analyzed for thrust performance as significant aero impacts would have invalidated the comparison. The mass flows and thrust performance of all three variations were within less than 1 percent different; therefore, the acoustic results represent viable design alternatives. The acoustic tone power of the IGV-R1 interaction mostly varied inversely with distance. However, some harmonics at some flight conditions were actually increased by increasing the IGV-R1 distance. Exploration of the flow field showed that these were due to phasing of the IGV wakes on the rotor, with some wakes striking the rotor more uniformly along the blade span, increasing the acoustic efficiency of the source. The three-dimensionality of the twisted flow kept the acoustic impact of the IGV-R1 spacing from being monotonic. More details on these nuanced results can be found in Reference 68 and the resulting modeling is described in Section 4.4.



(a) s*=0.936 (b) s*=1.277 (c) s*=1.613

Figure 37.—SuperFan spacing configurations used for IGV-R1 spacing study.

4.3.3 Propagation of Tones from Downstream Stages to Inlet

The question of whether tones generated at downstream stages were significant in the inlet arc of the engine was explored by applying nonlinear-harmonic analysis for perturbations beyond adjacent blade rows and analyzing the perturbation field for frequencies associated with the stages downstream of the immediate one. Prior work (Ref. 69) on two-stage fan noise suggests that the first stage is the main contributor to inlet noise. The present work confirmed this suggestion and identified the IGV-R1 interaction as the primary contribution to inlet noise. In the far-field spectra, negligible power was found in frequency bands created by the blade counts and rpm of the R1-S1, S1-R2, and R2-S2 interactions. The sound generated by these downstream stages is partially blocked by the first fan, which has a particularly high solidity in the present design. This finding promotes the idea that the total fan pressure rise might be distributed to be higher on the second stage, where it is blocked, and so achieve noise reduction for the fan inlet tone.

4.3.4 Assessment of Acoustic Liner Placement

The supersonic inlet designed by GE is quite long compared to current subsonic inlets. Modern subsonic inlets have length-to-diameter (L/D) ratios of around 0.3 to 0.5, while this axial spike inlet has an L/D of ~1 between the IGVs and the downstream edge of the auxiliary inlet. This provides ample area for noise attenuating liners that can help reduce the inlet radiated fan noise. Using the liner methods described previously and demonstrated on the NASA ADP fan liner test, the liner design from GE was evaluated in COMSOL and implemented in Actran for simulation, as shown in Figure 38. The shaded blue area is the lined section and it is shaded to indicate that the liner length was varied during the study.

Because the full treated area prescribed by GE was quite large compared to modern subsonic designs, a study was conducted investigating the effect of liner length. This turned out to be a rather complicated question, given that the fan tone source is changing between operating conditions. Results for the three noise certification conditions are shown in Figure 39.

The effect is quite nonlinear, although generally the longer liner is more effective. The liner is most effective at approach condition, which was likely the design intent from GE. At cutback condition, the noise source is dominated by the m = –14 mode, as discussed in Reference 58. This means that even a short liner will be quite effective, while at approach and cutback the m = 3 mode is important and so additional liner length is helpful. These results informed the fan noise model as presented in Figure 47 and associated text.

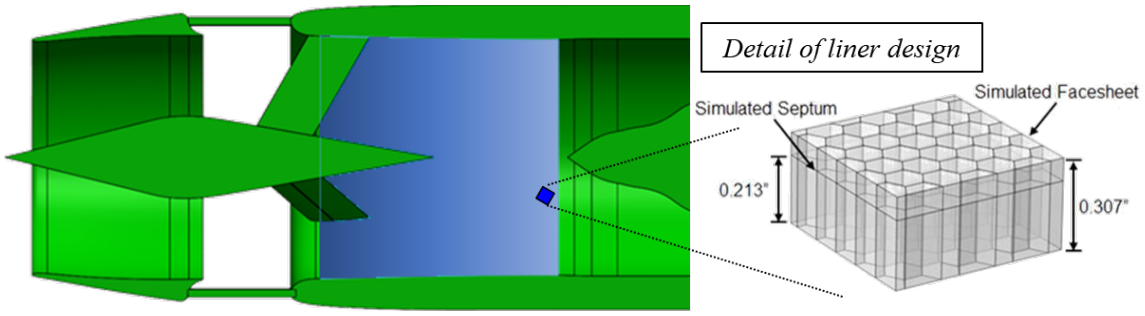


Figure 38.—Acoustic liner for supersonic inlet shown in blue.

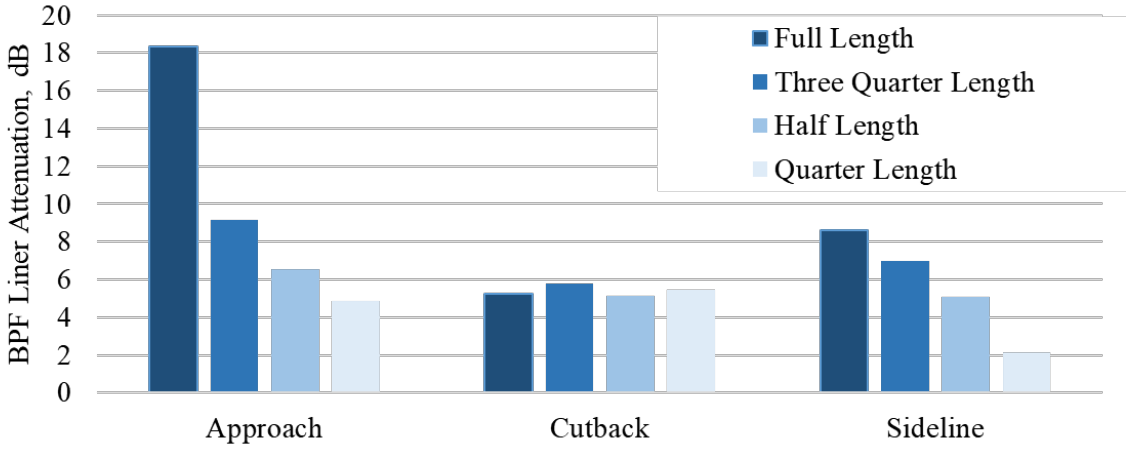


Figure 39.—Effect of liner length for supersonic engine inlet.

4.3.5 Assessment of Axisymmetric Propagation from Source to Far Field

A study was conducted to isolate the effect of inlet topology on the noise radiation to the far field (Ref. 70). In this study, axisymmetric versions of a subsonic and a supersonic inlet were compared, as shown in Figure 40.

The idea of this study was to use the same boundary conditions for the acoustic and flow simulation and compare the resulting far-field noise. This study predates the delivery of the GE fan system to NASA, so the fan noise source was conceptual, and intended to be generic. The forward flight speed was varied and flow calculations were conducted for both geometries. The workflow described previously was used to propagate the sound from the fan face to the far field. A typical result is shown in Figure 41.

It is apparent from this example that the overall trends are similar between the two inlets, with peak noise at a similar geometric angle and the noise falloff at sideline angles similar overall, although there are more ripples in the directivity from the supersonic inlet (red). This is principally because the supersonic inlet acts like a two-port system and causes constructive and destructive interference in the wave pattern. The sound propagation modeled here is linear so there is no mechanism for changing sound power due to inlet geometry. Overall, the study concluded that inlet geometry alone had a weak effect on the radiated noise and the effect of the inlet geometry on the fan noise is likely more important.

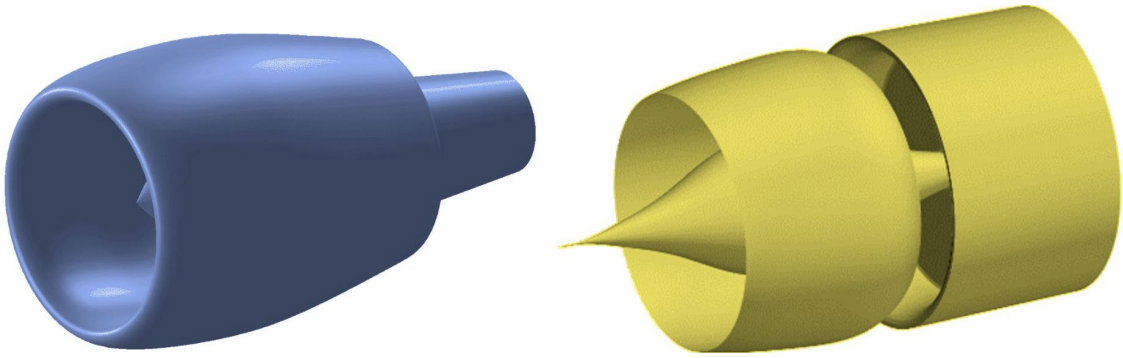


Figure 40.—Axisymmetric subsonic and supersonic inlets used for inlet effect study.

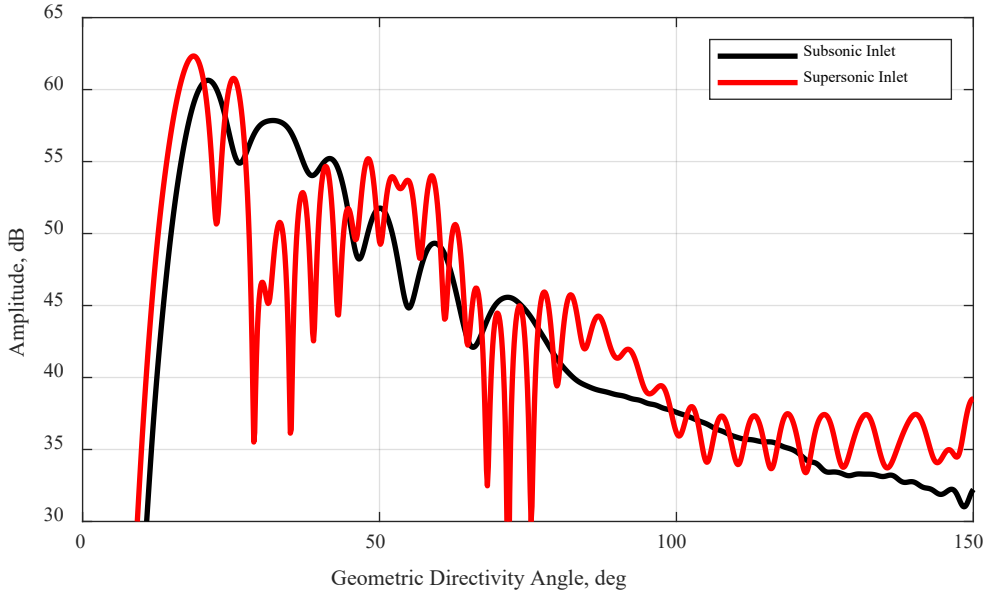


Figure 41.—Example directivity of subsonic and supersonic inlet with same boundary conditions.

4.3.6 Assessment of Azimuthal Features on Propagation of Tones to Far Field

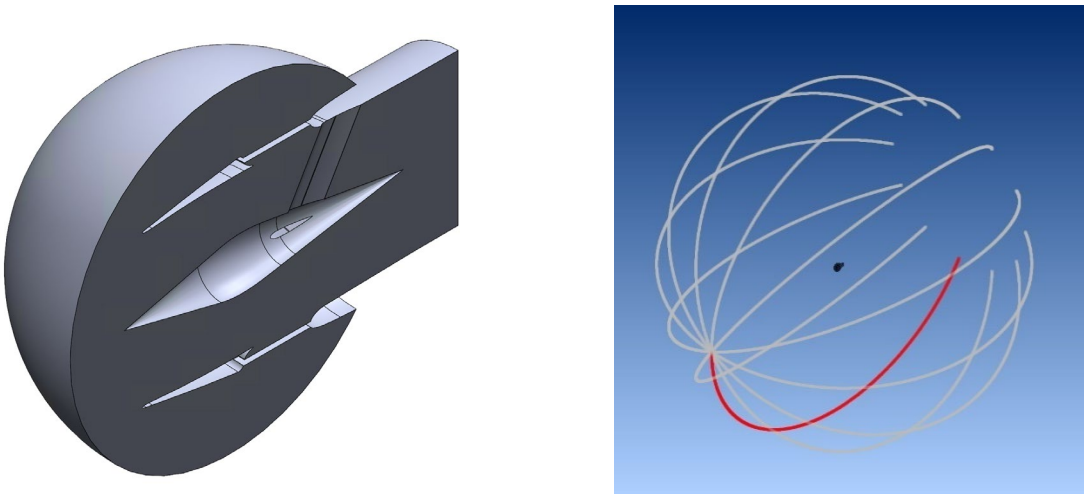
All of the noise propagation work presented previously used a 2D method, where the convected wave equation is expressed in an axiperiodic form. This is computationally extremely beneficial because it allows sufficiently large near-field domains while the finite element mesh size can be fine enough to capture all relevant frequencies with computational times of minutes or hours. The periodicity is needed to capture the spinning modes generated by the turbomachinery, differentiating the solution method from a purely axisymmetric result. This solution method is commonly used for subsonic fan noise, especially for inlets that are nearly axisymmetric. It is bundled in the toolkit Actran TM (for turbomachinery) and was used extensively in the TC. However, the supersonic inlet is not purely axisymmetric and includes a few major features that might affect the radiated sound. The centerbody struts and the actuators for the upstream inlet cowl cannot be included in the axisymmetric model, nor can the effect of inflow AoA.

To include the full 3D effects, we used the FUN3D RANS solver to generate a flow field and used a CAD model to generate a geometry of the fluid domain for meshing in Actran. The Actran ICFD tool is

used to interpolate from the CFD mesh to the acoustic mesh. The far-field sound is now captured on a set of arcs around the finite element domain. Both near-field and far-field geometries are shown in Figure 42.

The workflow, challenges, and findings from this study are described in Reference 69. The 3D geometry was determined to be somewhat ambitious for the computational resources available, with a small geometry required and solution times on the order of 7 h per condition. A total of six cases were run, with three variations on geometry combined with two operating conditions (approach and lateral). The geometry was varied in increasing complexity from axisymmetric to nonaxisymmetric and then at AoA, as shown in Table 3. Example results of the radiated sound are shown in Figure 43. The directivity plots all were somewhat messy and required some interpretation. It can be seen that the major features match, so the differences will come down to quantifying details.

Reference 69 contains more details and discussion, but the overall findings were that the AoA was the smallest effect and the viscous flow field was the largest effect on the propagation of sound out through the supersonic inlet. Being on the order of 1 dB, the 3D effects can certainly be neglected to give first-order results, but for a final noise prediction, it is likely worthwhile to investigate whether they are important.

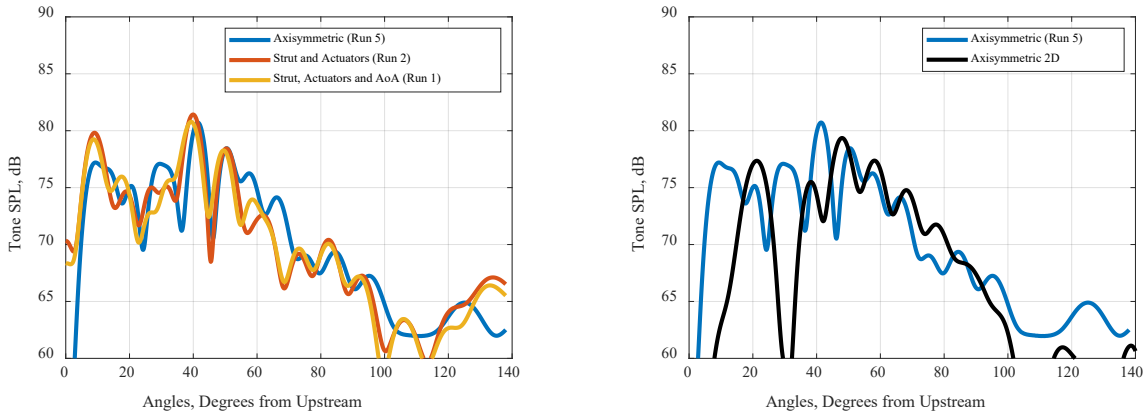


(a) (b)

Figure 42.—Acoustic finite element domain for symmetric-antisymmetric solution method. (a) CAD model. (b) Far-field points around infinite element domain, bottom arc highlighted.

TABLE 3.—CASES STUDIED IN 3D FAN NOISE SIMULATIONS

Run no.	Condition	AoA, degrees	Mach number	Struts and Actuators
5	Approach	0.0	0.261	No
2	Approach	0.0	0.261	Yes
1	Approach	5.2	0.261	Yes
6	Lateral	0.0	0.350	No
4	Lateral	0.0	0.350	Yes
3	Lateral	6.7	0.350	Yes



(a) (b)

Figure 43.—Approach condition. (a) Average directivity over all azimuthal angles comparing 3D effects. (b) Comparison of 3D simulation with RANS flow field versus 2D simulation with potential flow.

4.4 Extensions to Heidmann Fan Model

NASA's ANOPP software contains four empirical fan noise models based on the framework provided by Heidmann (Ref. 71). The models predict five sources: Inlet blade-passing and multiple pure tones, inlet broadband noise, aft blade-passing tones, and aft broadband noise. In the benchmark STCA assessment (described in Section 2.2), the fan inlet noise was modeled following the recommendation of (Ref. 66). The inlet broadband noise was modeled using the GE Large Fan Model; the inlet tone noise was modeled using the AlliedSignal Small Fan Model (Ref. 72). All four Heidmann fan (HDNFAN) empirical models were developed for subsonic single-stage fans of various sizes, but none were based on data relevant to high-speed two-stage fans, which may be used by commercial supersonic aircraft being developed by industry. In an effort to capture the noise from these two-stage fans, a fifth Heidmann fan empirical model was developed and is referred to as the HDNFAN-2S model. This model was developed using the same empirical model format as the other four Heidmann fan models, but it was created using the high-speed two-stage fan experimental data from the 2002 QSP test (described in Section 2.1). The accuracy of the models were evaluated by taking the difference in SPL spectra over all polar angles measured and computing the mean, E, and standard deviation, S, of the difference for all 11 rpm speeds and seven configurations measured in the QSP test. The resulting HDNFAN-2S model resulted in a reduced error when compared to the other Heidmann models. In Figure 44, the magnitude of the error offset E (left) and standard deviation of the error S (right) are shown for HDNFAN methods 1 to 4 and the newly developed HDNFAN-2S method.

After utilizing the HDNFAN-2S model to predict the QSP experimental data points, it was observed that multiple data points were overpredicted. This was due to the variations in the QSP fan configurations tested; multiple configurations contained IGV-R1 spacer acoustic treatment and had a larger spacing between the rotor stages, as shown in Table 4. A cross section of the QSP fan configurations for the baseline and the low noise configurations can be seen in Figure 45, with the acoustic treatment highlighted in the yellow box.

It was therefore determined that the new HDNFAN-2S model needed to incorporate the effect of acoustic treatment. To accomplish this, a study comparing the application of the acoustic treatment models in ANOPP to the HDNFAN-2S model was conducted. ANOPP has two methods for predicting the acoustic attenuation of fan noise by liners: the Magliozzi method (Ref. 73), and the GE method (Ref. 23). Both methods were coded into the HDNFAN-2S MATLAB® model (The MathWorks, Inc.) and the

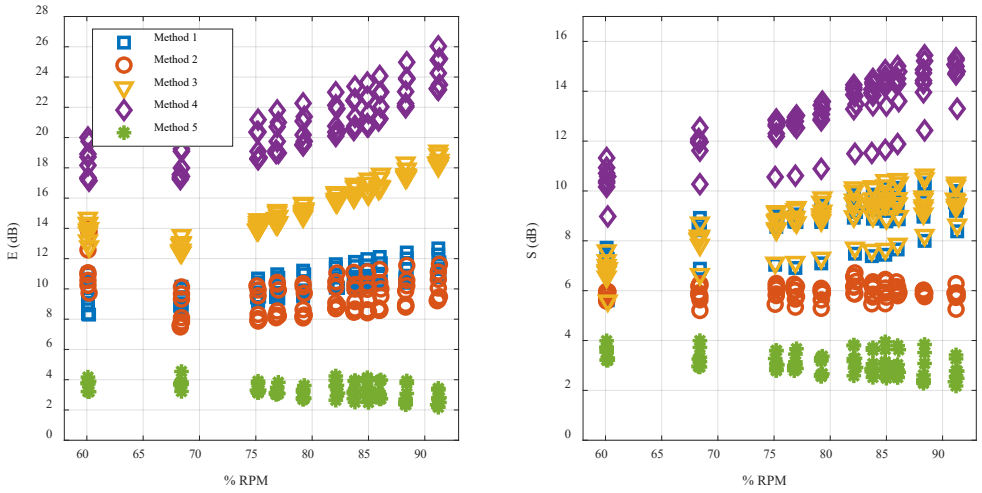


Figure 44.—Comparison of offset and standard deviation of HDNFAN methods, including new HDNFAN-2S method, in predicting QSP data set.

TABLE 4.—QSP EXPERIMENTAL FAN CONFIGURATIONS

Configuration no.	IGV count	IGV-R1 spacing	IGV-R1 spacer treatment	R1-S1 spacing	S1 angle, (°)	Acoustic barrier wall
1A	23	Nominal	N/A	Nominal	4.1	Original
2	23	Open	Hard Wall	Nominal	4.1	Original
3	23	Open	Treated	Nominal	4.1	Original
4	19	Open	Treated	Nominal	4.1	Original
5	19	Open	Hard Wall	Nominal	4.1	Original
9A	19	Open	Treated	Open	4.1	Extended
9S	19	Open	Treated	Open	–3.0	Extended
11W	23	Nominal	N/A	Open	4.1	Extended

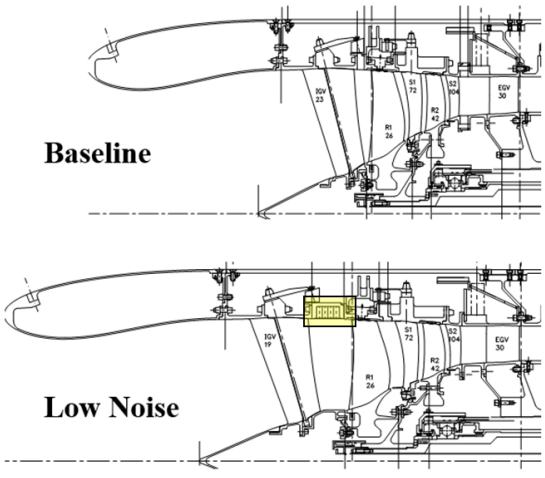


Figure 45.—Cross sections of QSP fan baseline and low noise configurations.

impact of the IGV-R1 spacer treatment was calculated and applied to the appropriate QSP configurations. A comparison of the impact on standard deviation of the fan inlet noise showed that the Magliozzi method increased the standard deviation by 0.4 EPNdB and the GE method reduced the standard deviation by 0.3 EPNdB. The GE method was adopted into the HDNFAN-2S model and was carried forward in the system assessments as the preferred treatment method. The inlet treatment suppression curve for the GE model is shown in Figure 46.

A secondary study was performed to validate the correct implementation of the acoustic treatment model in the HDNFAN-2S. This was done through comparing the impact of various liner lengths and positioning (in the forward inlet of the IGV versus in between the IGV and the R1 rotor) based on calculations from the GE method (modeled in HDNFAN-2S) and Actran. The comparison was done for the SuperFan inlet/fan model, and the results can be seen in Figure 47. The TREAT GE model (an ANOPP liner model) seemed to underpredict the attenuation at approach condition, perform similarly at the flyover condition, and overpredict at the lateral (sideline) condition when compared to the Actran

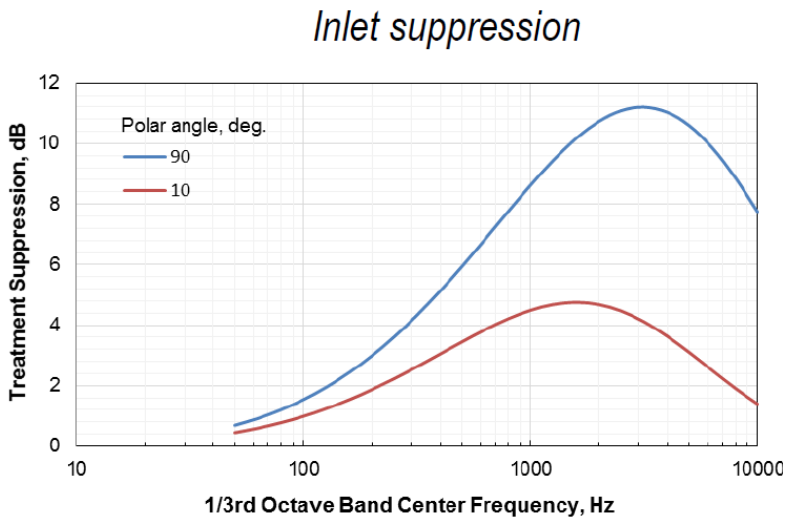


Figure 46.—GE treatment empirical method in HDNFAN-2S model.

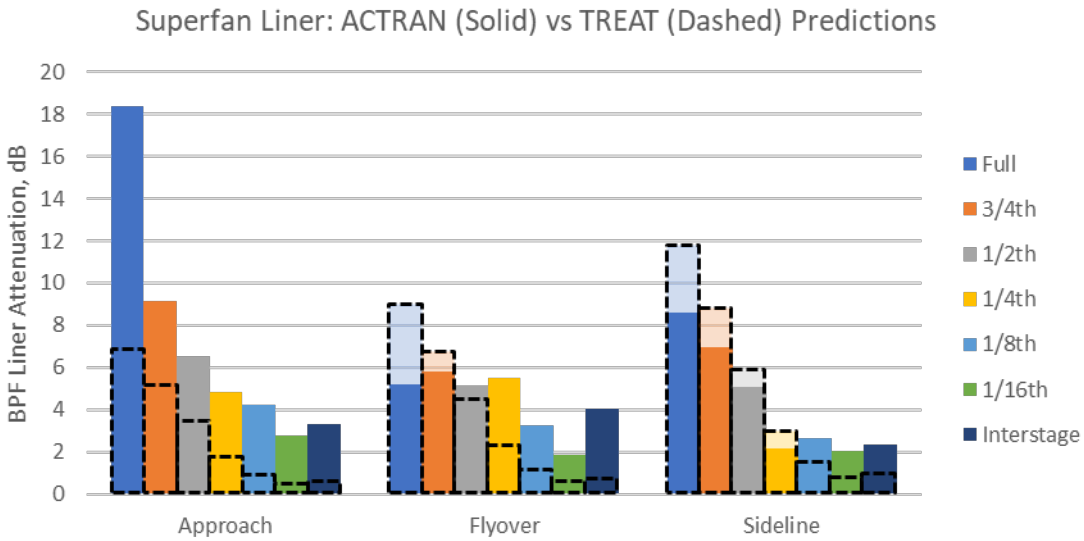


Figure 47.—Comparison of Actran-calculated liner attenuation versus TREAT (GE) model calculations for SuperFan.

results. The decision was made to continue using the GE TREAT model in HDNFAN-2S model without any alterations based on the Actran results given that it captures the trend with liner length adequately and would be a more conservative approach to handling the impact of acoustic treatment.

The other crucial two-stage fan variation investigated that needed to be captured in the empirical fan model was the impact of the IGV to R1 spacing. To save weight in the engine system for supersonic aircraft, fan designers might be tempted to minimize the space between the IGV and R1 rotor. However, this could potentially cause an acoustical problem to arise as the strength of the fan harmonic tones generally increase as the spacing between the IGV and R1 is reduced. The QSP data set contained two different IGV to R1 spacings (see Figure 45) and the HDNFAN-2S model was lacking a method to capture the acoustic impacts of the different spacings. Therefore, the goal was to provide a high-level impact of reducing spacing and capture an appropriate noise penalty for having tight IGV to R1 spacing in a two-stage fan.

The IGV to R1 spacing model was developed from Fidelity Fine Turbo simulations of three different IGV to R1 spacings of the SuperFan model (refer to Section 4.3). The IGV to R1 spacing parameter (s*) was defined as the IGV to R1 spacing normalized by the axial tip chord length of the IGV. The three different spacing configurations were run through a Fidelity Fine Turbo analysis and the results were used to create the empirical IGV to R1 spacing model for HDNFAN-2S. The three configurations and associated IGV to R1 spacing values are shown in Figure 37.

These three configurations were run at four different power/rpm settings corresponding to approach (63 percent power), flyover (80 percent power), lateral (93 percent power), and takeoff (100 percent power) conditions. The results generated sound power levels for the first three harmonics of the R1 rotor as functions of axial distance from the centerline of the R1 rotor. These results were computed for each combination of spacing/power setting, resulting in 12 trendlines for each harmonic (1×BPF, 2×BPF, and 3×BPF). An example showing the results for the 1×BPF at the flyover condition is shown in Figure 48. The circled data points in the figure represent the values used for the creation of the empirical model in HDNFAN-2S. It was determined that the point prior to a drop-off in sound power level should be used for the model because the empirical model would not have the capability of determining the effect of evanescent modal content in the fan acoustic signature, and this drop-off represents the point at which evanescent acoustic waves start to diminish. It should be noted that there were some combinations of

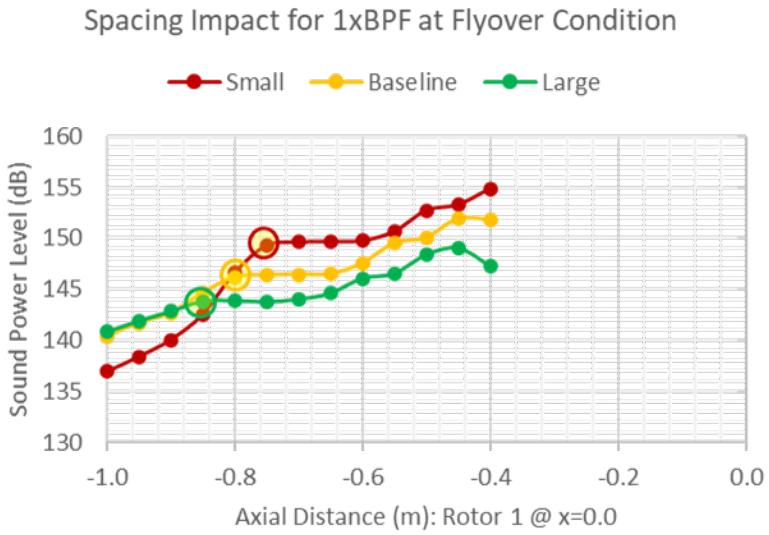


Figure 48.—1xBPF sound power level results for three IGV-R1 spacing values at flyover condition.

spacing/power condition that exhibited unexpected trends, most likely due to nonoptimal phasing of the wakes off the IGV into R1.These points were excluded from the empirical model given that the goal of this effort was to capture high-level trends appropriate for use during the conceptual design phase. Investigating these unusual points could be part of future work to enhance the current model further.

The empirical IGV to R1 model developed for HDNFAN-2S consists of nine different curves based on logarithmic functions of the form $\Delta PWL = A \times \ln(s^*) - B$, where s* is the normalized IGV to R1 spacing, and A and B are coefficients determined empirically from the simulation data. A separate equation was created for each power setting/harmonic value, and all nine are shown in Figure 49, and the A and B coefficient values are shown in Table 5. The approach condition (A) curves are shown in orange, the flyover condition (F) curves are shown in green, and the lateral/takeoff condition (T) curves are shown in blue. The appropriate range of IGV to R1 spacing values for use with these models is s*=0.2 to s*=3.0 and should not be used outside of this range. These empirical models were implemented into the HDNFAN-2S code and used for the final system uncertainty assessments.

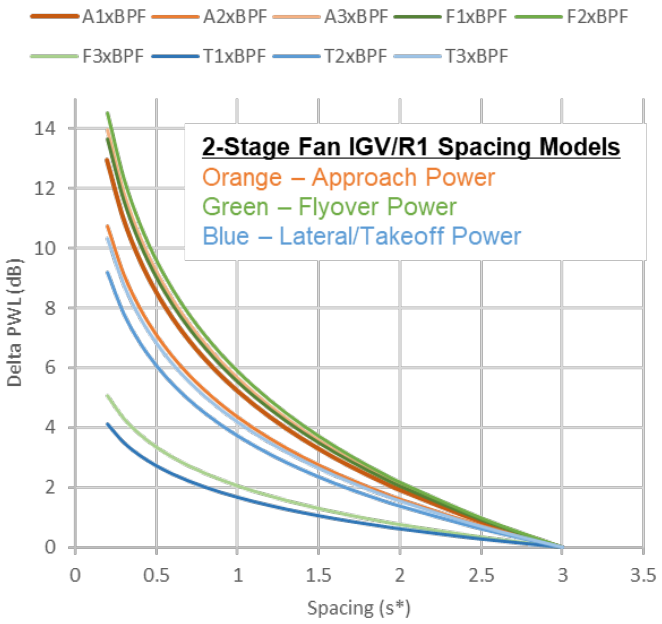


Figure 49.—Two-stage fan IGV to R1 spacing models implemented into HDNFAN-2S.

TABLE 5.—TWO-STAGE FAN IGV TO R1 SPACING MODEL EMPIRICAL COEFFICIENTS

Power condition	Fan tone harmonic	A	B
Approach	1×BPF	–9.588	10.500
	2×BPF	–7.938	8.720
	3×BPF+	–10.320	11.340
Flyover	1×BPF	–10.090	11.080
	2×BPF	–10.720	11.777
	3×BPF+	–3.733	4.101
Lateral/Takeoff	1×BPF	–3.057	3.358
	2×BPF	–6.784	7.453
	3×BPF+	–7.624	8.376

5.0 Jet Noise Model Development—Simulation and Modeling

5.1 Simulation Tool Description

The simulation of jet noise presents significant challenges due to the complex interactions between turbulent flows and acoustic fields. The Launch Ascent and Vehicle Aerodynamics (LAVA) solver, an advanced multiscale, time-accurate flow simulation package, was developed at NASA Ames Research Center (ARC) (Ref. 74) to leverage state-of-the-art computational techniques for problems such as jet noise. The current capabilities of LAVA are illustrated in Figure 50, which highlights its comprehensive integration and extensive functionality.

The LAVA solver framework offers flexible meshing options and was developed with the intent of modeling highly complex geometries and flow fields. For a majority of the work presented in this report, the compressible Navier-Stokes equations are solved using a finite-difference formulation applied to the curvilinear transformed system of equations in strong conservation law form using a third-order Runge–Kutta Total Variation Diminishing (RK3-TVD) time integration scheme (Ref. 75). LAVA includes detached eddy simulation (DES) and wall-modeled large eddy simulation (WMLES) capabilities. These models are crucial for accurately capturing the complex turbulent flows that contribute to jet noise.

Section 5.2 describes how LAVA has been applied to the prediction of jet noise within the NASA CST project since 2016. A historic overview of how the solver was validated on canonical cases, including round jets, chevron nozzles, and jet surface interaction noise, is followed by exposition of improvements that enabled generation of a large database to assess uncertainties of physics-based simulation technologies. Section 5.3 focuses on the prediction of jet noise applied to single-stream round jets in static as well as in-flight conditions. Finally, Section 5.4. describes how the developed best practices were applied to supersonic two-stream nozzle configurations with internal mixing and internal/external plugs representative of supersonic aircraft.

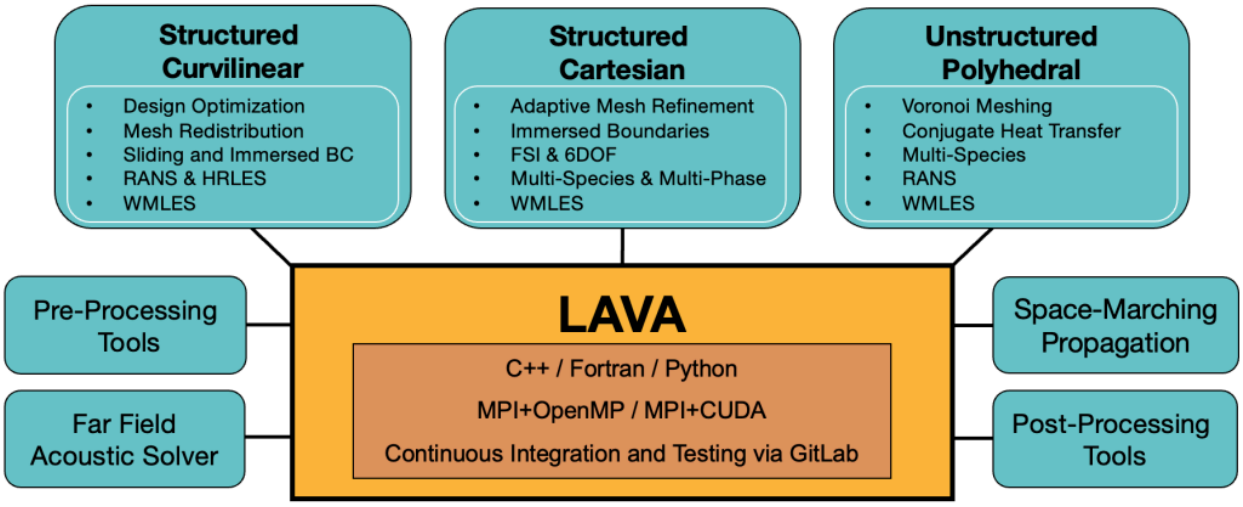


Figure 50.—Flow chart depicting Launch Ascent and Vehicle Aerodynamics (LAVA) solver capabilities.

5.2 Validation Exercises for Jet Noise Tools

The present LES development effort started in 2016 as part of the NASA Transformative Technology and Tools Program's Revolutionary Computational Aerosciences (RCA) challenge, focusing on validation and verification exercises aimed at improving jet CFD predictions. Our objective was to enhance the prediction of key metrics for jet simulations, including potential core length and turbulent kinetic energy (TKE) quantities along the lipline and centerline. By applying hybrid RANS-LES (HRLES) methods, specifically delayed detached eddy simulation (DDES) and zonal detached eddy simulation (ZDES), we achieved significant improvements. Our predictions of potential core length surpassed state-of-the-art RANS applications by more than 90 percent, with findings detailed in a report by Housman et al. (Ref. 76). Figure 51 illustrates the improvements in predicting potential core breakdown. Additionally, we performed far-field noise predictions using a Ffowcs Williams–Hawkings (FWH) propagation approach. Although our results showed good agreement in jet noise predictions, we identified discrepancies at high frequencies, attributed to delays in turbulence transition within the jet shear layer and boundary layer. This delayed transition of turbulent structures in the jet shear layer is depicted in Figure 51, comparing an early DDES simulation with a ZDES simulation. To address these deficiencies in high-frequency noise prediction, we continued our study by investigating the effects of boundary layer tripping and exploring several different FWH surface strategies, as detailed in Stich et al. (Ref. 77). By incorporating boundary layer tripping, we aimed to accelerate the transition to turbulence, thereby improving the accuracy of high-frequency noise predictions. Additionally, we experimented with different FWH surface configurations to better capture the noise generated by the turbulent structures. These efforts led to improved agreement between our simulations and experimental data, particularly in the high-frequency range. The use of permeable FWH surfaces enclosing both the jet and surrounding structures proved effective in predicting far-field noise, further enhancing the fidelity of our simulations.

Once best practices for jet noise prediction were developed on an axisymmetric round jet, more complicated geometries typically seen in supersonic configurations were addressed. One topic chosen was jet surface interaction noise. A plate was placed in close proximity to the jet and aimed to establish if we could accurately capture the complex physical interactions between the flow features and differentiate

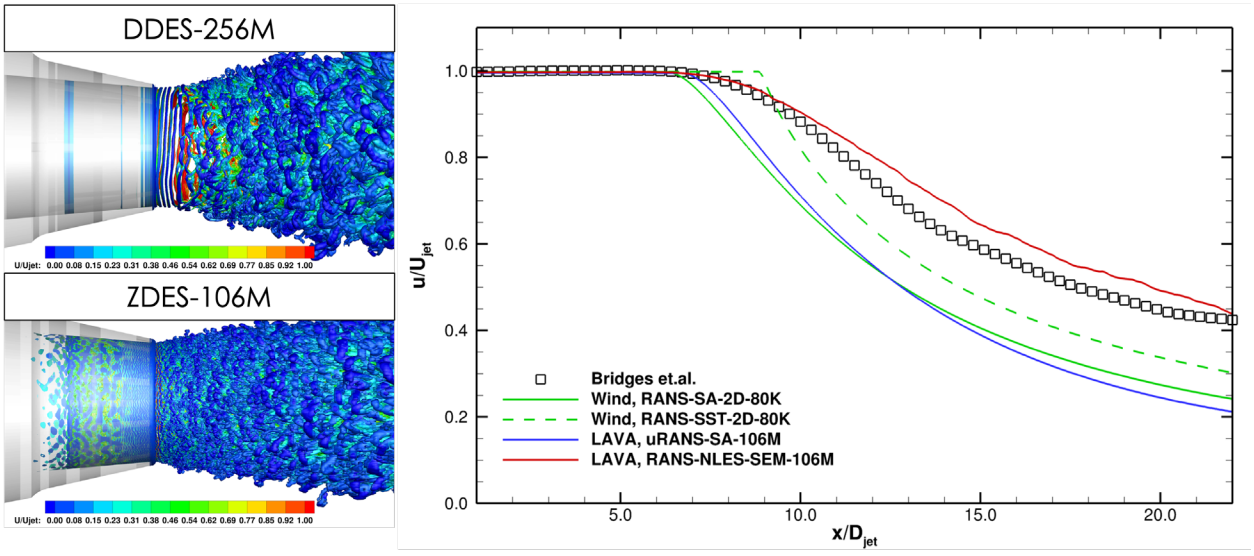


Figure 51.—Iso-surface of Q-Criterion colored by streamwise normalized velocity for DDES (top left) and ZDES (bottom left). Comparison of centerline normalized streamwise velocity between RANS simulations and hybrid-RANS LES within LAVA from study performed in 2017.

the noise between the shielded and reflected sides. This investigation was also part of the 2019 study by Stich et al. (Ref. 77). By simulating the noise generated by a high-speed turbulent round jet near a simple planar surface, we made detailed comparisons with experiments conducted at NASA Glenn. The study demonstrated our ability to predict the shielding effect of the plate at low-to-mid frequencies, although further improvements in mesh resolution are needed for high-frequency noise predictions. These findings are crucial for understanding jet-surface interactions and improving noise prediction models for more complex supersonic configurations.

Figure 52 shows passive particles seeded inside the nozzle, which are convected downstream and interact with the plate. The centerline slice, displayed in red and blue, illustrates the pressure gradient over time, highlighting acoustic contributions. Clear features such as noise reflection at the plate, shielding effects between the shielded and reflected sides, noise generated at the plate trailing edge, and noise escaping from the backside of the plate are evident.

Up to this point, we were using hybrid RANS-LES methodologies, which require a y+ less than 1 resolution in the near-wall region, resulting in highly skewed cells that demand a more permissive numerical treatment, such as increased artificial dissipation for stability. Another downside of using HRLES is the necessity of implicit time-marching methods, which, although allowing larger time steps, are computationally expensive and somewhat negate the benefits when small time steps are required for acoustic predictions. To overcome these limitations, we developed a wall-modeled LES (WMLES) approach within our LAVA solver. We applied it first to a simple round jet previously studied and then to a complex chevron nozzle configuration. Findings of this are reported in Stich et al. (Ref. 78). We not only demonstrated improvements in accurate jet noise predictions but also achieved a significant reduction in turnaround times—more than 60 times faster—reducing simulation times from months to hours. The improvement in turnaround times was achieved through the switch to an explicit time-marching scheme for WMLES and a complete refactoring of the LAVA solver for modern computer cluster systems. This allowed us to run simulations much longer with the same computational resources, unlocking improvements in the low-frequency spectrum by almost an order of magnitude, which was previously not feasible with HRLES implicit time-marching. Figure 53 illustrates the resolution range between HRLES and WMLES. By relaxing the near-wall grid requirement from y+ less than one to around 150, we generated more isotropic cells, allowing the use of less dissipative schemes and the resolution of finer turbulent scales. This change enabled the redistribution of mesh points, which were

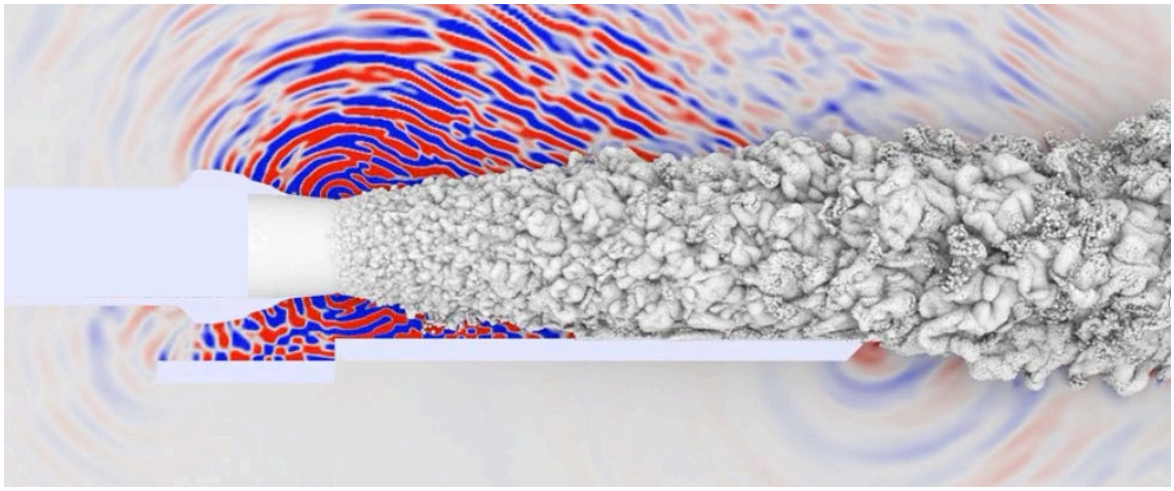


Figure 52.—Passive particles and pressure gradients showing noise reflection, shielding effects, and noise generation at plate's trailing edge.

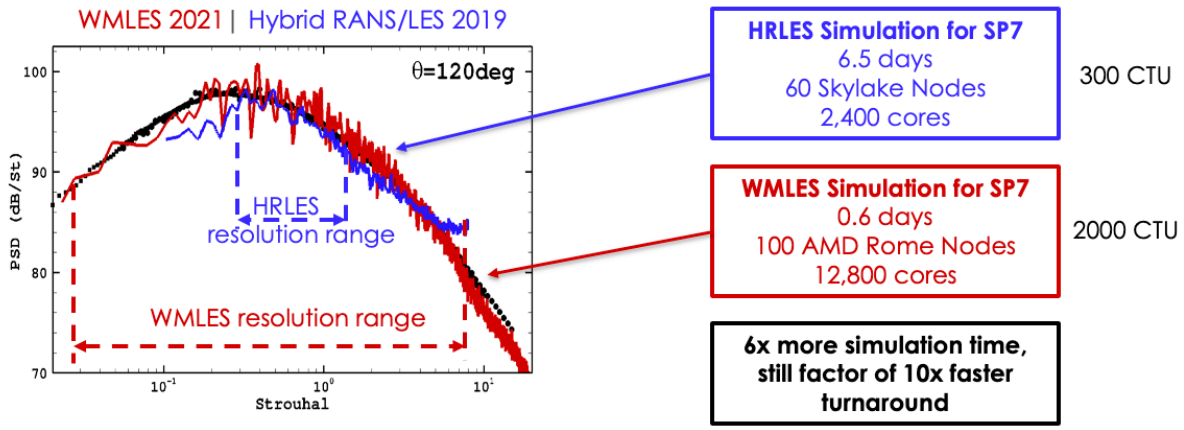


Figure 53.—Comparison of HRLES and WMLES resolution ranges, illustrating relaxation of near-wall grid requirements and resulting improvements in resolving finer turbulent scales with WMLES.

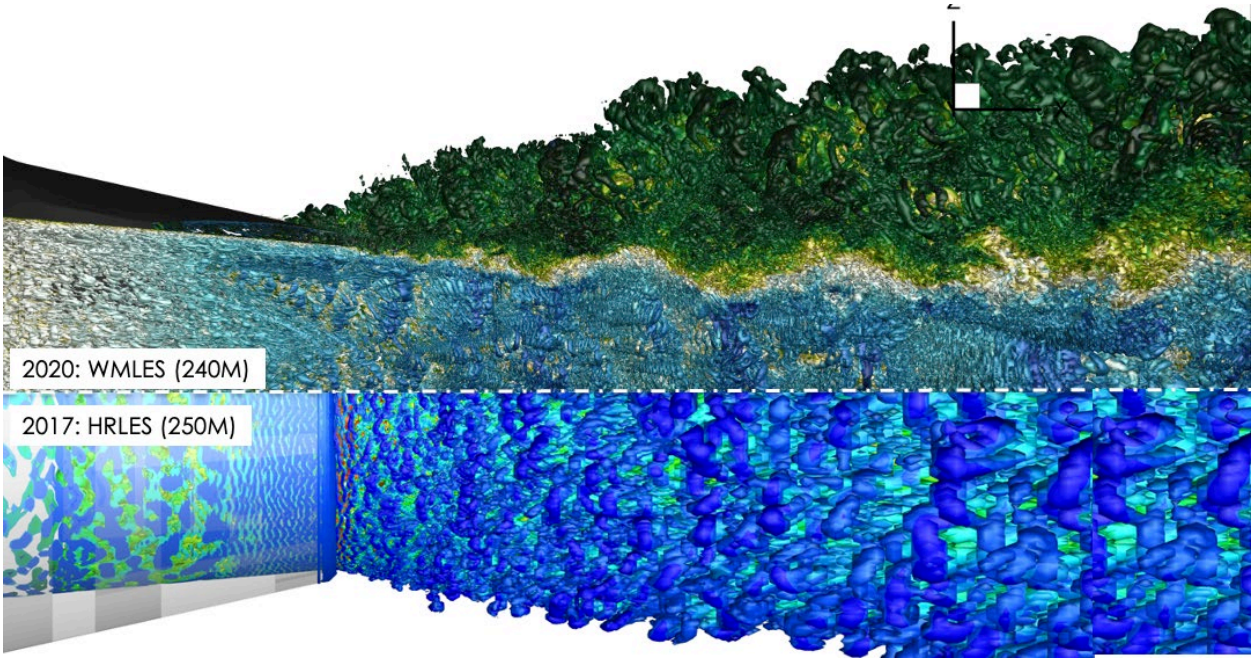


Figure 54.—Iso-contours of Q-criterion for simulations with equal mesh counts, comparing HRLES (bottom) with WMLES (top). WMLES resolves more physical flow structures, demonstrating improved solution accuracy while being computationally cheaper.

previously highly clustered in the near-wall region, across the entire domain, resulting in smaller cell sizes in the main jet flow region. The effect is shown in Figure 54, where the iso-contours of Q-criterion for simulations with equal mesh counts performed with WMLES versus HRLES demonstrate the resolution of more physical flow structures with WMLES.

With all the improvements in numerical methods and the development of WMLES within LAVA, we enabled the generation of a first-of-its-kind LES database for jet noise prediction. Initially applied to round jets in both static (no free stream) and in-flight (coflow) conditions, as described in Section 5.3, this approach was then extended to a supersonic configuration with multistream internal mixers and internal and external plugs, as detailed in Section 5.4.

5.3 Validation on Single-Flow Nozzles

A significant milestone in the PUR TC was the validation of LES of single-flow nozzles under static conditions. In 2022, nine cases were validated using wall-modeled large-eddy simulations (WMLES) performed with the LAVA CFD software. This effort addressed the new PUR Technical Challenge within NASA's CST project, justifying the use of LES to generate noise databases for supersonic propulsion concepts.

In this study, we focused on generating a simulation database for single-stream axisymmetric round nozzles under static conditions (no ambient coflow). We conducted simulations for nine different flow conditions, with jet exit Mach numbers ranging from 0.38 to 1.0 and nozzle temperature ratios (NTR) from 0.84 to 2.7. The different flow conditions, as well as the geometry, can be seen in Figure 55. Details of the structured overset grids, numerical discretization, and wall-model were provided in a publication by Stich et al. (Ref. 79). Near-field comparisons to Particle Image Velocimetry (PIV) data showed excellent agreement for both velocity and normal stresses, although a systematic TKE overshoot at the nozzle exit was observed in the lipline shear layer. A permeable FWH surface, enclosing the jet, was used to predict far-field noise from the simulated flow field. This campaign demonstrated that predicting jet noise with WMLES within the LAVA framework can be performed within a few days' turnaround time, making it a cost-effective approach for jet noise predictions.

Comparison of CFD predictions to microphone array measurements demonstrated excellent agreement within the resolved frequency range, although a systematic underprediction at far-aft observer angles larger than 150° was observed across all simulations. This can be seen in Figure 56, which shows the band-limited Overall Sound Pressure Level (OASPL) for observers from 55° to 165° for the static cases in Figure 55. One reason for the underprediction of noise at far-aft angles is related to the numerical setup of these simulations. Typically, the simulation domain extends up to 60 nozzle diameters downstream and then rapidly coarsens to reduce the mesh count. However, given that the 165° microphone gets extremely close to the growing turbulent structures of the jet, some noise contributions to the downstream angles might not be captured in the LES due to the shortened domain. To account for these structures, the domain would need to be extended to at least 140 nozzle diameters. Although the additional mesh count would increase the simulation costs, the more significant issue is the temporal scale of these downstream structures, which are several orders of magnitude larger than those upstream. These structures convect extremely slowly, requiring the simulation to run for a much longer time—on the order

	Set Point SP	Ma [-]	M_j [-]	M_∞ [-]	NPR [-]	NTR [-]	Exp. Data PIV	Exp. Data MIC
static	3	0.50	0.51	0.0	1.197	0.96	✓	✓
	7	0.90	0.98	0.0	1.852	0.84	✓	✓
	23	0.50	0.38	0.0	1.102	1.76	✓	✓
	27	0.90	0.68	0.0	1.368	1.76	✓	✓
	29	1.33	1.00	0.0	1.898	1.76	✓	✓
	38	1.33	0.88	0.0	1.664	2.27	✗	✓
	46	0.90	0.56	0.0	1.219	2.70	✓	✓
	49	1.48	0.90	0.0	1.697	2.70	✓	✓
	101240	1.14	0.85	0.0	1.608	1.78	✗	✓
In-flight	100084	1.32	1.09	0.3	2.110	1.48	✗	✓
	100024	1.01	0.85	0.3	1.616	1.40	✗	✓
	100274	1.20	0.99	0.3	1.875	1.47	✗	✓
	101244	1.13	0.85	0.3	1.603	1.78	✗	✓

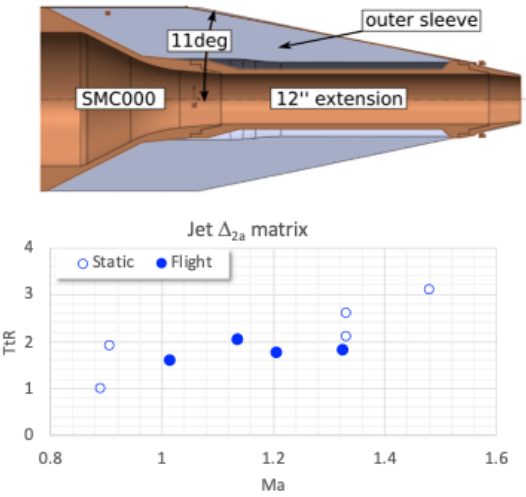
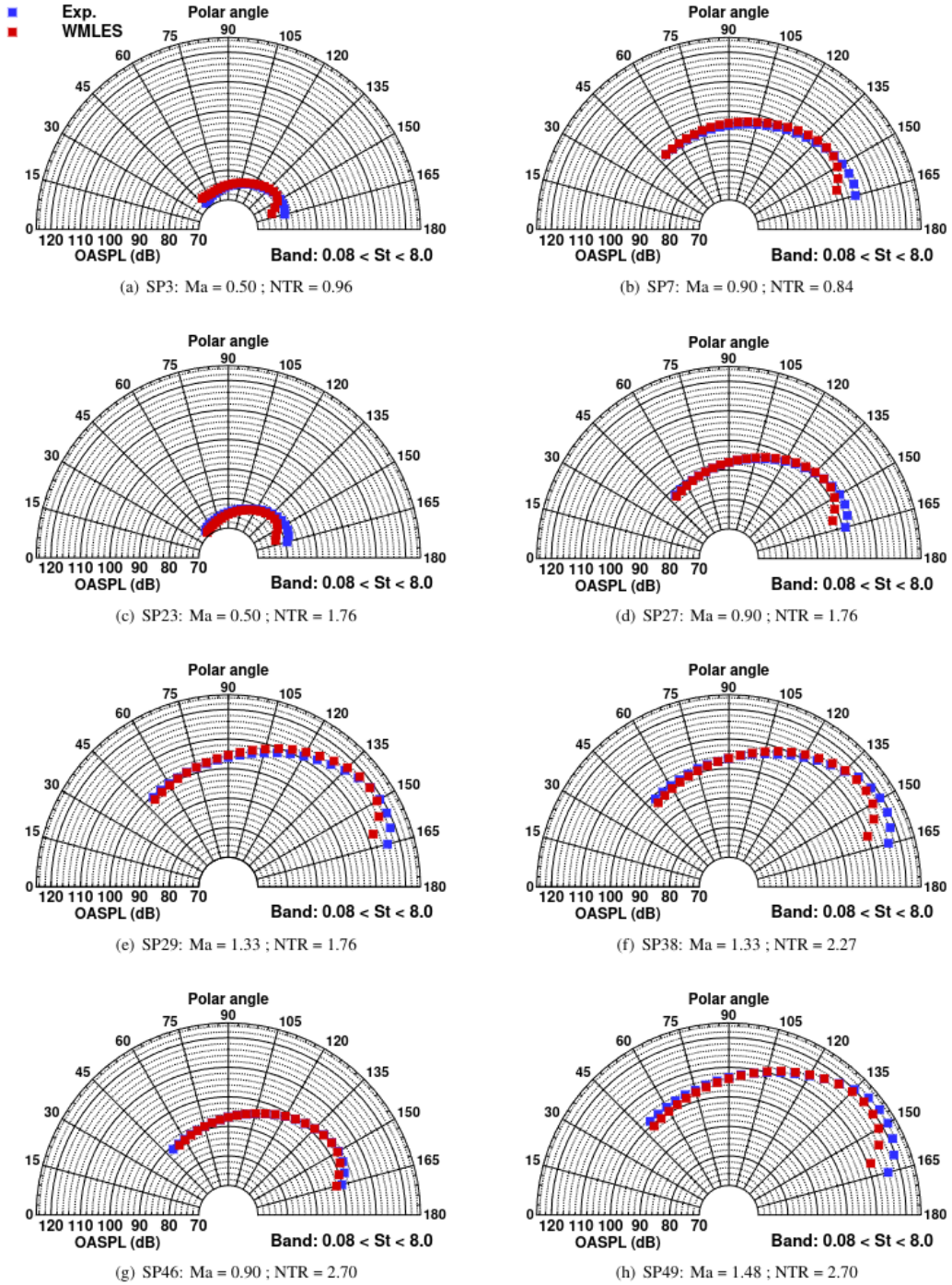


Figure 55.—D2a database flow conditions and geometry used in CFD simulation study.

of 10,000 convective time units based on the jet nozzle diameter and exit velocity—to accurately capture them (Ref. 80). This extended runtime would drastically increase the simulation costs. Given that the difference is only observed at very far-aft angles, the increased cost does not always justify including these effects. However, if capturing these far-aft noise contributions is critical, one must be prepared to bear the additional computational expense.



(a) SP3: Ma = 0.50 ; NTR = 0.96

(b) SP7: Ma = 0.90 ; NTR = 0.84

(c) SP23: Ma = 0.50 ; NTR = 1.76

(d) SP27: Ma = 0.90 ; NTR = 1.76

(e) SP29: Ma = 1.33 ; NTR = 1.76

(f) SP38: Ma = 1.33 ; NTR = 2.27

(g) SP46: Ma = 0.90 ; NTR = 2.70

(h) SP49: Ma = 1.48 ; NTR = 2.70

Figure 56.—Comparison of band-limited (0.05 < St=freq*D_{jet}/U_{jet} < 8) OASPL at 100D_{jet} from nozzle exit obtained from WMLES with FWH propagation. Experimental data by Brown and Bridges (Ref. 81).

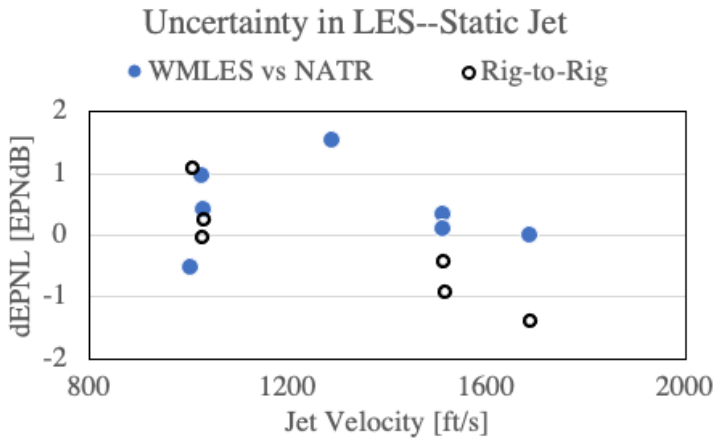
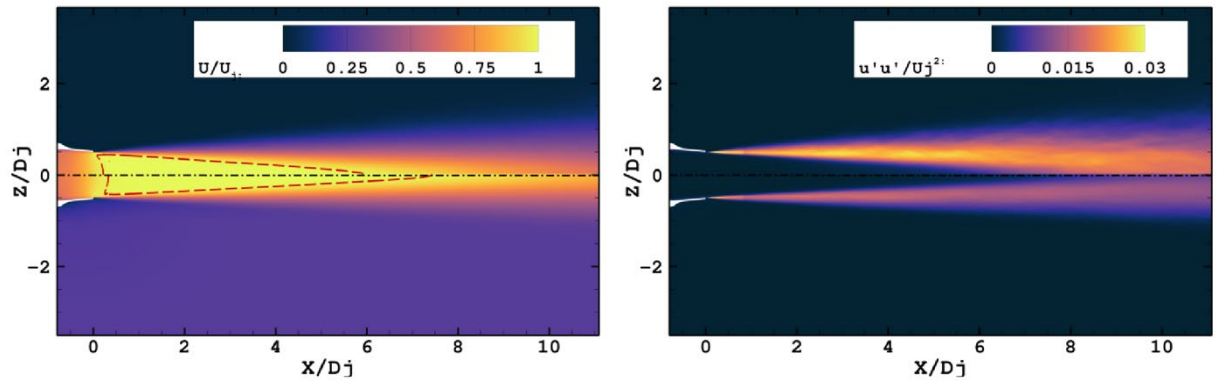


Figure 57.—Discrepancies between experimental rigs (HFJER and SHJAR) and between WMLES and HFJER for validation cases.

The deviations in component EPNL of WMLES and HFJER experimental data are shown in Figure 57 as blue dots. For comparison, the deviation for cases replicated on a small jet rig (SHJAR) in the same facility are also shown in the same plot, indicated by hollow black circles. The standard deviation of the rig-to-rig error is 0.96 EPNdB; for the LES error, it is 0.72 EPNdB. Based on this, the LES was determined to have similar uncertainty as the experimental error of a physical model-scale rig test. It would seem that LES could safely be used in place of physical experiments for jet noise. However, in the following, we will see that this isn't correct yet.

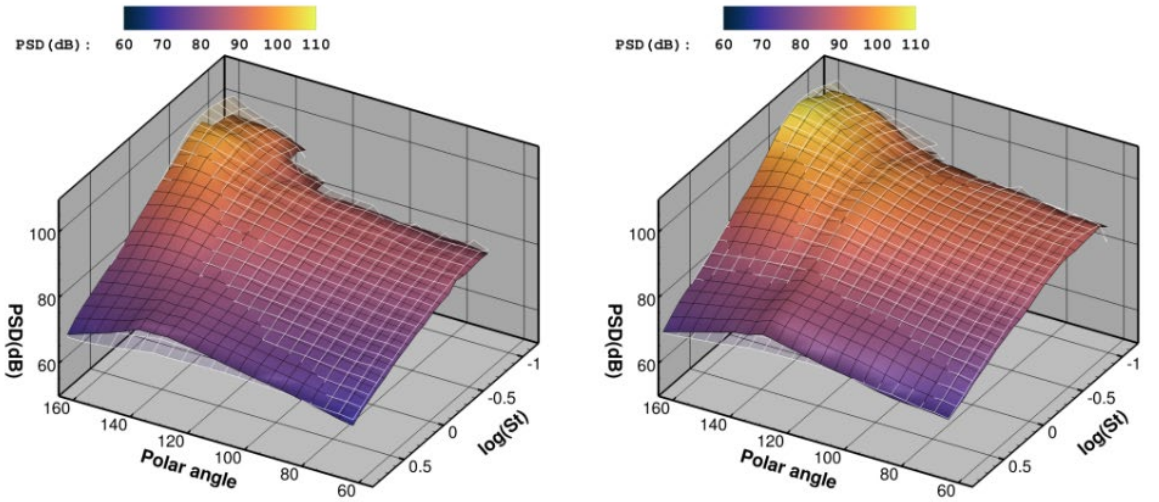
Building upon the validation under static conditions, we progressed towards simulating in-flight conditions to assess the effect of a free stream on the general flow-field and noise characteristics. The effect of the flight stream was assessed on two specific points, SP101240 and SP101244, which have nearly identical flow conditions but different ambient coflows. Both cases have an acoustic Mach number of 1.13, NTR of 1.78, and nozzle pressure ratio (NPR) of 1.608, with SP101244 having an in-flight Mach number of 0.3 and SP101240 having one of 0. This allows for a direct comparison to assess the impact of the flight stream on flow-field quantities, resulting in an overall reduction of noise spectrum levels. The flight stream significantly impacts the near-field flow. The shear layer is stretched axially by the coflow, resulting in a delayed breakdown of the potential core, as highlighted by the red dashed iso-contour with U = 0.98Uj in Figure 58. The reduced shear due to the smaller velocity difference between the coflow and the jet lowers the turbulent intensity along the lipline. The peak TKE along the centerline, caused by the collapse of the potential core, is both delayed and smaller in magnitude when compared to the static jet. This reduction in kinetic energy at the shear layer is a major reason for the decrease in far-field noise with increasing ambient flow.

The introduction of a flight stream impacts far-field noise predictions. Comparison of LES predictions to microphone array measurements, however, showed good agreement within the resolved frequency range (Figure 59). There was a dip in the predicted low-frequency noise spectra for observers between 120° and 145°. This dip is smaller for lower Mach numbers and seems to be correlated to the Mach wave radiation angle. The Mach 1.1 jet (Figure 59(d)) exhibits broadband-shock associated noise (BBSN), but while the onset of BBSN appears to be captured correctly in WMLES, some differences in its magnitude and the prominent frequency at which it occurs persist between the experiment and the simulations.

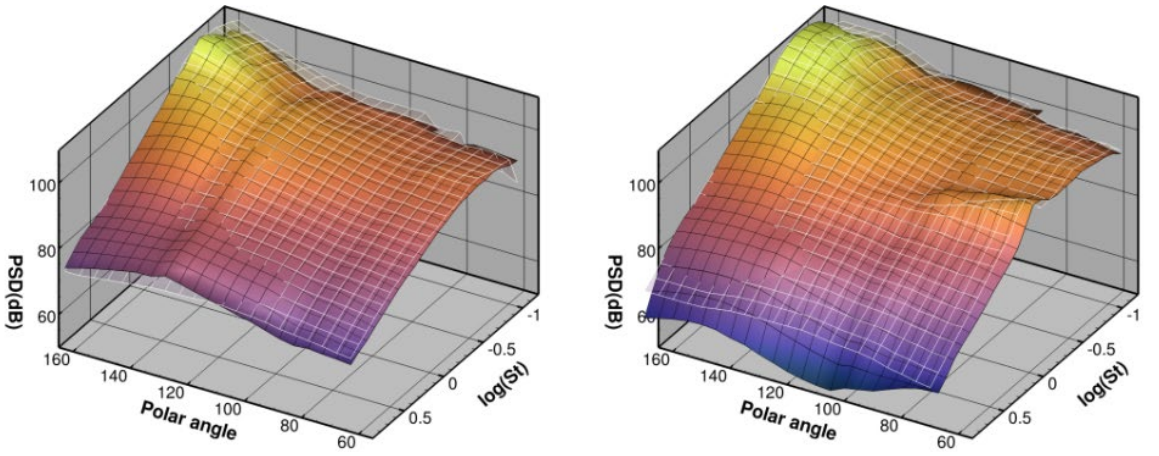


(a) Streamwise velocity. (b) Axial normal Reynolds stress.

Figure 58.—Time-averaged flow field quantities for SP101240 static (above dashed line) and SP101244 in flight (below dashed line).



(a) SP100024: Ma = 1.01; NPR = 1.61; NTR = 1.39. (b) SP101244: Ma = 1.13; NPR = 1.60; NTR = 1.78.



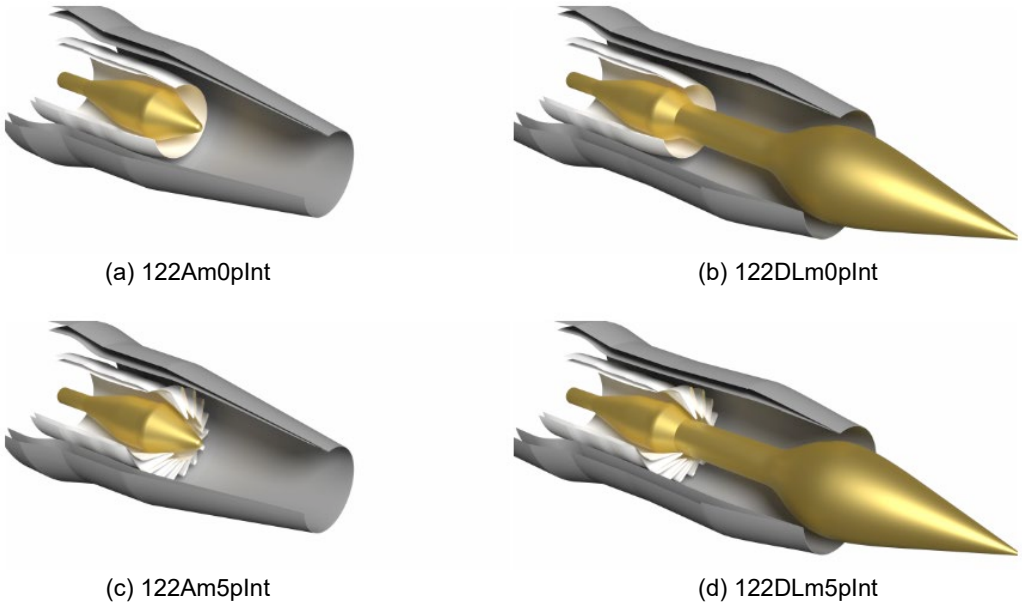
(c) SP100274: Ma = 1.20; NPR = 1.87; NTR = 1.78. (d) SP100084: Ma = 1.32; NPR = 2.11; NTR = 1.47.

Figure 59.—Visual depiction of spectral directivity of far-field noise at $100D_{jet}$. Comparison of WMLES (black grid) with experiments (white grid) from Reference 28.

5.4 Validation on Internal Mixers—Gaps in Simulation of Plug20

The next step in this systematic study of prediction uncertainty, after validating and assessing uncertainties for conventional single-stream round jets in static and in-flight conditions, is to move towards supersonic configurations. Information on this is published in Stich et al. (Ref. 82). This study focuses on the aeroacoustic implications of multistream nozzle configurations with internal mixing generated by the addition of both internal and external plug geometries. In this work, we used WMLES within the LAVA computational framework to predict the noise characteristics of these more complex configurations. The four considered configurations are depicted in Figure 60. The research addresses the challenges posed by the internal mixing of multiple streams and the interaction with internal and external plugs, which are critical for the next generation of quiet supersonic commercial jets. We simulated various operational conditions, as displayed in Table 6, to understand the impact on both the flow field and the resulting noise spectra. By comparing the simulation results with experimental data, we aimed to quantify the accuracy of our predictions and identify areas for further improvement. This comprehensive approach ensures that we can reliably use these advanced simulation techniques to guide the design and optimization of low-noise supersonic propulsion systems.

In part I of this study, we applied established aeroacoustic best practices to these more complex supersonic nozzle configurations with internal mixing and plugs. We aimed to validate these methodologies, which have been well-validated in simpler jet flows, under the increased complexity of supersonic nozzles featuring intricate geometric variations and demanding flow conditions. This involved detailed comparisons between CFD predictions and experimental data, focusing on both near-field flow and far-field acoustic measurements. The objective was to assess where these traditional practices maintained their predictive accuracy and where discrepancies emerged.



(a) 122Am0pInt (b) 122DLm0pInt

(c) 122Am5pInt (d) 122DLm5pInt

Figure 60.—Dual-stream, internally mixed Plug20 nozzles used in this study. (a) Internal plug nozzle with axisymmetric splitter m0. (b) External plug nozzle with axisymmetric splitter m0. (c) Internal plug nozzle with lobed mixer m5. (d) External plug nozzle with lobed mixer m5.

TABLE 6.—MATRIX OF EXPERIMENTAL AND SIMULATION DATA USED IN PLUG20 LES STUDY (REFS. 83 AND 84). SETPOINTS 70 TO 75 ARE SINGLE-STREAM, UNHEATED WITH FLIGHT, SETPOINTS 1180 TO 1203 ARE DUAL-STREAM WITH FLIGHT

Setpoint	DLm0p2069			DLm0p2069			DLm0p2069			DLm0p2069		
	PIV	FF	CFD	PIV	FF	CFD	PIV	FF	CFD	PIV	FF	CFD
70	✓	✓	✓	✗	✓	✓	✗	✓	✓	✓	✓	✓
71	✓	✓	✓	✗	✗	✗	✗	✗	✗	✗	✗	✗
73	✓	✓	✓	✗	✗	✗	✗	✗	✗	✗	✗	✗
75	✓	✓	✓	✗	✗	✓	✗	✗	✓	✗	✗	✓
1180	✗	✓	✓	✗	✓	✓	✗	✗	✓	✗	✓	✓
1183	✗	✓	✓	✗	✓	✓	✗	✓	✓	✗	✓	✓
1200	✓	✓	✓	✓	✓	✓	✗	✗	✓	✓	✓	✓
1203	✓	✓	✓	✓	✗	✓	✗	✓	✓	✓	✓	✓

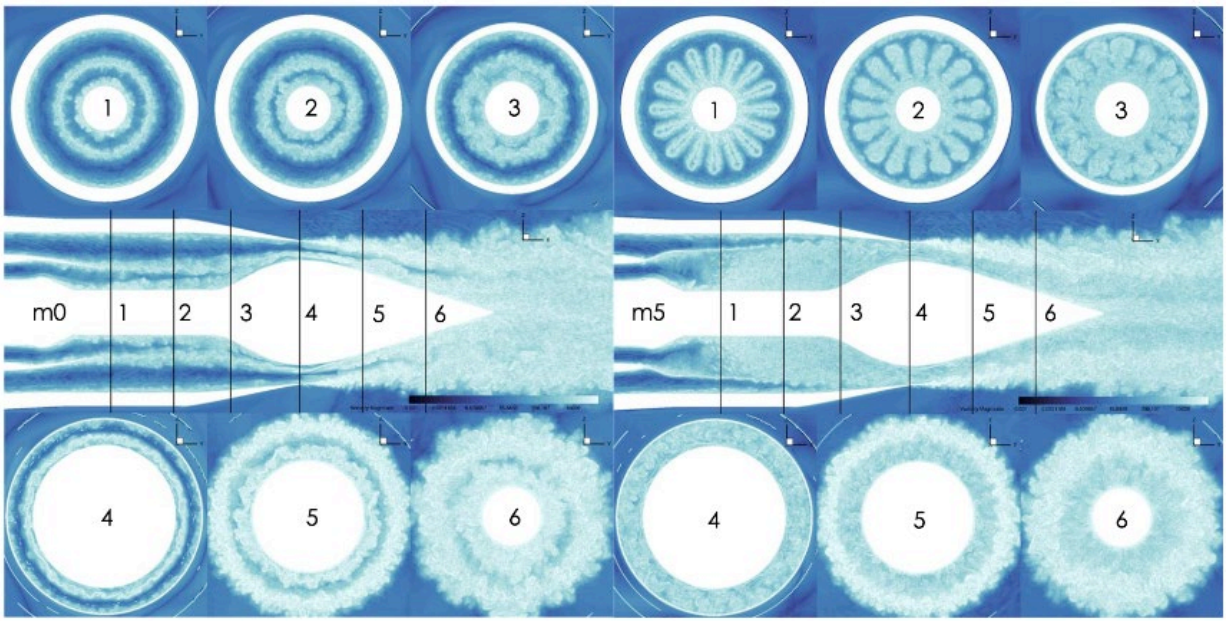


Figure 61.—Contours of Vorticity Gradient Magnitude for the Dual-Stream (122DL), External Plug (p2069) Configuration: This figure presents contour plots at various streamwise cuts, comparing the axisymmetric splitter (m0) on the left with the lobed mixer (m5) on the right.

In our investigation, we explored the effects of integrating a lobed mixer compared to an axisymmetric mixer. Figure 61 illustrates the significant impact of the lobed mixer on the flow field. The lobed mixer enhances turbulent mixing, resulting in a more homogeneous flow at the nozzle exit. This increased mixing efficiency is evident in the vorticity gradient magnitude contours (Figure 61), where the lobed mixer disrupts the shear layers, leading to an almost fully mixed flow at the exit station. This comprehensive mixing contrasts sharply with the axisymmetric mixer, which maintains distinct shear layers up to the nozzle exit. The enhanced mixing achieved by the lobed mixer is critical for optimizing thrust and potentially reducing jet noise significantly. A more detailed analysis is presented in Stich et al. (Ref. 82).

We observed notable differences in noise predictions between the two mixer configurations. Figure 62 shows the directivity plots of far-field noise for SP1180 as well as the difference plots between experimental data and WMLES. For the axisymmetric mixer configuration (m0), there was a consistent underprediction of the power spectral density (PSD). Despite various methodological and geometric modifications, including adjustments to mesh resolution and changes in the turbulent boundary layer, the underprediction persisted. Near the jet noise peak, the WMLES results aligned more closely with experimental data, even capturing the characteristic hump in the frequency spectrum around 3,000 Hz. For the lobed mixer (m5), the results showed good agreement with experimental data in low-to-mid frequencies, with differences generally being less than 2 dB except at higher frequencies. However, the simulations failed to predict the high-frequency spectral details observed in the experimental results. This suggests potential limitations in the current modeling approach or numerical setup. Further investigations are planned to explore the conditions under which this high-frequency hump occurs and identify potential modifications to enable accurate LES predictions of this phenomenon.

5.5 Historical Data Sets Used—Excess Noise Source Physics for Modeling

The primary need for a new empirical model for jet noise was that publicly available models did not capture noise sources related to internal lobed mixers. They also did not capture the impact of an external plug. Prior to the beginning of the TC, a test program was created and partially executed that produced data for a single lobed mixer with variations in the external plug, the length of the nozzle, and whether the plug was external or internal. This test was called Plug20 and was invaluable for validating LES and to show that the most important attribute acoustically wasn't the external plug but the lobed mixer.

Although the LES tool to be used in the TC was validated for single-stream nozzles over a wide range of hot and cold flows, with and without flight, it did not reproduce the noise data from the Plug20 test. Most specifically, it did not have the internal noise source that was characteristic of this and other tests with internally mixed exhaust systems. In the absence of noise data from LES, it was required to turn to historical data of internal lobed mixers for modeling the internal noise sources. Although these geometries did not have an external plug, they did have several variations on mixer geometry and some variation on nozzle length.

The historical data sets used came from jet noise tests conducted in collaboration with Allison Engines and then Rolls-Royce LibertyWorks in 1995 to 2006. The geometries of the tested nozzles are not generally publicly available, being a mix of proprietary and NASA-owned geometries, but the acoustic data belongs to NASA. Much of the work had been presented by Rolls-Royce authors in open publications (Refs. 79 to 84) where they carefully did not disclose all necessary information to reverse engineer the data. The mixers tested included variations in lobe count, lobe height, sidewall cutback, and two with alternate lobe tips clipped. The nozzles varied in length, relative to the mixer exit, from 0.5 D to 1.25 D, where D is the nozzle exit diameter. A total of 10 mixers and three nozzle lengths were included in the modeling effort.

As the historical data sets seemed to capture the internal noise sources shown to be critical in the supersonic-relevant Plug20 test, it was decided to use them to create an acoustic model for internally mixed nozzle systems while the shortcomings of the LES tools were addressed. The empirical models so derived would be applied to the TC database, assuming that the internal mixer source was the main source of deviance found in the baseline uncertainty assessment.

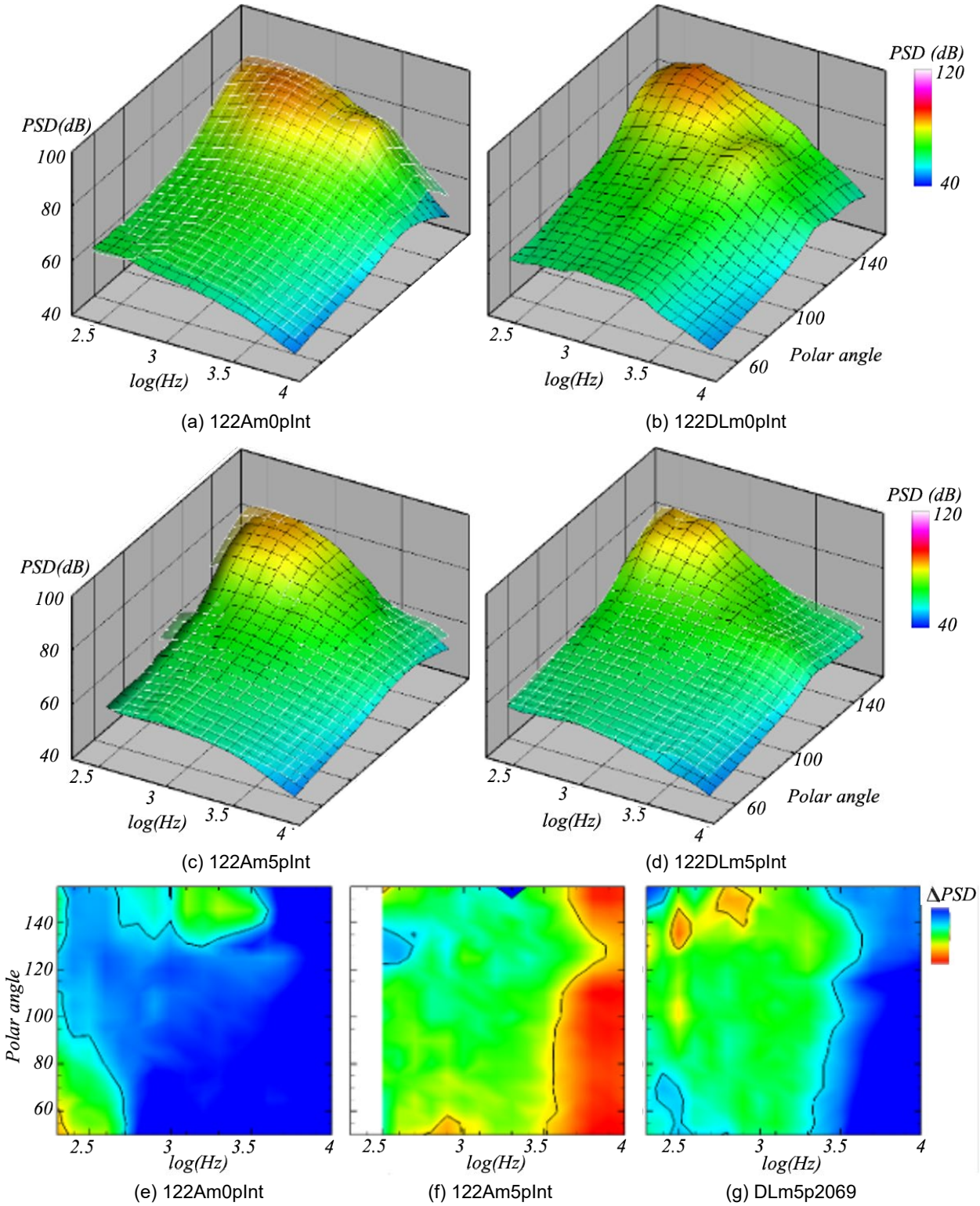


Figure 62.—SP1180. (a) to (d) Far-field spectra directivity comparison between WMLES LAVA data and rig data. Solid surfaces with black mesh represent WMLES data, while transparent surfaces with white mesh depict rig data. Panels (e) to (g) illustrate differences between WMLES and rig data (WMLES – rig), with black contour lines representing ±2 dB levels.

5.6 Validation of Rig Data Against Flight Data

System-type prediction tools for jet noise are developed predominantly from scale-model data. These data have been found to underpredict jet noise in flight (Ref. 91). One approach to compensate for deficiencies in the scale-model-to-flight comparisons is to apply an offset when using empirically based models for system-type studies of future supersonic aircraft. This approach can lead to unacceptably large uncertainties in the predictions. The improvement of the models and a quantification in the uncertainties associated with the application of existing models has been hindered by a lack of data from well-instrumented flight and accompanying scale-model tests. This section of the report details scale-model-to-flight investigations used to assess current predictions of jet noise from scale-model data.

A flight test was performed with a Learjet 25D in September 2022. The aircraft was selected for its CJ610 turbojet engines, which are expected to result in jet-noise-dominated acoustic radiation for the aircraft in flight. The aircraft, shown in Figure 63, was owned and operated by Calspan Corporation under contract with NASA. Acoustics tests were conducted at the Niagara Falls International Airport using an 800-ft, nine-element microphone array placed on a decommissioned runway (see Figure 63). Acoustic data were acquired for more than 70 flyovers where the aircraft performed a steady climb maneuver over the array to maintain constant airspeed and engine exhaust conditions. Atmospheric temperature, pressure, and humidity were recorded at roughly one-hour intervals with the drone shown in Figure 64 (Ref. 92). Wind velocity was measured with a ground-based LiDAR system. Aircraft position, engine exhaust gas temperature, engine pressure ratio (EPR), and aircraft speed were recorded throughout all flights. The nozzle pressure ratio (NPR), which is an important parameter describing the jet noise source strength, is determined from the EPR and the ambient atmospheric pressure.

Accompanying scale-model tests were performed in the Aero-Acoustic Propulsion Laboratory (AAPL) using the 0.31 scale model of the CJ610 nozzle system shown in Figure 65. All internal flow contours of the engine nozzles were replicated in the model. The engine uses a dual-stream nozzle but only the primary exhaust is powered. The secondary nozzle is used to exhaust cooling air entering the engine through a NACA scoop at the front of the nacelle.



Figure 63.—Learjet flight location, Niagara Falls International Airport, with microphone array and aircraft rotation point indicated. Learjet 25D used in flyover tests is shown in upper right. Lower right shows researcher inspecting ground microphones used in test.



Figure 64.—Weather drone used for atmospheric measurements during Learjet flight tests.

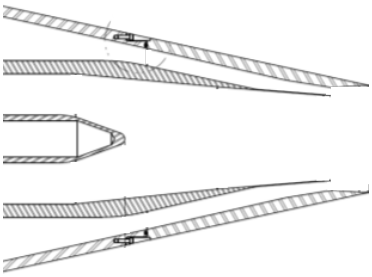


Figure 65.—Nozzle system used in scale-model tests.

TABLE 7.—FLIGHT CONDITIONS

Nominal NPR = 1.7			Nominal NPR = 1.9		
NPR	NTR	Mach #	NPR	NTR	Mach #
1.695	2.718	0.256	1.906	2.901	0.265
1.694	2.717	0.251	1.896	2.883	0.262
1.703	2.716	0.264	1.890	2.879	0.252
1.685	2.711	0.251	1.896	2.884	0.252
1.681	2.710	0.249	1.925	2.890	0.282
1.686	2.717	0.253	1.899	2.884	0.268
1.686	2.692	0.249	1.912	2.885	0.271
1.686	2.689	0.247	1.898	2.839	0.282
1.682	2.693	0.261			

TABLE 8.—CENTER REPEAT POINTS

Nominal NPR = 1.7			Nominal NPR = 1.9		
NPR	NTR	Mach #	NPR	NTR	Mach #
1.686	2.704	0.257	1.903	2.881	0.267

Two sets of data were acquired in the scale-model tests. The first set replicated the conditions for the flight test at each nominal NPR achieved in the flyover test. Each condition was associated with an individual flyover and each nominal NPR had eight to ten flyovers. The second set of data acquired acoustic spectra for a center point for each nominal NPR. The center-point acquisition for each nominal EPR was repeated 12 times with the tunnel condition being reset for each acquisition. Individual flyover conditions were retained for further analysis if the average and standard error of the mean were nearly the same for the flight-condition and associated center-point data sets. The standard error of the mean is a measure of the spread in the average values obtained from different flyovers or different data samples acquired in the tunnel. The flight and center-point conditions for two nominal NPRs are shown in Table 7 and Table 8. Flight and scale-model tests acquired data for six different nominal NPRs between 1.6 and 2.1.

The flight spectra from nine flyovers and their average for a nominal NPR = 1.7 are shown in Figure 66. Emission angles greater than 90° are aft of the aircraft. A secondary nonjet-noise source is seen in the data at emission angles between 70° and 130° and circled in red on the plot for an emission angle of 110°. Additionally, a first shaft-order tone, observed in all spectra, is not jet noise related. Reasonable agreement is found between the different flyovers.

The average spectra for the scale-model data using the flight and repeat conditions are shown in Figure 67. The associated standard errors of the mean are shown in Figure 68. Nozzle Acoustic Test Rig (NATR) is used synonymously with scale-model data. The results show the average spectra are the same, and the standard errors of the mean are similar for the two data sets. Based on the results in Figure 67 and Figure 68, the variations in spectra obtained at the different flight conditions, and therefore the different flyovers at the same nominal NPR, are assumed to be the same as those that would be achieved for multiple measurements at the same average condition.

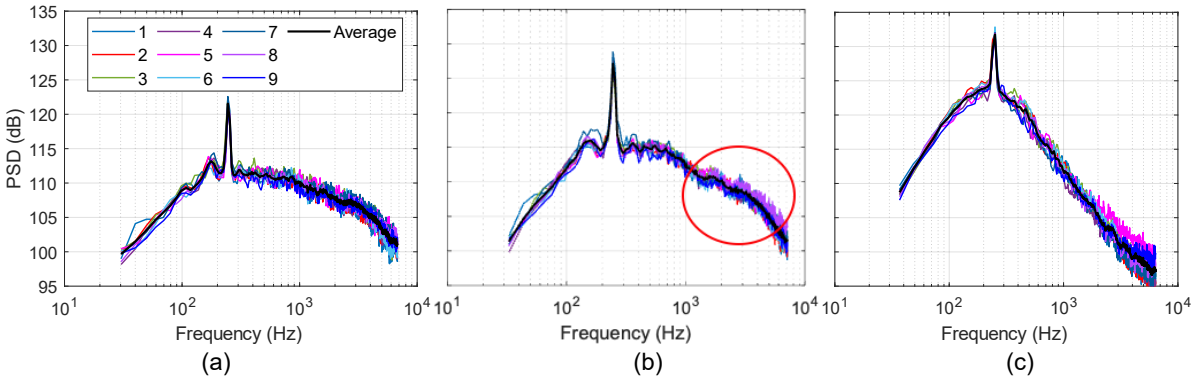


Figure 66.—PSD for nine flyovers and their average at nominal NPR = 1.70 and emission angles of (a) 70°, (b) 110°, and (c) 150°. Nonjet source circled in red.

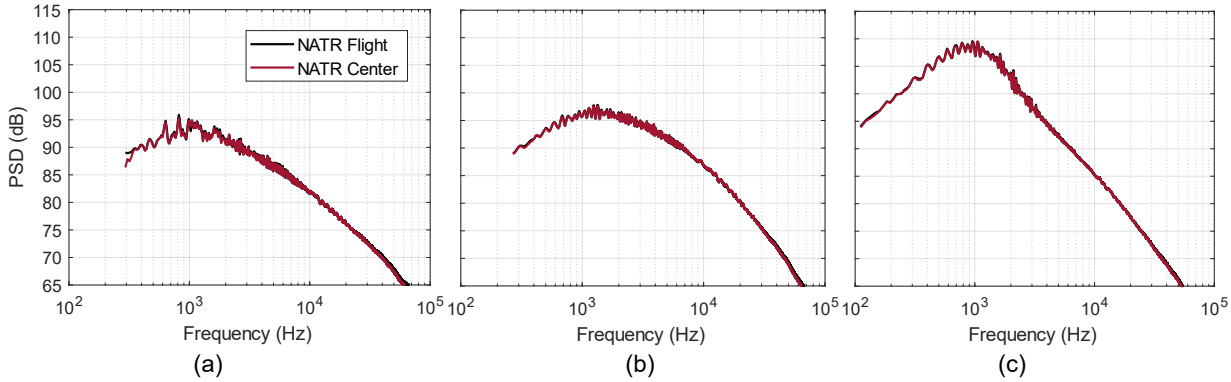


Figure 67.—Average PSD for flight conditions and center points at nominal NPR = 1.70 and emission angles of (a) 70°, (b) 110°, and (c) 150°.

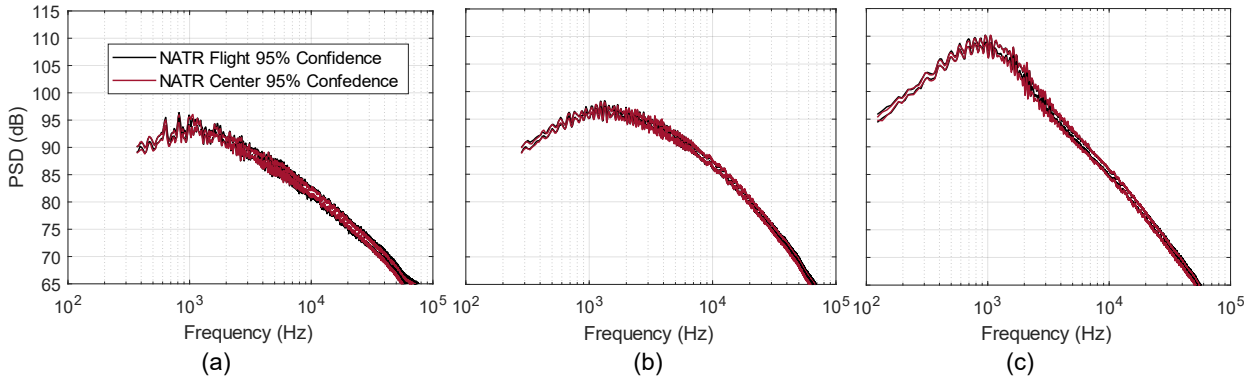


Figure 68.—Ninety-five percent SEM confidence interval for nominal NPR = 1.70 and emission angles of (a) 70°, (b) 110°, and (c) 150°.

Comparisons between the average PSD acquired at nominal NPR = 1.7 flight conditions for the scale-model and flight tests are shown in Figure 69. The first shaft-order tones have been removed from the flight spectra. A scale factor of 3.4 has been applied to the rig data to match the flight data. This is 6 percent greater than the true geometric difference, increased to align peak frequencies and levels of the scale-model data with the flight data (Ref. 91). Further investigations are required to understand the physics behind the difference in scale factor. The peak levels agree reasonably well for the flight and scale-model data at all emission angles.

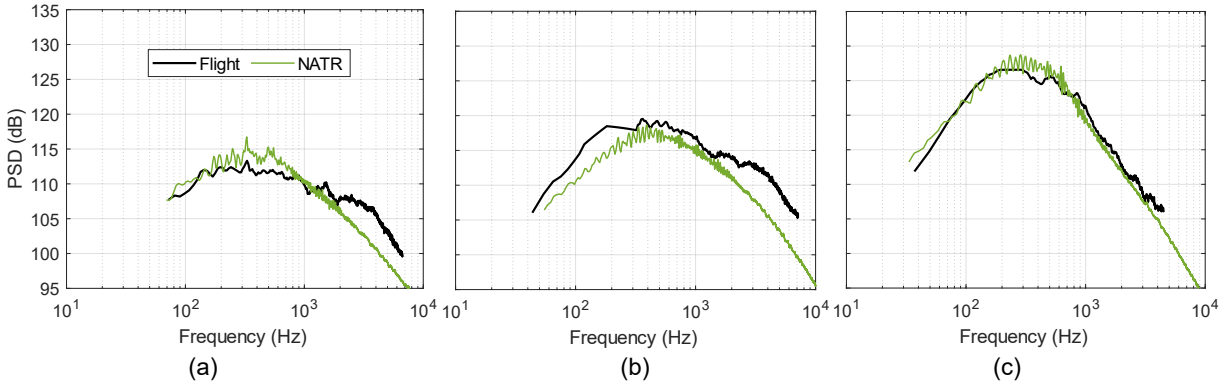


Figure 69.—Average PSD for flight and scale-model tests computed from flight conditions for nominal NPR = 1.70 and emission angles of (a) 70°, (b) 110°, and (c) 150°.

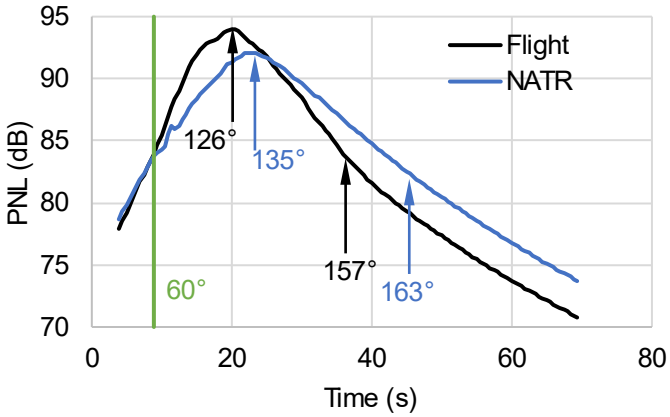


Figure 70.—PNL for flight and scale-model (NATR) tests for NPR = 1.9.

TABLE 9.—COMPUTED EPNL VALUES AND 95 PERCENT CONFIDENCE-LEVEL UNCERTAINTY BOUNDS

Nominal	Learjet Flight Test			AAPL/NATR Scale-Model Test			Lear-AAPL
NPR	EPNLdB	EPNLdB–	EPNLdB+	EPNLdB	EPNLdB–	EPNLdB+	ΔEPNLdB
1.6	88.0	85.6	89.5	86.2	85.1	87.1	1.8
1.7	90.9	88.8	92.3	89.4	88.7	90.1	1.4
1.8	93.3	91.1	94.8	92.2	91.4	92.9	1.1

The trajectory taken from Reference 15 was used for EPNL calculations. The PNL as a function of time for a nominal NPR = 1.9 is shown in Figure 70. Emission angles for the peak PNL and for one of the 10 dB down points are indicated in the figure. The peak PNL is slightly higher for the flight data than for the scale-model data. Additionally, the roll-off of the PNL with time at large emission angles is greater for the flight data than for the scale-model data. Further investigations are required to improve the PNL roll-off region of the scale-model PNL.

The EPNL and 95 percent confidence-level uncertainty bounds for NPR = 1.6 to 1.8 are shown in Table 9. The computed EPNLs are 1.1 to 1.8 higher for the scale-model data than for the flight data.. The confidence intervals are wider for the flight data (3.5 to 3.9 dB) than for the scale-model data (1.4 to 2 dB). However, the scale-model EPNL falls within the 95 percent confidence interval for the flight data. Additional details are found in References 93 and 94.

5.7 Improvements to Jet Noise Models

5.7.1 Improved Noise Prediction Method for Single-Stream Jets

The single-stream jet noise models in the NASA noise prediction code ANOPP do not adequately predict single-stream scale-model data (Refs. 63 and 91). The NASA jet noise model named "sJet" is better, but it is primarily an interpolation on experimental spectra from static jet tests. A new model with analytic description and extending to jets in a flight stream is needed. A new empirical model (Ref. 95) was developed from data acquired in the freejet facility within the Aero-Acoustic Propulsion Lab and used to predict noise from single-stream jets over the ranges of $1.5 \leq NTR \leq 3.0$, $1.4 \leq NPR \leq 1.8$, and $0.0 \leq M_{fj} \leq 0.3$, where M_{fj} is the flight stream Mach number, NTR and NPR are nozzle temperature and pressure ratio, respectively. The spectra at different NPR were first collapsed at the same NTR, emission angle, and flight Mach number to master spectra after appropriate scaling by a power of the relative acoustic Mach number computed from the difference in the jet and flight stream velocities and the ambient speed of sound. Peak shape functions were fit to the master spectra and the parameters for the functions were determined for static jets. Slight adjustments to a couple of the parameters were found to fit the master spectra for the jets with flight streams. The master spectra and the peak shape functions for an emission angle of 140° are shown in Figure 71. This model is awaiting the completion of validation tests against Learjet flight data before being deployed. It is anticipated that the new model will be more robust than the sJet model being used in the PUR TC, which requires a separate model to account for the effects of flight.

5.7.2 Improved Noise Prediction Method for Internally Mixed Exhaust Systems

The modeling of the jet noise from internally mixed exhaust systems was based on historical concepts (Ref. 96), but quantified using more modern methods and better prediction tools. Historically, the noise from internally mixed nozzles were considered to be divided into noise produced inside and outside the nozzle. The outside noise sources were thought to be the same as a single-stream, fully mixed jet, with some changes due to high-speed streaks where the internal mixing had been incomplete. The internal noise source was more of a mystery, often considered to be the noise of the internal shear layer but somehow amplified.

In the modeling approach used for PUR TC, the first step was in validating an empirical noise code for hot single-stream jets in flight and seeing how much the noise of the internally mixed two-stream jet deviated from this. The sJet code created by Khavaran and Bridges in 2005 (Ref. 97) was found to give good agreement with the single-stream cases in the PUR uncertainty assessment data set, and was chosen

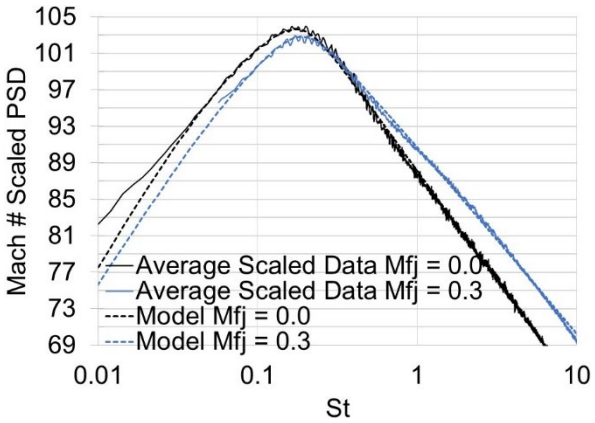


Figure 71.—Master spectra and empirical models for NTR = 2.5 and indicated flight Mach numbers.

over other publicly available alternatives. When the historical data set was compared to predictions of sJet, the deviation was found to correlate with mixer parameter of lobe height and with the velocity ratio of the two-stream flow. Creating a model for this correlation and adding it to the sJet prediction produced the empirical model sJetMod22, with a significant improvement in the ability to predict the PUR TC data set consisting of data from the Plug20 test of 2020 (Ref. 83) and the GE N+2 test of 2010 (Ref. 98).

The second step was to create a model for the internal noise. As described in Reference 99, once the external jet noise source was clearly identified, the remaining noise was found to match several criteria that corroborated its internal origins. The source mechanism was not clear at first, and the next version, sJetMod23, made a very broad attempt at modeling this noise without good physical basis. The result was a strong improvement in ability to predict the TC data set but did not seem applicable beyond the parameters of the historical database.

The third and final version of the empirical model, sJetMod24, resulted from insights gained from the ongoing LES runs, design efforts to create the next generation supersonic nozzle, and acoustic modal analysis of the nozzle system. Under the hypothesis that the internal noise was primarily caused by unsteady separation of the flow in the lobed mixers, triggered and organized by acoustic resonance in the nozzle, a more detailed, physics-based model was created for this noise source. The new model not only fit the range of parameters in the historical data set but also the Plug20 data set representing exhaust systems for supersonic aircraft. The final improvement came from including a broadband shock noise model for exhaust flows with pressure ratios higher than 1.9. Although such high-velocity jets are not likely to be able to meet noise requirements, they are included in the TC uncertainty analysis and need to be properly predicted when systems engineers push the engine performance boundaries. A full description of the model, including analytical expressions needed to encode it, are given in Reference 100.

6.0 Airframe Noise Modeling

6.1.1 Previous Studies

During the High Speed Research Program, Herkes and Stoker (Ref. 25) acquired far-field acoustic data on a 3 percent scale-model of the High-Speed Civil Transport (HSCT) aircraft. Major airframe noise sources were identified from phased microphone array measurements. Although this test provided valuable information into the acoustic behavior of supersonic transports at low speeds, the extremely small scale of the models and the high passenger count of the concepts severely limited their application to the study of supersonic business jets, such as are anticipated in the near term. For example, in Reference 25, the measured data contained a significant level of uncertainty due to the low signal-to-noise ratio (SNR) introduced by high tunnel background noise.

Also absent from the literature are computational airframe noise studies of supersonic business jets in landing configuration. Numerical simulations with high physical fidelity have made significant inroads as a viable, complementary tool to wind tunnel testing for airframe noise characterization. Previous efforts conducted under the NASA Environmentally Responsible Aviation and Flight Demonstrations and Capabilities projects clearly established the applicability of physics-based computational simulations to two essential aspects of airframe noise prediction for sub- and full-scale subsonic aircraft in landing configuration: identification of primary and secondary sources and generation of accurate far-field noise footprints (Refs. 39 to 42). The vetted accuracy and wide acceptance of high-fidelity simulations provide ample justification for exploratory airframe noise predictions to lower the uncertainty in system-level

acoustic analyses of supersonic transports until complementary experimental tests can be performed. Thus, the present investigation aims to extend the computational methodology used in previous studies to commercial supersonic aircraft concepts to better understand the relevance of airframe sources to the far-field noise footprint of this transport class.

6.1.2 Generic Low-Boom Concept (GLBC)

After careful consideration, a generic low-boom concept (GLBC) airframe was selected as the surrogate geometry for this initial study. The GLBC is an early version of the low-boom X-59 supersonic demonstrator being built for NASA (Ref. 43). Although not a viable passenger-carrying supersonic business jet, two important attributes tilted the selection process in favor of the GLBC. First, if the opportunity arises during flight tests of the X-59, aeroacoustic data can be acquired to validate the high-fidelity computational approach. Second, a 15 percent scale model of the GLBC was tested in the NASA Langley Research Center 14- by 22-Foot Subsonic Tunnel (14×22) for low-speed aerodynamic characteristics of the configuration. Although not an acoustic test, the measured data provided sufficient aero information to validate the airframe noise simulations.

An exploratory study was executed in three phases. Given the vast differences between the flow fields of low aspect ratio supersonic wings and those of conventional subsonic aircraft, the initial phase focused on the accurate prediction of key aerodynamic characteristics of the GLBC. In this phase, the wind tunnel test section and model support system were included in the simulations as it was tested. The aerodynamic analysis and associated results obtained were presented in References 44 and 45 and are not included in this report. In the follow-up phase, airframe noise was predicted by conducting free-air simulations of the GLBC in various landing configurations (Ref. 45) to determine the contribution of various airframe components to the far-field noise. The third phase of the effort was to analyze the acoustic results, detailed in References 46. A summary of this acoustic analysis and a comparison against the predictions produced by the empirical methods used in the STCA is given in Section 6.1.12.

6.1.3 Model Description

The wind tunnel test article was a 15 percent scale-model of the GLBC C608 outer mold line. The reference parameters for the model-scale vehicle are provided in Table 10, and a CAD geometry of the simulated model is presented in Figure 72. For the purposes of airframe noise prediction, only a small subset of tested configurations was considered. The two main configurations of interest were flap 0° with landing gear stowed (Flap0-LGoff) and flap 30° with landing gear deployed (Flap30-LGon). Configuration Flap0-LGoff corresponds to an aircraft in cruise and represents the quietest possible (baseline) configuration; Flap30-LGon corresponds to a landing scenario when airframe noise is most prominent.

TABLE 10.—REFERENCE PARAMETERS FOR 15 PERCENT SCALE GLBC WIND TUNNEL MODEL

Parameter	Value
Reference area, in^2	1,575.158
Reference span, in.	53.100
Reference chord, in.	39.528

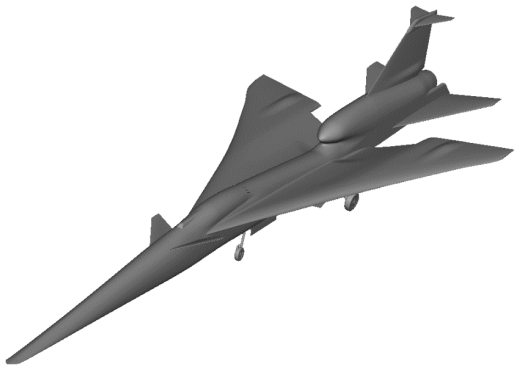


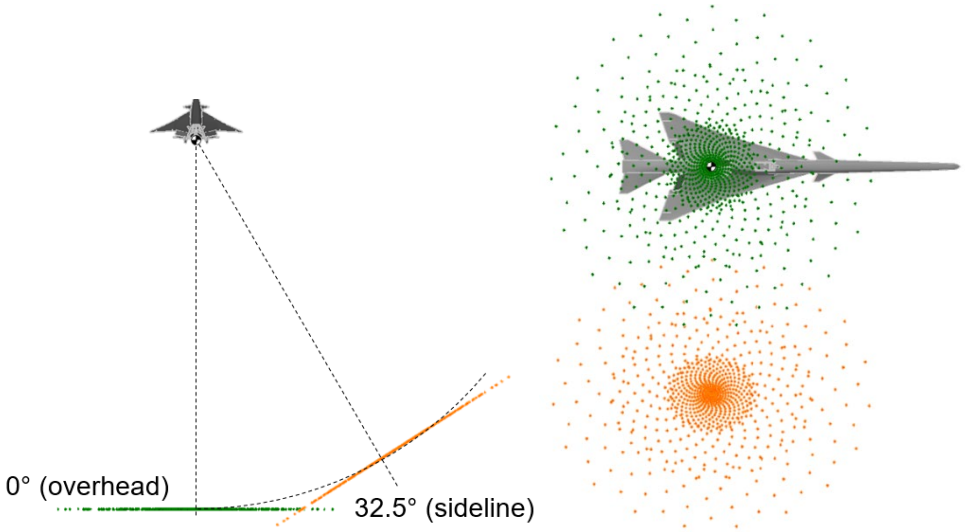
Figure 72.—Close-up image of GLBC CAD model with flaps deflected 30° and landing gear deployed (landing condition) in free-air setup.

6.1.4 Computational Data

All airframe noise simulations were conducted with the commercial lattice-Boltzmann solver PowerFLOW® (Dassault Systèmes Americas Corp.) described in References 44 and 45. These simulations were performed in free-air conditions, without the wind tunnel and model support system, to eliminate reflections from walls and allow the acoustic waves to propagate unimpeded to numerous observer locations. The simulated ambient parameters were set to values corresponding to the selected GLBC test runs in the 14×22 tunnel. The Reynolds number (based on mean aerodynamic chord), Re, and Mach number, M, were 4.4×10^6 and 0.2, respectively. The AoA was set at 9°, representative of aircraft landing conditions. Most computations were executed at two grid resolution levels (coarse and medium, corresponding to 1.5 billion and 5 billion cells, respectively) to determine the effect of spatial resolution on predicted aeroacoustic trends. For the most critical case of Flap30-LGon (landing configuration), an additional simulation was performed at a higher resolution level (fine, 17 billion cells).

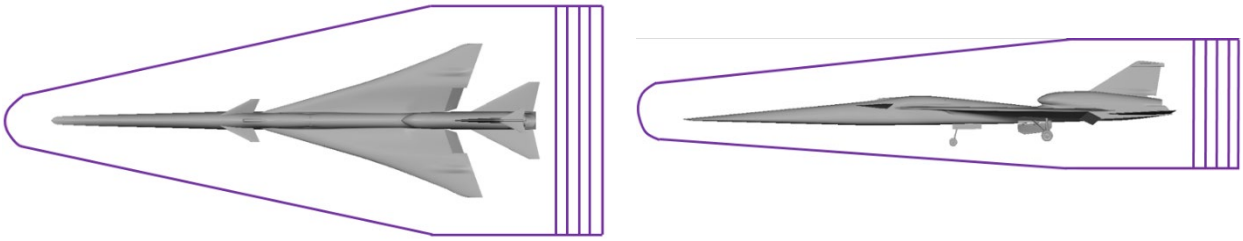
6.1.5 Synthetic Phased Microphone Array

Due to the lack of experimental noise measurements for the GLBC model, the present exploratory acoustic analysis relied solely on simulated (synthetic) pressure fields. Not constrained by the 14×22 tunnel, a synthetic array of 800 phased microphones was developed and used for precise resolution and ranking of prominent airframe noise sources of the 15 percent scale GLBC model. The nonredundant array pattern comprised three nested, multiarm, spiral subarrays targeting different frequency ranges. More details about the array design can be found in Reference 47. The array was scaled to obtain the desired array resolution based on its relative distance to the aircraft. A hyperbolic tangent-based shading algorithm was employed during beamforming to improve array resolution while preserving a good SNR for all frequencies of interest (about 10 dB at low frequencies and at least 16 dB at mid-to-high frequencies). The array was placed directly underneath the GLBC in the flyover direction and at an azimuthal offset of 32.5° in the sideline. Schematics of the array position relative to the model and the microphone pattern are shown in Figure 73. The array was designed for an operational frequency range of approximately 1.0 to 50 kHz (0.15 to 7.5 kHz full-scale). The synthetic microphone array pressure records contain nearly 0.065 s of simulated physical time (0.4 s in full-scale).



(a) Array positions (b) Microphone patterns

Figure 73.—Phased microphone array positions and configurations. Green dots represent microphones in overhead array and orange dots signify microphones in sideline array.



(a) Top view (b) Side view

Figure 74.—GLBC model with permeable FW-H data surface drawn in purple lines (from Ref. 45).

An acoustic analogy approach based on the FWH formulation (Ref. 49) was used to propagate the computed near-field pressure fluctuations to the array microphone locations. For all simulated configurations, data collected on a tailored FWH-permeable surface were used as input to calculate the far-field pressure records at the two array locations. For Flap30-LGon, the computed unsteady pressure field on the GLBC solid surface was also used as input. The permeable data surface is shown in Figure 74, including a series of end caps used to reduce the effects of hydrodynamic fluctuations exiting the surface. Notice that unlike the permeable data surfaces used for conventional subsonic aircraft, the present surface encloses a large volume above the model. This was done to properly contain the highly interactive, complex, off-surface vortical flow field that develops on the upper surface of the model (see Figure 75).

6.1.6 Synthetic Array Data Processing and Integration Regions

The simulated pressure records were beamformed in the frequency domain and post-processed using the CLEAN technique (Ref. 50) as implemented in AVEC's phased array software suite (Ref. 51). The beamform (source localization) maps were generated on a 6.3-by-3-m planar grid, with a resolution of 0.02 m in both directions, located at the mid distance between the GLBC landing gear wheels and wing. In this position, nearly all the airframe sources are close to the selected plane without significantly affecting the integrated levels. The location of the chosen beamforming plane is shown in Figure 76(a)

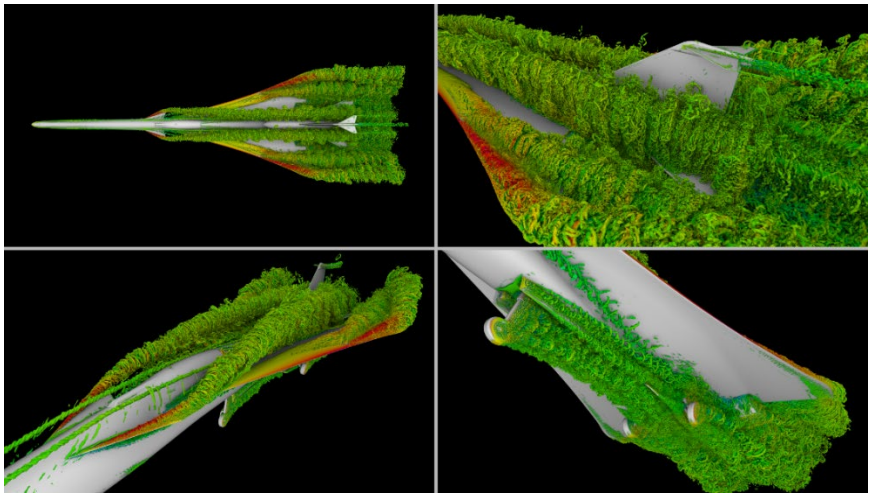


Figure 75.—Instantaneous vorticity field based on iso-surfaces of λ_2 criterion for GLBC model in landing configuration (Flap30-LGon). Results from free-air fine-resolution simulation at AoA = 9°.

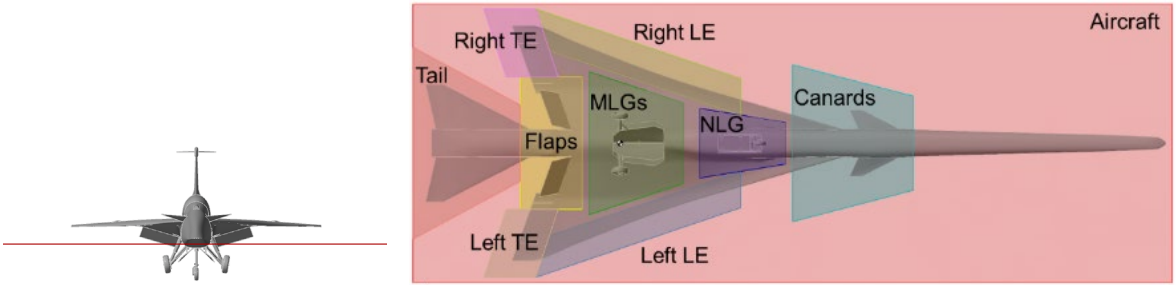


Figure 76.—Location of beamforming plane and regions used to calculate integrated far-field noise spectra. Grid resolution: 0.02 m. (a) Extent and position of beamforming plane. (b) Tailored integration regions.

and its extent is displayed in Figure 76(b). The narrowband beamform maps were generated using a bandwidth of 350 Hz and a 15 dB cutoff range.

To generate far-field spectra, the CLEAN beamform maps were integrated with a 10-dB cutoff. Carefully oriented integration regions were devised to extract contributions from various sections (components) of the aircraft as shown in Figure 76(b). The summation of contributions from all subregions (based on p^2) is termed “Sum” in Figure 78, Figure 81, and Figure 83 and is used to illustrate the total airframe noise produced by the GLBC. Unless stated otherwise, all spectra presented in the acoustic analysis correspond to the overhead position and all frequencies (e.g., beamform maps, spectral plots) represent model-scale values.

6.1.7 Effects of End Caps and Spatial Resolution

As illustrated in Reference 44, the large-scale, longitudinal vortices generated by the GLBC canard lifting surfaces and those produced at the wing leading edges persist for long distances downstream of the aircraft. Passage of such coherent structures through the exit plane of the permeable data surface is problematic and, in most cases, results in generation of spurious numerical sound sources. As shown in Figure 74, multiple end caps were devised and applied to diminish the contribution of these nonphysical

noise sources through end-cap averaging. The numerical sources may be circumvented also by ignoring the contribution of the end caps during FWH propagation when synthetic pressure records are generated at the array microphone locations. The resulting open permeable data surface causes errors primarily at acute directivity angles close to 0° and 180° (in the flyover direction). Reference 46 demonstrated that the predicted spectrum at the overhead position (90° directivity) was unaffected by end-cap removal. Therefore, all results presented in the following sections are with end caps removed.

6.1.8 Source Localization (Beamform) Maps

The Flap30-LGon configuration, the most challenging configuration, was simulated at three grid resolution levels and will be used to examine the effects of spatial resolution on the results. CLEAN beamform maps for the coarse, medium, and fine spatio-temporal resolution simulations are shown in Figure 77 at various frequencies. At a low frequency of 3.85 kHz (Figure 77(a)), all maps depict fairly converged source distributions and strengths for the primary noise sources – main landing gear (MLG) and flaps. Even the levels for weaker sources – nose landing gear (NLG), canards, and wing leading edges (LE) – show relatively good agreement among the maps. This good agreement extended to a moderate frequency of ~7.7 kHz for the most dominant sources, including flap inboard tips, MLG, and NLG (Figure 77(b)). Additional sources, such as those originating from flap outboard tips, emerge more clearly in the maps as resolution is increased. However, the distribution and strength of the sources

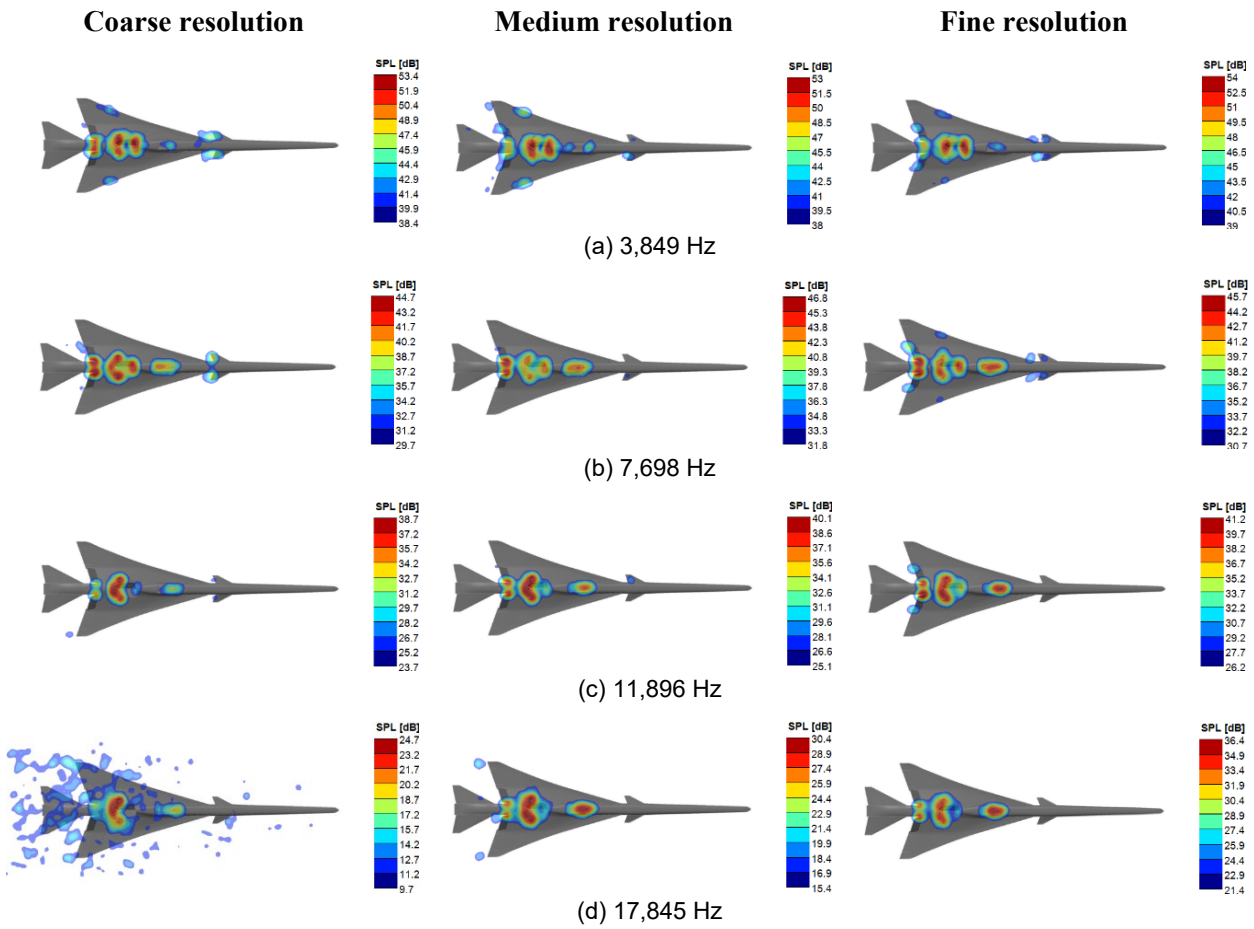


Figure 77.—Spatial resolution effects on CLEAN maps of landing (Flap30-LGon) configuration (from Ref. 46).

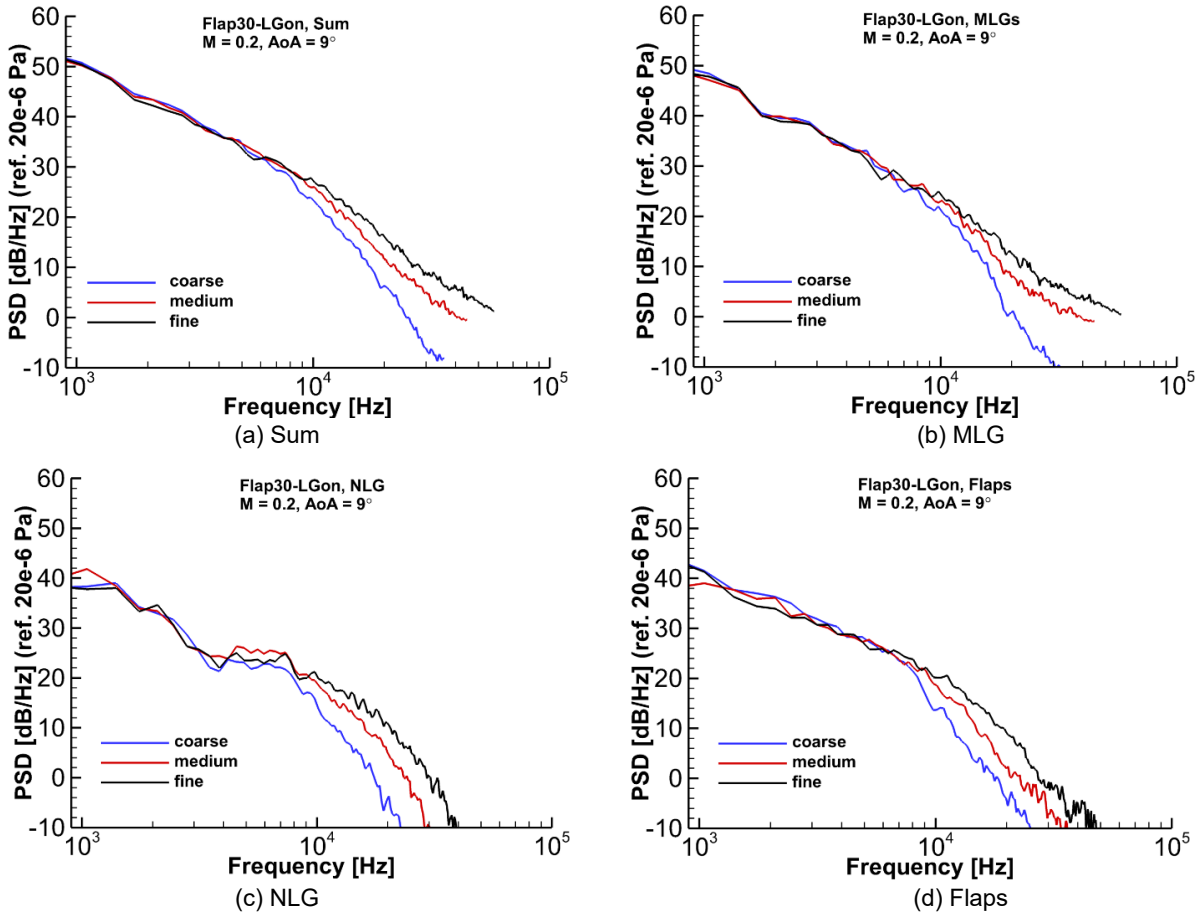


Figure 78.—Spatial resolution effects on integrated spectra of Flap30-LGon configuration—landing gear and flaps (from Ref. 46).

originating from the canards and wing LEs keep changing and do not display the typical convergence trends one would anticipate from increased spatial resolution. As illustrated in Reference 44, this behavior is caused mostly by the inherent difficulties in capturing leading edge separation on smooth surfaces that leads to shear layer roll-up and formation of large-scale longitudinal vortices for delta-wings that are typical of supersonic aircraft.

Convergence of the Flap30-LGon far-field noise spectra with spatial resolution is shown in Figure 78. In this figure, PSD spectra from summation (Sum) of all sources and from landing gear and flap components are presented for the simulated spatial resolution levels. For frequencies lower than 18 kHz, the spectra of Figure 78 indicate that, on both component and total noise levels, the medium-resolution simulation produced results that are within 2 to 3 dB of those obtained from the much more computationally expensive fine-resolution simulation. Therefore, the medium-resolution grid was selected to conduct most of the acoustic analysis for the GLBC model.

Far-field spectra obtained from integration of the canards and port wing leading edge (left LE) regions were also examined (Ref. 46). Unlike the spectra presented in Figure 78, where the levels were well converged at less than 10 kHz, the spectra for the sources in the canards and LE regions depict a nonmonotonic, slow convergence of the noise levels with increased resolution. This behavior is similar to that observed in the aerodynamic data for the LE vortices reported in Reference 44. The trends captured

for the canards and LE noise do not provide a clear indication of the appropriate spatial resolution at which fairly converged noise levels for sources lower than 10 kHz should be apparent. This convergence behavior, which seems unique to swept, low aspect ratio wings typical of supersonic aircraft, may be affected also by the significant difference in noise amplitude between secondary (canards, leading edges, and tail) and primary noise sources (landing gear and flaps). The result is a reduction in the accuracy of the secondary sources where their levels are lower than 10 dB from the peak in the beamform maps.

6.1.9 Overhead Versus Sideline Far-Field Noise Levels

In Figure 79, source maps from flyover (overhead) and sideline arrays at low and moderate frequencies, obtained from medium-resolution results for the Flap30-LGon configuration, are shown. The sideline maps feature primary sources with strengths similar to those in the flyover maps. However, the source distributions in the sideline maps are distorted and slightly off position. This is caused by parallax as the sources do not reside exactly on the selected grid plane (Figure 76). The most significant changes occur for the wing LE and canard sources. With the sideline array, increased shielding of the sources on the upper surface of the starboard wing and canard (farthest away from the microphones) is observed. Conversely, decreased shielding is noted for the LE and canard that are closer to the array.

Integrated spectra for total noise and the MLG component are depicted in Figure 80. Note from Figure 80(a) that the total noise produced by the model (Sum) remains unchanged between flyover and sideline observers. The main reason for this indifference is the modest change in noise produced by the MLG, NLG, and flaps (e.g., see Figure 80(b) for MLG component). As noted in the beamform maps of Figure 79, the largest differences between observers occurred in the asymmetry of the wing LE and canard sources. However, as the total source strength remains the same, the total sound does not change with observer.

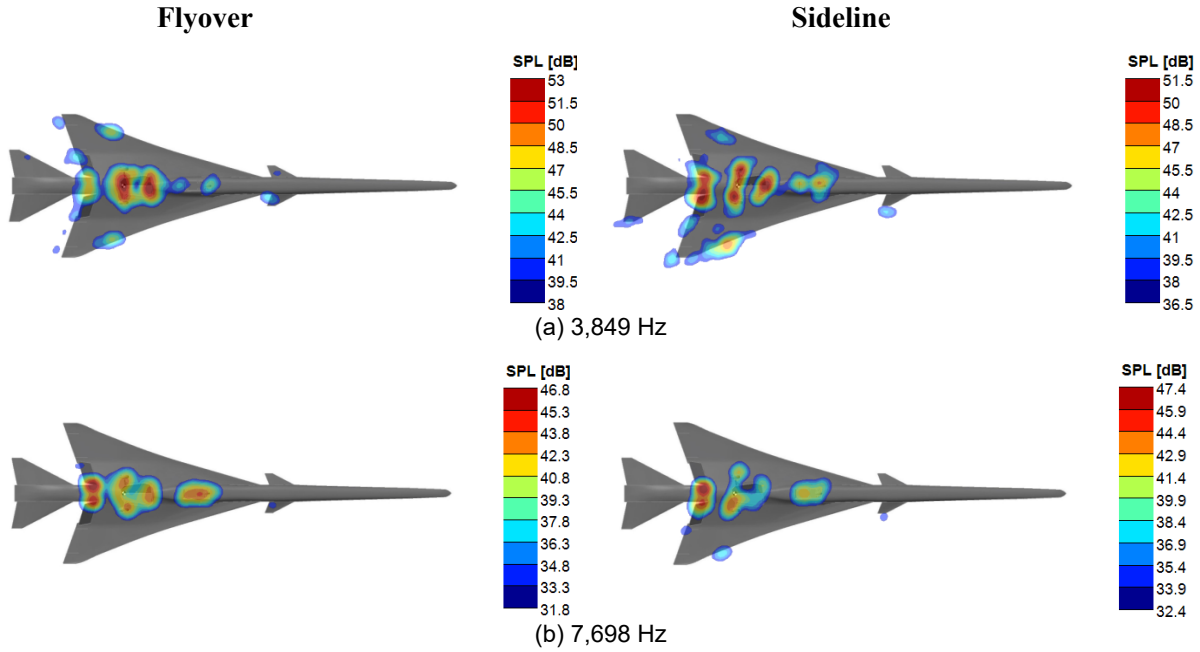
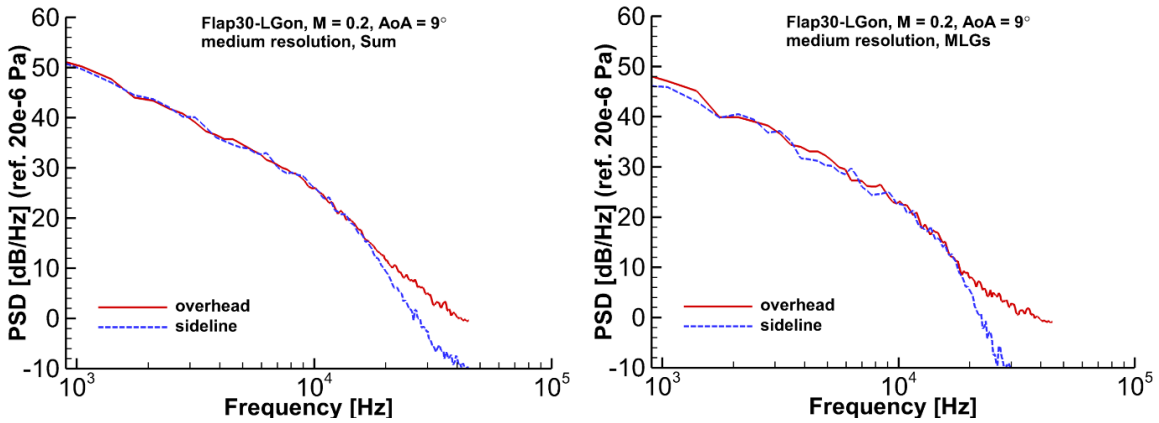
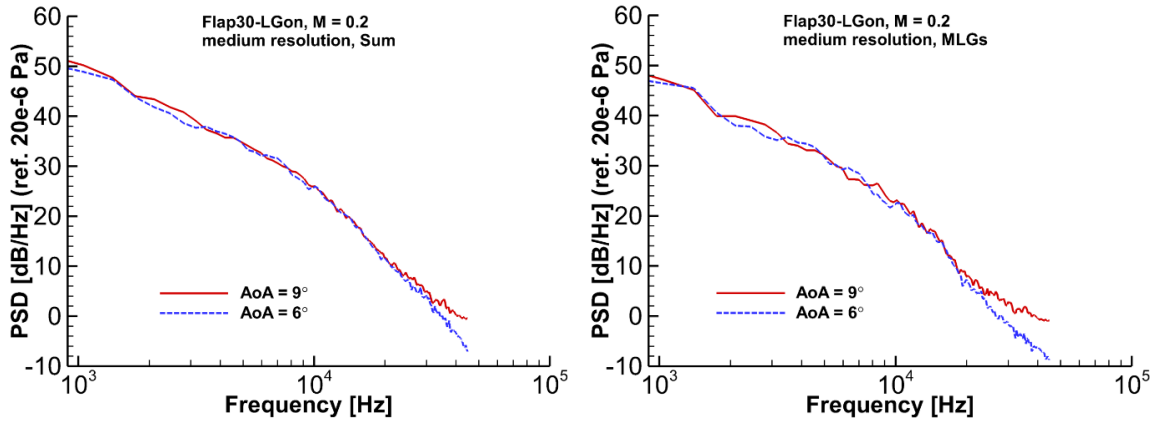


Figure 79.—Flyover and sideline CLEAN maps for Flap30-LGon configuration (medium resolution). From Reference 46.



(a) Sum (b) MLG

Figure 80.—Flyover and sideline integrated spectra for Flap30-LGon configuration (medium resolution)—landing gear and flaps (from Ref. 46).



(a) Sum (b) MLG

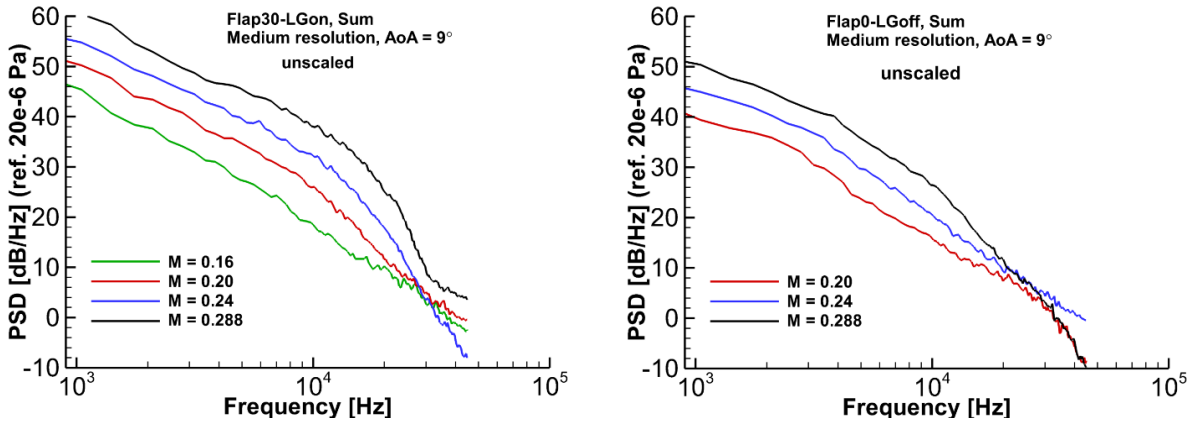
Figure 81.—Effects of AoA on integrated spectra for Flap30-LGon configuration (medium resolution)—landing gear and flaps (from Ref. 46).

6.1.10 Angle-of-Attack (AoA) Effects

For conventional subsonic aircraft, airframe noise displays a weak dependency on AoA at the low-to-moderate angles typical of landing conditions (Ref. 52). To confirm that a similar trend holds for supersonic aircraft, a free-air, medium-resolution simulation of the Flap30-LGon configuration for M = 0.2 and AoA = 6° was also performed. The resultant integrated spectra for the Sum and the MLG component of the GLBC model are shown in Figure 81. The total noise produced by the model, as well as the noise generated by the MLG are independent of AoA (within the limited range examined here). A similar trend was observed also for the integrated spectra associated with NLG and flaps. The canards, LE, and trailing edge (TE) regions do show noticeable differences at the two AoA considered, the most significant change occurred for noise generated by the canards, with an 8 to 10 dB drop in levels at the lower AoA.

6.1.11 Velocity Scaling for Far-Field Noise Levels

To determine an appropriate velocity scaling for far-field noise, medium-resolution simulations at additional speeds were performed for the Flap30-LGon (landing) and Flap0-LGoff (cruise) configurations. Unscaled integrated spectra for the Sum of all GLBC sources are shown in Figure 82 for both model configurations. For the quietest condition (cruise, Figure 82(b)), results for the two lowest



(a) Flap30-LGon (landing) (b) Flap0-LGoff (cruise)

Figure 82.—Unscaled integrated total noise spectra at different speeds for landing and cruise configurations (medium resolution).

speeds show flattening of the spectral roll-off at frequencies close to 10 kHz, suggesting possible contamination from numerical sources that cause SNR degradation.

For conventional subsonic transports, airframe noise levels typically follow an M^6 velocity scaling without the need to apply frequency or Strouhal (St) scaling. In Reference 45, based on single-microphone data, M^6 produced the best collapse for far-field total noise spectra. The synthetic array data allowed examination of individual airframe components. With M = 0.2 as the nominal value, the normalized spectra without and with St scaling for the Sum and two GLBC components are shown in Figure 83 for the Flap30-LGon configuration. Without St scaling (Figure 83(a)), total Sum spectra display good collapse of the noise levels at frequencies lower than 4 kHz. The application of St scaling produces good spectral collapse for the frequency range of 4 to 12 kHz and suboptimal collapse lower than 4 kHz (Figure 83(b)). Because the undercarriage used for the model is very rudimentary (composed of several simple bluff bodies), we suspect that a sizable portion of the noise generated by the gear stems from regular vortex shedding, which tends to follow a St normalization. Flap noise also collapses best with M^6 combined with St scaling up to 15 kHz, where adequate spatial resolution is maintained (Figure 83(e) and (f)).

6.1.12 Comparison With Semiempirical Models

System-level acoustic analyses of supersonic civil transports rely on existing semiempirical prediction models that were developed for conventional tube-and-wing subsonic aircraft (Ref. 53). As an initial attempt to validate the semiempirical models, a direct comparison between high-fidelity simulations and empirical predictions was performed. Figure 84 depicts these spectra at three polar directivity angles for a full-scale GLBC. To arrive at the full-scale spectra, the empirical Fink method within the NASA ANOPP noise prediction code (Ref. 10) was used to predict the model-scale sound pressure levels (SPL) for the GLBC airframe. The calculated SPL were then adjusted based on acoustic measurements of a model-scale supersonic civil transport. Details on these corrections are given in Reference 25 and documented in Reference 10. Model-scale frequencies were rescaled to full-scale values for both empirically predicted and high-fidelity simulation spectra.

As seen in Figure 84, the simulated spectra indicate that airframe noise is broadband in nature, with absolute peak levels occurring at relatively low frequencies (less than 300 Hz). They also display a rapid roll-off of the noise levels at frequencies greater than 2.5 kHz. The simulated spectra lack any significant directivity features. The fast roll-off of the high-frequency noise in the simulated spectra may be caused

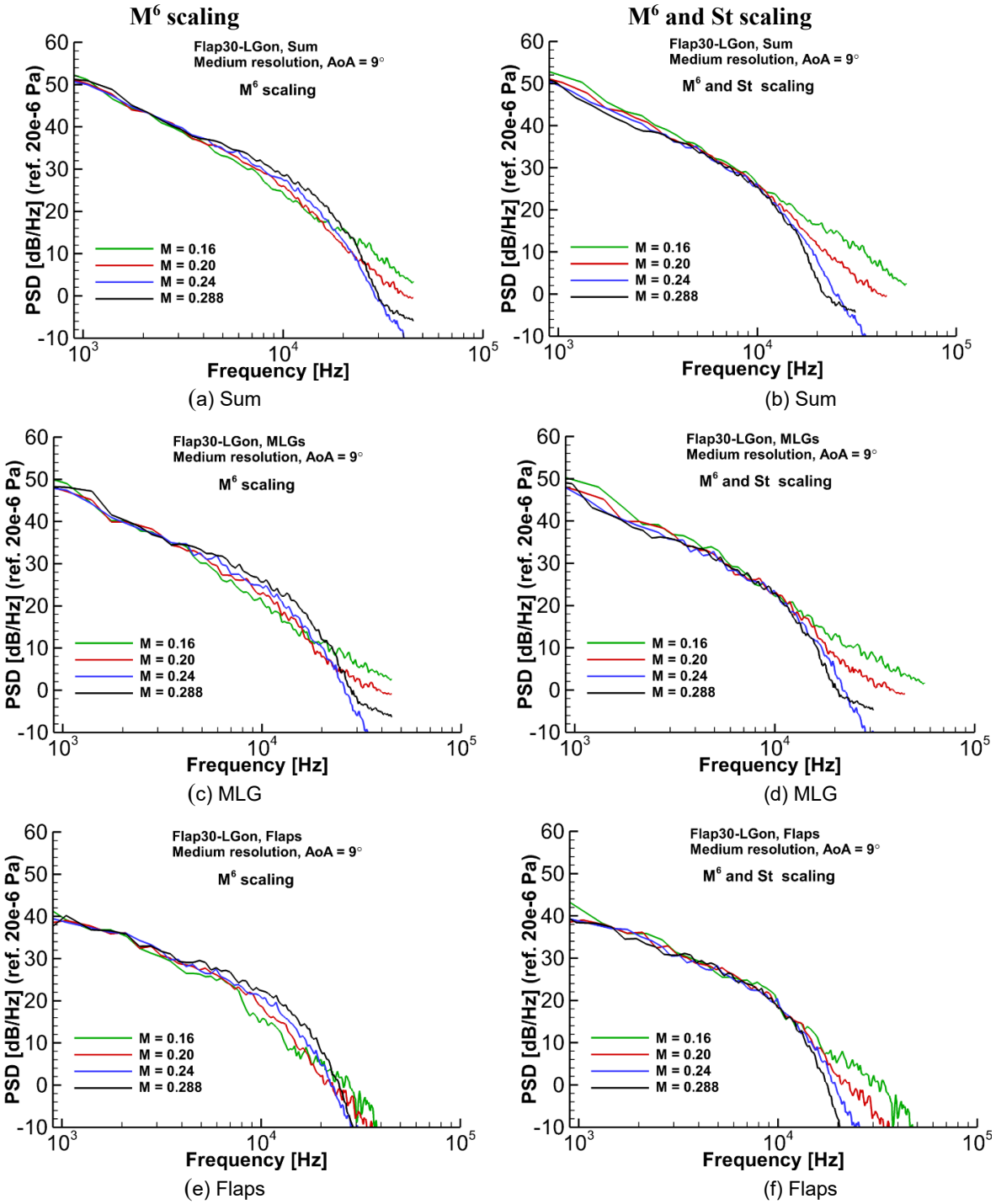


Figure 83.—Scaled integrated spectra for Flap30-LGon configuration (medium resolution)—landing gear and flaps.

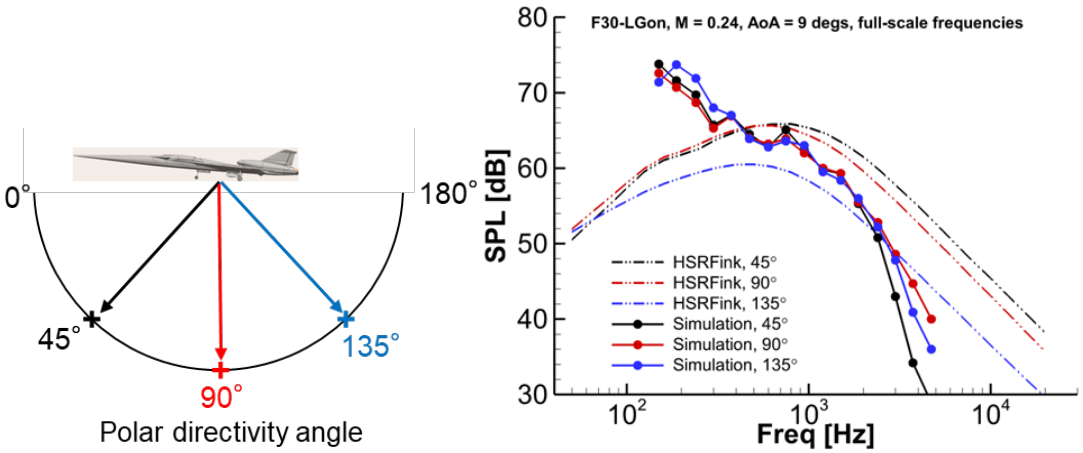


Figure 84.—Simulated and predicted spectra at three polar directivity angles and full-scale frequencies. Simulated values obtained from medium-resolution data.

by two distinct effects: insufficient spatio-temporal resolution at higher frequencies, and the absence of finer geometric details in the undercarriage that typically produce the high-frequency content of landing gear noise.

In contrast to the simulated results, ANOPP-predicted spectra (using HSRFink module) are broad and smooth, with the highest noise levels occurring at the forward and overhead directivity angles. Rearward noise is about 6 to 8 dB lower than that in the forward quadrant. The broad peak levels in the spectrum at 45° occur near 800 Hz and gradually shift to lower frequencies at higher polar angles. In general, acceptable agreement (in both shape and levels) between simulated and ANOPP-predicted spectra is observed within the 400 to 2500 Hz frequency range. The discrepancies observed between the two sets of data lower than 400 Hz are less important when A-weighting is applied during noise certification analysis. Based on the results presented in Figure 84, we can conclude that the empirical airframe noise models used to conduct system-level analyses of supersonic business jets yield far-field spectra with levels that are within ±5 dB of those from physics-based simulations over a good portion of the frequency range of interest.

7.0 Uncertainty Assessments

7.1 STCA-Based Total Aircraft Noise Uncertainty

The goal of the TC was to incorporate all the knowledge gained in reducing the fan and jet source noise uncertainty, described in the previous sections, into an aircraft system-level uncertainty assessment. The PUR effort was quantified through the resulting metrics from the system uncertainty assessments and tracked throughout the length of the entire TC. The focus of the PUR was in reducing epistemic uncertainty—which is model uncertainty due to lack of knowledge—rather than the aleatoric uncertainty, or uncertainty due to inherent randomness within data. To track the reduction of uncertainty, system-level noise assessments of the STCA aircraft model were performed four times throughout the life of the TC: an initial baseline assessment, update 1, update 2, and a final assessment.

The STCA total aircraft noise assessments were performed using NASA's ANOPP software in accordance with the modeling description detailed in Section 2.2 of this report. To capture the system-level uncertainty, both the jet noise source and inlet fan noise source were given randomized inputs rather than deterministic values that were propagated through the aircraft system model. These randomized inputs were defined as normal distributions characterized by an offset to the mean value and a standard

deviation around the mean value. The resulting system-level uncertainty was computed by running a Monte Carlo analysis, a method in which repeated random sampling of inputs (jet/fan source noise levels) are run through a deterministic model (ANOPP STCA model) to generate numerical uncertainty metrics for the outputs (STCA Airport EPNL). Randomly changing these variables represents the lack of knowledge of system characteristics, as well as the accuracy of (and uncertainty in) source noise prediction methods. For the system uncertainty assessments, the Monte Carlo contained 10,000 cases to adequately converge on an output EPNL standard deviation value and ensure stable histograms. The PUR progress indicator for the TC was this STCA-based total aircraft EPNL standard deviation. The initial benchmark value for the standard deviation was 7.8 EPNdB with a goal reduction of 5 EPNdB by the end of the TC. It should be noted that the uncertainty assessments only include uncertainty distributions for the jet, fan inlet tone, and fan inlet broadband noise sources and use deterministic values for all other noise sources (aft fan, core, landing gear, airframe). Including the uncertainty of these noise sources, although they are not the dominant noise sources at any of the three observer locations for the STCA, may impact the total aircraft system-level uncertainty.

7.2 Fan Noise Component Uncertainty Assessment

The fan noise component uncertainty of the system uncertainty assessment was determined through comparing the predictions of the two-stage fan empirical model (HDNFAN-2S) against available experimental data sets. Two data sets were utilized, the Quiet Supersonic Platform (QSP) data set and the GE High-Speed Fan (GE HSF) data set. The QSP data is from a two-stage fan tested with inlet guide vanes and was designed by Pratt & Whitney and tested in the GRC 9×15 LSWT in 2003. The GE HSF data is from experiments of a series of three single-stage fans and three stator sets designed and built by General Electric Aircraft Engines (GEAE) and tested as part of the NASA Advanced Subsonic Technology (AST) program in 1999. More details on these data sets and how they were used for the TC can be found in References 28 and 66. The HDNFAN-2S model was used as the prediction tool for the QSP data (two-stage fan) and the original HDNFAN methods within ANOPP were used at the prediction tool for the GE HSF data (single-stage fan). The total inlet fan source uncertainty was calculated by combining the results of both into a single standard deviation and offset value. A combined result from the GE HSF and QSP fan model was determined to be a reasonable method for an overall prediction uncertainty, because perhaps either a single- or two-stage fan might be chosen as the final design for an efficient and quiet supersonic aircraft engine.

For the initial STCA benchmark system uncertainty assessment, the inlet fan noise source uncertainty was calculated based on using the internal ANOPP HDNFAN methods for both the single-stage and two-stage fan predictions, prior to the development of the HDNFAN-2S model. These predictions were compared to the experimental values and the standard deviation and offset metrics were calculated for both broadband fan noise and tonal fan noise. Furthermore, the uncertainty metrics were separated based on flight condition (approach, flyover, lateral) to retain as much detail in the uncertainty as possible. The difference between predicted EPNL and experimental EPNL (dEPNL) is shown in Figure 85 for the various flight conditions and fan noise components.

Over the course of the TC, two interim updates (in October 2022 and October 2023) and a final update (in April 2024) of the SUA were performed and incorporated updated inlet fan source noise uncertainty metrics based on the empirical modeling improvements described in Section 4.4. The evolution of the inlet fan source noise uncertainty metrics can be seen in Table 11.

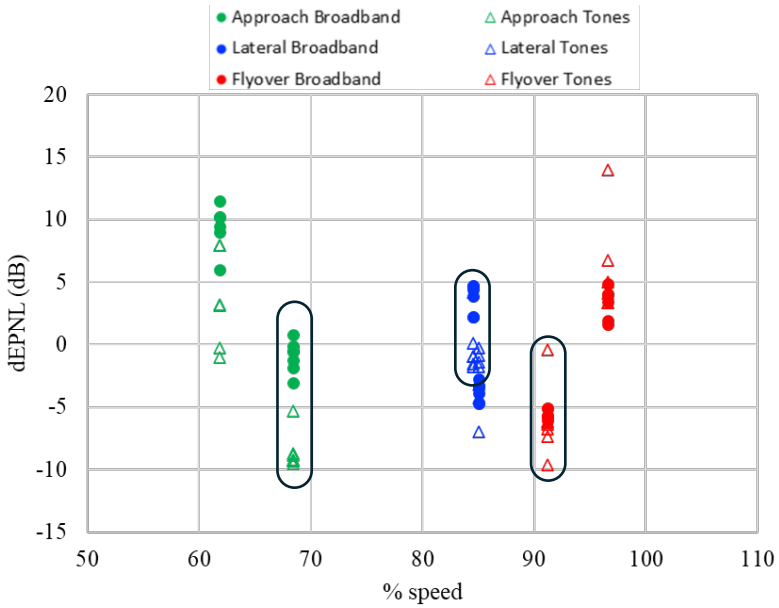


Figure 85.—Comparison of broadband (circle) and tone (triangle) dEPNL between model and test data for inlet fan noise; initial benchmark uncertainty assessment. QSP data identified by ellipses.

TABLE 11.—EVOLUTION OF INLET FAN NOISE UNCERTAINTY METRICS OVER TC

Variable	SUA Benchmark: May21		SUA Update I: Oct22		SUA Update II: Oct23		SUA Final: Apr24	
	Std. Dev.	Offset	Std. Dev.	Offset	Std. Dev.	Offset	Std. Dev.	Offset
Fan inlet tone (lateral)	7.13	0.49	6.82	0.00	6.19	0.49	4.36	2.67
Fan inlet tone (flyover)	2.55	1.52	3.41	2.06	3.42	2.57	2.72	0.33
Fan inlet tone (approach)	9.46	0.30	5.21	–4.38	5.54	–3.97	1.91	–1.14
Fan inlet BB (lateral)	4.71	1.48	2.03	–1.42	2.52	–0.96	2.06	–0.46
Fan inlet BB (flyover)	3.96	0.28	1.66	–2.28	2.13	–1.83	1.68	–1.26
Fan inlet BB (approach)	3.50	–1.11	2.76	–2.64	2.99	–2.20	2.62	–1.14

The first SUA update in October 2022 included the newly developed HDNFAN-2S empirical model for predicting the two-stage fan noise. The second SUA update in October 2023 included improvements to the HDNFAN-2S model by including the impact of acoustic treatment based on the GE TREAT method found in ANOPP. The final SUA assessment in April 2024 included the IGV-R1 spacing model in the HDNFAN-2S model and updated predictions for the single-stage GE HSF data that included the impact of swept rotors and swept/leaned stators. Updates for the single-stage predictions was done to reduce the total fan noise uncertainty metrics by implementing the effects of rotor/stator sweep and lean as discussed in Reference 101. It was found that the internal ANOPP HDNFAN methods do not account for rotor/stator sweep and lean and the GE HSF acoustic tests were done for various sweep and lean configurations. To capture the acoustic changes from the various configurations tested, a series of sweep and lean deltas, taken from Reference 24, were applied to the fan source spectra. This process helped align the single-stage fan predictions to the GE HSF experimental data. It is noted that this is a potential knowledge gap in predicting fan noise (for both subsonic and supersonic fans) at the conceptual level and could be investigated further in the future. The final SUA dEPNL values for the inlet fan noise source are shown in Figure 86. Comparing to Figure 85, a substantial improvement in predicting inlet fan noise was

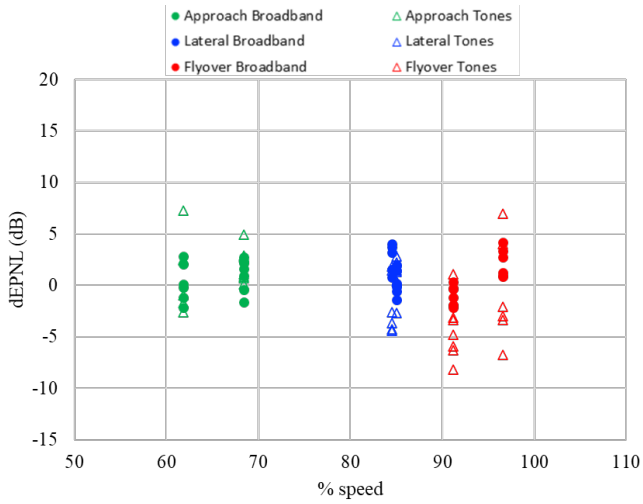


Figure 86.—Comparison of broadband (circle) and tone (triangle) dEPNL between model and test data for inlet fan noise; final uncertainty assessment.

achieved over the course of the TC. The new empirical models to predict inlet fan noise show great promise in capturing the noise from fans designed for supersonic applications. The impact on the overall STCA aircraft system-level uncertainty metrics will be discussed in Section 7.4. More details on the new fan noise model for two-stage fans are in Reference 102.

7.3 Jet Noise Component Uncertainty Assessment

Engine exhaust flow conditions of near-term civil supersonic aircraft will likely follow conventional throttle conditions in their pressure and temperature relationships but with nozzle pressure ratios possibly exceeding 2.0. For nozzle geometry, they might have internal plugs with flaps and seals to vary the nozzle areas for supersonic flight or they might have a translating external plug to make the area adjustments. They would most likely use an internal mixer and a common flow duct. The data set being used in the uncertainty assessment should cover this range of conditions and geometries. For external plug nozzles, the only noise data available was from the Plug20 test (Ref. 83). This test had an internal lobed mixer and included variations in plug and nozzle length. Thirty-two points covering throttle lines with $1.5 < NPR < 2.3$ were included in the assessment exercises. For internal plug nozzles, the Plug20 test did have one internal plug configuration, but these 8 points were augmented by 45 data points from a 2010 test (Ref. 98) of a single-stream nozzle, which covered a range of flows and flight speeds representative of near-term supersonic aircraft. The combined range of flow conditions is shown in Figure 87.

In the initial comparison of model versus data, conducted in February of 2021, the difference in component EPNL was banded between single-stream hot jets and internally mixed, dual-stream jets, as seen in Figure 88. Both the Stone and SGLJET jet noise models in ANOPP have a bias for high-speed hot jets, which produced a high dEPNL for the single-stream cases. Neither model is intended for internally mixed nozzles, which are very different from the separate flow nozzles that the Stone model does include. The internally mixed nozzle data was predicted first using the assumption that it was a separate flow nozzle and then using the approximation that the noise was that of a fully mixed single-stream jet. The latter approximation had less error and was used in the uncertainty assessment. The difference between predicted EPNL and dEPNL is shown in Figure 88. The spread in the discrepancies shown in the figure are quantified in the SUA Benchmark column of Table 12.

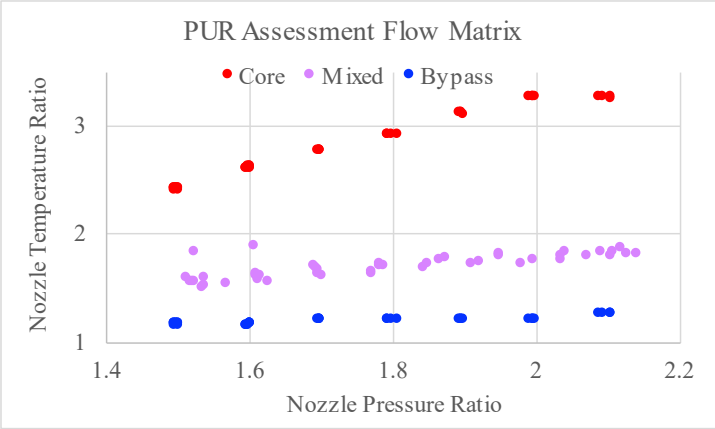


Figure 87.—Matrix of flow conditions contained in jet-noise assessment database.

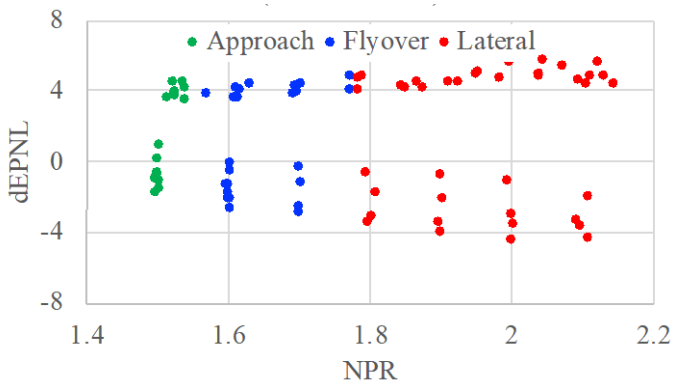


Figure 88.—Comparison of jet-noise component dEPNL between model and test data as function of nozzle pressure ratio (NPR). SUA Benchmark (2021) uncertainty assessment.

TABLE 12.—EVOLUTION OF JET-NOISE UNCERTAINTY METRICS OVER TC

Variable	SUA Benchmark: Feb 21		SUA Update I: Oct 22		SUA Update II: Oct 23		SUA Final: Apr 24	
	Std. Dev.	Offset	Std. Dev.	Offset	Std. Dev.	Offset	Std. Dev.	Offset
Jet noise (lateral)	3.85	–1.68	1.13	1.50	1.00	–1.01	0.75	–0.67
Jet noise (flyover)	2.92	–1.47	1.13	1.17	0.73	–0.29	0.34	–0.23
Jet noise (approach)	1.74	–1.61	1.05	1.29	0.78	–0.45	0.45	–0.36

The improvements in the jet noise modeling occurred in two steps. The first step was to substitute the basic jet mixing noise prediction models in ANOPP with one developed at NASA Glenn in 2009 (Refs. 97 and 103). Referred to as "sJet," this code is suitable for single-stream hot jets only. It predicts jet noise spectrum by interpolating over a few experimental spectral directivity data sets using scaling laws determined from data acquired over decades of research at NASA Glenn's Small Hot Jet Acoustic Rig (SHJAR). This model is more faithful to modern jet noise data sets and gave an immediate improvement when the first SUA update was performed in 2022 as seen in the SUA Update I column of Table 12.

As the noise associated with lobed mixers became better understood, an empirical model was developed for it using historical data from internally mixed nozzles, described in Section 5.5. This model went through several iterations, reducing the deviation between the PUR test database and the model. By the end of the TC, the last version of the combined internal mixer and jet mixing noise model, called

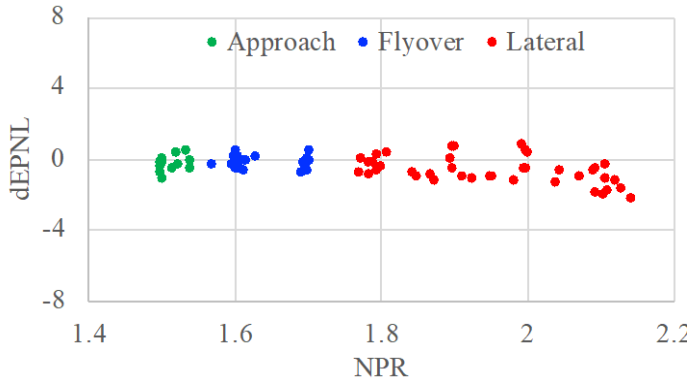


Figure 89.—Comparison of jet noise component dEPNL between model and test data as function of nozzle pressure ratio (NPR). SUA Final (2024) uncertainty assessment.

sJetMod24, did a good job of representing all the configurations and flows in the test database, covering the exhaust configurations and flows of a near-term supersonic aircraft. Figure 89 shows the deviations between empirical model and experimental data, which can be compared to the original spread in Figure 88. The SUA Final column of Table 12 quantifies the improvement in model performance.

7.4 Evolution of Total Aircraft Uncertainty

The PUR progress indicator for the STCA system uncertainty assessments was tracked throughout the course of the TC to monitor the progress in reducing the STCA aircraft system-level uncertainty. The metric used in tracking the total aircraft noise uncertainty was the standard deviation of the LTO cumulative EPNL. The cumulative EPNL is a summation of the EPNL at the three observer locations for aircraft noise certification, approach, flyover, and lateral. The initial benchmark uncertainty assessments for the conventional subsonic 737-800 model and the STCA model, preformed in May 2021, resulted in a cumulative EPNL standard deviation of 1.5 and 7.8 EPNdB, respectively. The goal of the TC was to reduce the STCA EPNL standard deviation by 5EPNdB by the end of the period of performance. Intermediate updates to the SUA were performed over the course of the TC and incrementally incorporated improvements to the jet and fan source noise empirical models based on the research of the investigative team.

The first SUA update occurred in October 2022 and included significant updates to both the fan and jet empirical models. The jet noise empirical model (sJetMod22) was developed to predict jet noise from internally mixed, external plug nozzles, not present in existing jet source noise models. The initial two-stage fan empirical model, HDNFAN-2S, was developed and utilized in the first SUA update instead of the heritage ANOPP HDNFAN models. The major changes in the empirical predictions of jet and fan noise resulted in a large reduction in aircraft system-level uncertainty, reducing the 7.8 EPNdB standard deviation to 3.4 EPNdB (a 4.4 EPNdB reduction from the benchmark value). The second SUA update occurred in October of 2023 and included substantial improvements to the jet and fan empirical models. The jet empirical model updates included updates based on the information gained from the LES analyses of the plug nozzle experimental designs, focused primarily on changes to plug-dependence in the sJetMod22 model. The fan empirical model updates included the addition of an acoustic treatment model, based on the ANOPP GE TREAT method, to capture the impact of liner attenuation on the two-stage fan noise source. These incremental improvements to the empirical models resulted in a SUA standard deviation value of 2.9 EPNdB (a 4.9 EPNdB reduction from the benchmark value).

The final SUA occurred in April 2024 and was the culmination of all the improvements made to the jet and fan empirical models over the course of the TC. Improvements to the empirical jet noise model from SUA update 2 included a two-component model based on new understandings of noise source mechanisms, guided by jet LES analyses that captured more details of the internal mixer impact on jet noise. The jet model also included a new spectral model of internal noise sources coupling with nozzle duct modes for internal mixers and plug geometries. Improvements to the empirical fan noise model from SUA update 2 included the inclusion of an IGV-R1 spacing model based on the SuperFan simulations. The final SUA resulted in a final EPNL standard deviation value of 2.0 EPNdB (a 5.8 EPNdB reduction from the benchmark value) and achieved the goal of meeting a 5 EPNdB reduction in the PUR progress indicator. In fact, it exceeded the PUR TC goal by 0.8 EPNdB. The final SUA Monte Carlo analysis used to generate the standard deviation metric consisted of 10,000 cases and the convergence of the statistical metrics is shown in Figure 90. The resulting probability distribution function of the STCA Cumulative EPNL is shown in Figure 91. A tracking of the PUR progress indicator relative to the goal over the course of the TC is shown in Figure 92.

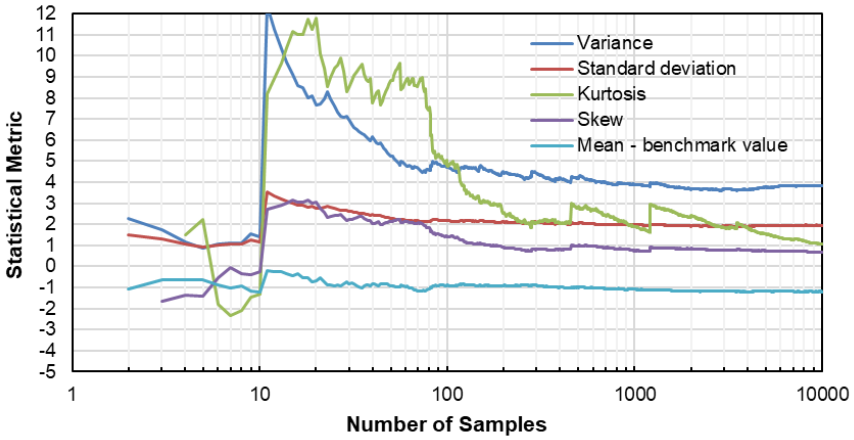


Figure 90.—Final STCA SUA Monte Carlo statistical metrics.

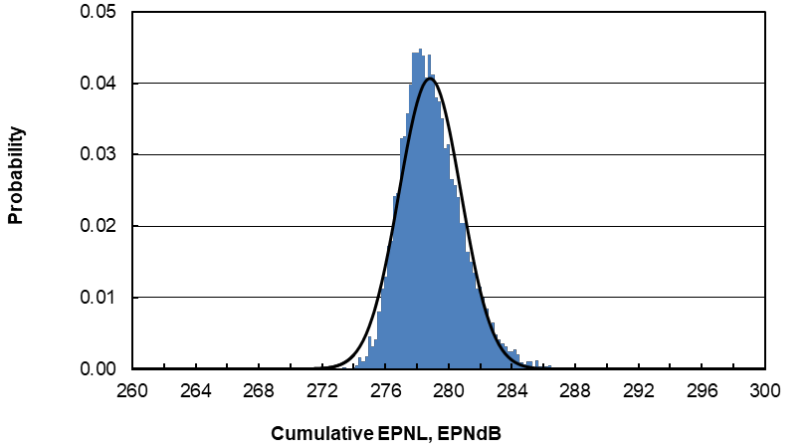


Figure 91.—Final STCA SUA probability distribution function.

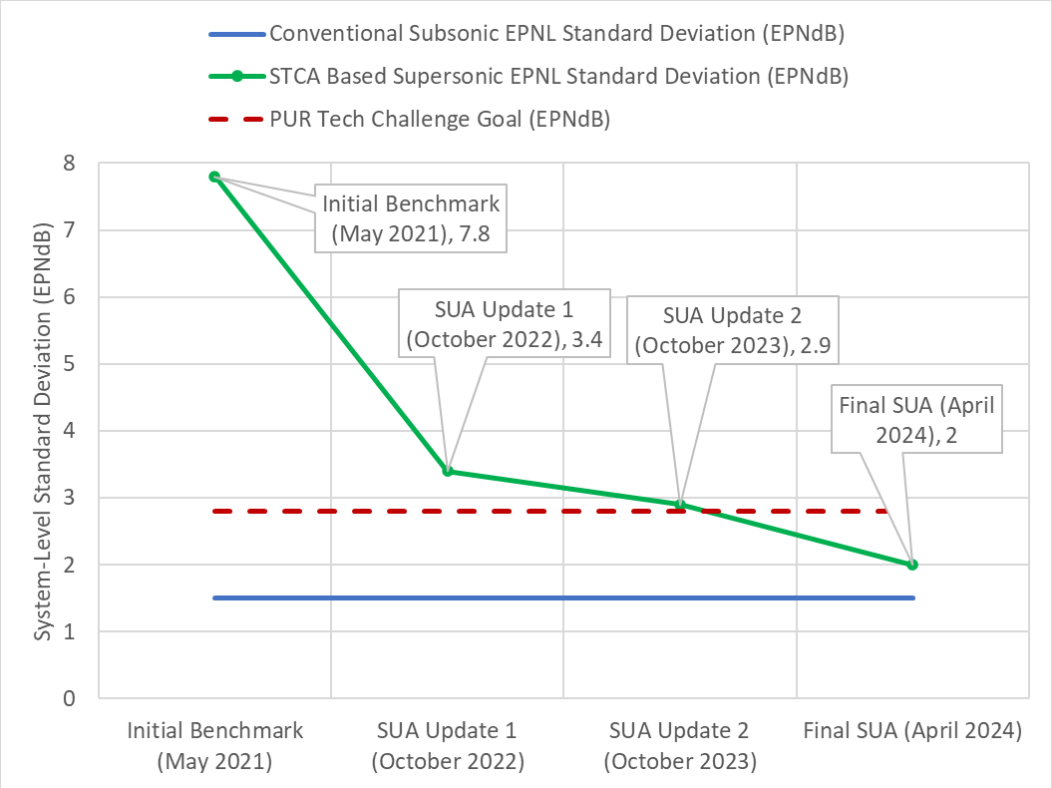


Figure 92.—Evolution of PUR progress indicator relative to TC goal.

8.0 Knowledge Gaps Identified

8.1 Aft Fan Noise Simulations

We have been neglecting the aft fan noise because the aft noise has historically been expected to be jet dominated. This may not be true for lower flight speeds or with advanced nozzle installations. The aft fan noise is a dominant source for subsonic fan noise at some flight conditions and shaft speeds. The aft noise is always more complicated due to a sheared flow. Additionally, the supersonic engine will likely include a long bypass duct with a mixed flow nozzle. It is not known if anyone has ever experimented or simulated this configuration.

8.2 Broadband Fan Noise Modeling

In the PUR TC, the leading source of fan noise was simulated and modeled: inlet tone noise. Broadband inlet noise is not as amenable to direct simulation as tone noise is. Its source is more robust than the tone source, making statistical models, such as acoustic analogies, more tractable. However, the propagation of broadband sound through the multiple stages of the rotor-stator system and the supersonic inlet should be investigated and the models for inlet broadband noise should be enhanced. The Actran portion of the fan noise simulation toolchain should be applied to produce the custom Green's functions required to predict this propagation.

8.3 Empirical Fan Noise Shielding Models

A commonly heard idea for noise reduction in supersonic aircraft is to integrate the propulsion such that the inlet is above the delta-wing, shielding the ground observer from the noise coming from the inlet. Indeed, the empirical models currently being used predict very strong reduction in fan noise. However, detailed studies of advanced concepts of subsonic aircraft designed to achieve shielding have found that the empirical models are very optimistic when predicting noise reduction. High-fidelity prediction methods should be deployed on supersonic configurations with inlets located over a range of possible locations. The results can be used to create more realistic models for shielding of inlet fan noise for system-level studies.

8.4 Acoustic Liners in Hot, High-Speed Flows

For both fan and internal shear layer noise sources, liners would be a useful noise reduction technology in the hot section of an internally mixed exhaust system. The technology for creating acoustic liners generally exists; what is missing is the ability to predict the effective impedance of the liner for acoustic waves propagating down the duct. The combination of grazing flow and variable speeds of sound make the design of the liners difficult and their acoustic impact hard to predict. High-fidelity simulations could produce the data and insights required to make lower-order models of liners in hot flow possible.

8.5 Improve LES of Internal Noise Sources

The inability of LES to reproduce the noise spectra from the Plug20 tests must be resolved. Whether the issue is some aspect of the experiment that is being mistakenly disregarded in the simulation setup or a numerical shortcoming, LES should be able to reproduce the noise produced if it is to replace physical testing. Historically, complicated exhaust systems have produced unexpected noise when tested. Often, this appeared as a tone representing a resonant unsteadiness in the flow. Other times, the unexpected noise was an increase in high frequencies, often described as broadband amplification. This has been observed in simple jets when the shear layer was deliberately fed energy at frequencies near its most amplified instability. The increase in turbulent energy associated with the coherent structures produced by the excitation pumps energy into other scales via classic turbulent cascade, typically creating additional noise at higher frequencies than the excitation. Whatever the mechanism of noise production, LES should be able to reproduce both the shear layer instabilities and the pressure field feedback that create these acoustic sources that do not simply correlate with the turbulence predicted by steady RANS solutions.

8.6 Improve LES for Shock Noise

During the validation of single-stream jets, one flow with supersonic (relative to its own speed of sound) jet was simulated. The simulation did not capture the noise of the broadband shock as well as it did the rest of the jet noise. Because it is unlikely that a jet containing shocks will be quiet enough for commercial airport operation, this was not considered important at the time. However, exhaust systems with external plugs do have shocks in subcritical flow conditions from the acceleration of the flow over the crown of the plug. Therefore, it is important that the LES methods being used for supersonic propulsion do properly capture the shock and the noise associated with it. Supersonic jets with significant broadband shock noise should be investigated, starting with the most basic single-stream jet possible.

8.7 More Efficient LES Methods

As LES have become more capable and computational resources have become more powerful, the difficulty in creating efficient grids has become more important to adoption of the method by engineers. Indeed, it is foreseeable that LES may replace RANS codes as the main tool for fluids simulation but only if grid generation can be become easy for realistic geometries. To this end, numerical methods must be pursued that lower the expertise required to create grids appropriate for full-spectrum time-resolved simulations. Two methods currently show promise to reduce grid generation difficulties and improve numerical efficiency: Voronoi meshes with unstructured solvers, and immersed boundary geometries with structured solvers. The internal mixer problem would benefit from either of these techniques and they should continue to be developed using the internal mixed exhaust system as a benchmark problem. Currently, both methods are matching noise predictions of the method of overset grid with structured solver that has been used in the PUR TC, showing the immediate payoff from the development of these new methods once the underlying issues with LES have been identified and corrected.

8.8 Expand Cycle Range (BPR) of Jet Noise Models

One significant parameter in the jet noise modeling that was not adequately explored was the effect of bypass ratio. The historical data that served as the basis for the modeling was all acquired at bypass ratios between 4 and 6. The Plug20 data that supplemented the historical data likewise had bypass ratio around 4.5. Although there was not a strong effect of bypass ratio over this range, it is possible, even likely, that there will be more sensitivity at lower bypass ratios where engines for supersonic vehicles are currently envisioned. In future tests to diagnose why LES and experiments disagree, tests should also be conducted with models having lower bypass ratios to be sure that the current noise models will continue to work well in those relevant regimes.

8.9 Explore Porous Plug, Nozzle Concepts

In addition to preliminary explorations of the acoustic impact of plug shape (discussed in Section 3.2.2) porous plugs were also considered. Porous plugs have been explored previously, but insight into how they work and under what conditions was lacking. The most obvious impact is to soften or remove shocks on the plug from an underexpanded flow, shocks that lead to broadband shock noise (BBSN) and screech tones. Most dramatic was the finding for the 10° plug. Not only were BBSN and screech tones taken out by the porous version of the plug (as shown in Figure 93), it was also found that transonic tones as well as excess broadband noise (EBBN) were also suppressed by porosity when the plug was used with an extended cowl, such as would be appropriate for cruise. The point of looking at noise in the cruise configuration, which is overexpanded when run at LTO condition, is that if the nozzle did not have to change geometry between LTO and cruise, there would be a great savings in weight and complexity. Unfortunately, the 10° conic plug is rather long for application, and the shorter 16° conic plug exhibited little effect when a porous version was tried. The reasons for these conflicting effects remain far from being understood and should be explored.

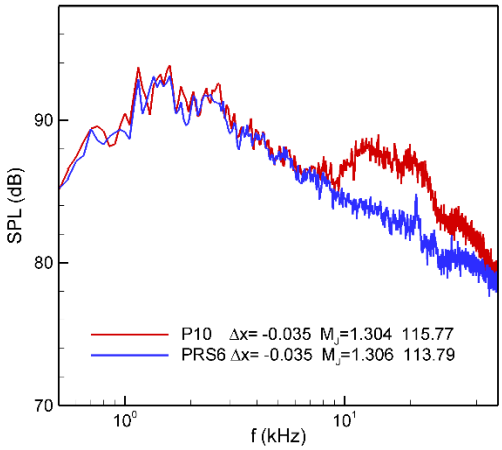


Figure 93.—Sound pressure level (SPL) spectra at θ≈90° for 10° conic plug showing plug porosity effect. Red lines: solid plug (P10), blue lines: porous plug (PRS6).

8.10 Airframe Noise From Supersonic Configurations

The strongest sources of airframe noise in conventional aircraft are largely missing from simplistic supersonic concept aircraft. Without high-lift devices such as slats and flaps, the delta-wing is relatively quiet and the landing gear are the main contributors to airframe noise. As noted in Section 6.1.1, current estimates for airframe noise are based entirely upon a few tests of an HSCT-era configuration. Although current models indicate that airframe noise will likely dominate propulsion noise, this is based on thin evidence, bolstered here only in that the models predicted the noise of the X-59 aircraft reasonably well. Further, airspeeds are likely to be higher than conventional aircraft LTO operation, decreasing the jet noise while increasing the airframe noise. This all points to the need to find ways to improve models for airframe noise of supersonic aircraft, starting with having more fidelity in our concept vehicles as they operate at low speed.

8.11 Low-Noise Operations

Although much research has focused on the prediction and reduction of noise sources found in supersonic aircraft, the PUR TC did highlight the impact of trajectory and variable noise reduction scheduling of propulsion on the noise levels of the certification procedure. The airspeed impacts noise source levels and the distance to the observer and the duration of the noise directly impacts the EPNL metric used in certification. With the advent of variable noise reduction systems, most likely implemented as automatic changes in throttle and wing flap deflection, being allowed in certification, these variables must be explored as an additional means to alleviate the noise impact to the community.

9.0 Summary of Results

The Prediction Uncertainty Reduction Technical Challenge (PUR TC) was initiated in January 2021 in response to a perceived need to improve predictions of noise generated by future civilian supersonic aircraft at landing and takeoff. In baseline activities, it was found that commonly used empirical prediction methods had an uncertainty of 1.5 EPNdB for conventional aircraft. In comparison, the uncertainty was 7.8 EPNdB when these methods were applied to a near-term supersonic vehicle. The goal

of the PUR TC was to reduce the uncertainty for the supersonic aircraft by 5 EPNdB. This was to be done by obtaining noise data for supersonic-specific aircraft configurations using physics-based numerical simulations and improving the empirical methods used in the noise predictions.

To meet the TC objectives, high-fidelity designs had to be developed for the noise-generating portions of a supersonic aircraft. Workflows of physics-based simulation methods for aircraft noise had to be created and quantified. The simulations had to be applied to the high-fidelity designs and analyzed to confirm their reliability. In some cases, the simulations had to be supplemented with limited experimental data to provide the insights required as empirical models for the component noise sources were developed. And finally, the new empirical noise methods had to be evaluated against limited physical experimental data to assess the uncertainty of prediction of noise from the full aircraft.

Over three years, a team of NASA researchers carried out the tasks just outlined, building up capabilities, and carrying out simulations and analyzing results to build the new noise prediction methods and assess their uncertainties. By the end of the TC in April 2024, the new noise models were assessed and the uncertainty in predicting noise of supersonic aircraft was found to be 2.0 EPNdB. This not only met the goal of the TC, it put the prediction of landing and takeoff noise for supersonic vehicles near that expected for conventional aircraft.

This report serves as a guide to the activities that led to the accomplishment of the TC goal. The references herein can be consulted for details about the technologies that were advanced, the insights that were gained, and the actual empirical methods developed.

Appendix A.—Acronyms and Abbreviations

2D	two-dimensional
2DOF	two degrees of freedom
3D	three-dimensional
AAPL	Aero-Acoustic Propulsion Lab
ADP	Advanced Ducted Propulsor
ANOPP	Aircraft Noise Prediction Program
AoA	angle of attack
ARC	Ames Research Center
ASME	American Society Of Mechanical Engineers
BBSN	broadband shock noise
BPF	blade passing frequency
BPR	bypass ratio
CAA	computational aero acoustics
CAD	computer-aided design
CAEP	Committee on Aviation Environmental Protection
CFD	computational fluid dynamics
CGNS	CFD General Notation System
CST	Commercial Supersonic Technology
DARPA	Defense Advanced Research Projects Agency
DDES	delayed detached eddy simulation
dEPNL	experimental effective perceived noise level
DES	detached eddy simulation
Djet	nozzle exit diameter
EPNdb	effective perceived noise in decibels
EPNL	effective perceived noise level
EPNLdb	effective perceived noise level in decibels
FAA	Federal Aviation Administration
FAR	Federal Acquisition Regulations
FLOPS	Flight Optimization System
FWH	Ffowcs Williams-Hawkings
GE	General Electric
GEAN	GE Aircraft Engines
GLBC	generic low boom concept
GRC	Glenn Research Center
HDNFAN	ANOPP fan noise model
HFJER	High-Flow Jet Exit Rig
HSCT	High Speed Civil Transport
HSR	High Speed Research
ICAO	International Civil Aviation Organization
IGV	inlet guide vanes
klb	kilo-pounds
LAVA	Launch Ascent and Vehicle Aerodynamics
LE	leading edge
LES	large-eddy simulation

LSAF	Low-Speed Anechoic Facility
LTO	landing and takeoff
M	Mach number
MLG	main landing gear
MoC	method of characteristics
NLG	nose landing gear
NLH	nonlinear harmonic
NPR	nozzle pressure ratio
NPSS	Numerical Propulsion System Simulation
NTR	nozzle temperature ratio
OASPL	overall sound pressure level
PDF	probability distribution function
PNL	perceived noise level
PNLT	tone-corrected PNL
PSD	power spectral density
PUR	Prediction Uncertainty Reduction
PWL	sound power level
QSP	Quiet Supersonic Propulsor
R1	rotor 1
RANS	Reynold-Averaged Navier-Stokes
S1	stator 1
SDOF	single degree of freedom
SDT	Source Diagnostic Test
SEM	standard error of the mean
SNR	signal-to-noise ratio
SPAND	Supersonic Parametric Nozzle Design
SPL	sound pressure level
SPPV	single-plane, pressure velocity
STCA	Supersonic Technology Concept Aeroplane
SUA	system uncertainty assessment
SUPIN	Supersonic Inlet Prediction Program
t	metric ton
TC	Technical Challenge
TE	trailing edge
TKE	turbulent kinetic energy
TREAT	ANOPP liner model
TTT	Transformational Tools and Technologies
URANS	unsteady RANS
VNRS	variable noise reduction system
V	velocity
WMLES	wall-modeled LES
ZDES	zonal detached eddy simulation

References

1. J. Bridges, “Results of the NASA Prediction Uncertainty Reduction Tech Challenge,” in AIAA SciTech Forum 2025, American Institute of Aeronautics and Astronautics, 2025.
2. H.R. Welge et al., “N plus 2 Supersonic Concept Development and Systems Integration,” Aug. 2010. Accessed: May 01, 2017. [Online]. Available: https://ntrs.nasa.gov/search.jsp?R=20100030607
3. H.R. Welge et al., “N plus 3 Advanced Concept Studies for Supersonic Commercial Transport Aircraft Entering Service in the 2030-2035 Period,” Apr. 2011. Accessed: May 01, 2017. [Online]. Available: https://ntrs.nasa.gov/search.jsp?R=20110010973
4. J. Morgenstern, N. Norstrud, J. Sokhey, S. Martens, and J. J. Alonso, “Advanced Concept Studies for Supersonic Commercial Transports Entering Service in the 2018 to 2020 Period,” Feb. 2013. Accessed: May 01, 2017. [Online]. Available: https://ntrs.nasa.gov/search.jsp?R=20130010174
5. J. Morgenstern et al., “Advanced Concept Studies for Supersonic Commercial Transports Entering Service in the 2018-2020 Period Phase 2,” GRC-E-DAA-TN20996, Jul. 2015. Accessed: Dec. 20, 2021. [Online]. Available: https://ntrs.nasa.gov/citations/20150015837
6. Ramakrishnan, Kishore et al., “Evaluation of Low Noise Integration Concepts and Propulsion Technologies for Future Supersonic Civil Transports,” NASA Contractor Report NASA CR-2018-219936. [Online]. Available: https://ntrs.nasa.gov/CR-2018-219936
7. C. Heath, J. Seidel, and S.K. Rallabhandi, “Viscous Aerodynamic Shape Optimization with Installed Propulsion Effects,” in 35th AIAA Applied Aerodynamics Conference, Denver, Colorado: American Institute of Aeronautics and Astronautics, Jun. 2017. doi: 10.2514/6.2017-3046.
8. V.F. Dippold, “High Speed Inlet Distortion Test for the X 59 Low Boom Flight Demonstrator in the NASA Glenn 8-by 6-Foot Supersonic Wind Tunnel,” E-20056, Jul. 2022. Accessed: May 10, 2024. [Online]. Available: https://ntrs.nasa.gov/citations/20220010443
9. FAA Advisory Circular 36-4C, “Noise Standards: Aircraft Type And Airworthiness Certification (36-4C),” in FAA Advisory Circular, 2003.
10. R. Golub, J.W. Rawls, and J.C. Yeager, “High Speed Research Noise Prediction Code (HSRNOISE) User’s and Theoretical Manual,” NASA/CR-2004-213014, Nov. 2004. Accessed: Dec. 21, 2021. [Online]. Available: https://ntrs.nasa.gov/citations/20040200978
11. W. Ng, “Comparison of the Aeroacoustics of Two Small-Scale Supersonic Inlets,” NASA/CR-96-206507, Jan. 1996. Accessed: May 10, 2024. [Online]. Available: https://ntrs.nasa.gov/citations/19980006073
12. S.-M. Li, C.A. Hanuska, and W.F. Ng, “AN EXPERIMENTAL INVESTIGATION OF THE AEROACOUSTICS OF A TWO-DIMENSIONAL BIFURCATED SUPERSONIC INLET,” Journal of Sound and Vibration, vol. 248, no. 1, pp. 105–121, Nov. 2001, doi: 10.1006/jsvi.2001.3731.
13. D. Stephens, C.J. Miller, P.E. Slaboch, J. Brown, and J.M. Celestina, “Supersonic Engine Inlet Tone Noise Radiation,” in 25th AIAA/CEAS Aeroacoustics Conference, Delft, The Netherlands: American Institute of Aeronautics and Astronautics, May 2019. doi: 10.2514/6.2019-2493.
14. R.J. Neubert and C.P. Gendrich, “HSCT Forward Swept Fan Performance,” presented at the ASME Turbo Expo 2003, collocated with the 2003 International Joint Power Generation Conference, American Society of Mechanical Engineers Digital Collection, Feb. 2009, pp. 625–631. doi: 10.1115/GT2003-38948.
15. J.J. Berton, “Aircraft Noise and Performance Data for a Notional Supersonic Business Jet,” in 28th AIAA/CEAS Aeroacoustics 2022 Conference, American Institute of Aeronautics and Astronautics. doi: 10.2514/6.2022-3078.

16. R.W. Claus, A.L. Evans, J.K. Lylte, and L.D. Nichols, “Numerical Propulsion System Simulation,” Computing Systems in Engineering, vol. 2, no. 4, pp. 357–364, Jan. 1991, doi: 10.1016/0956-0521(91)90003-N.
17. SWRI, “Numerical Propulsion System Simulation (NPSS) ver. 1.6.5,” Southwest Research Institute. Accessed: Dec. 21, 2021. [Online]. Available: https://www.swri.org/consortia/numerical-propulsion-system-simulation-npss
18. J. Gloudemans, P. Davis, and P. Gelhausen, “A rapid geometry modeler for conceptual aircraft,” in 34th Aerospace Sciences Meeting and Exhibit, Reno, NV, U.S.A.: American Institute of Aeronautics and Astronautics, Jan. 1996. doi: 10.2514/6.1996-52.
19. H.W. Carlson, J. Chu, L.P. Ozoroski, and L.A. McCullers, “Guide to AERO2S and WINGDES Computer Codes for Prediction and Minimization of Drag Due to Lift.” Nov. 01, 1997. Accessed: May 14, 2024. [Online]. Available: https://ntrs.nasa.gov/citations/19980003445
20. S.C. Sommer and B.J. Short, “FREE-FLIGlIT MEASUREMENTS OF TURBULENT-BOUNDARY-LAYER SKIN FRICTION IN THE PRESENCE OF SEVERE AERODYNAMIC HEATING AT MACH NUMBERS FROM 2.8 TO 7.0”.
21. D.P. Wells, B.L. Horvath, and L.A. McCullers, “The Flight Optimization System Weights Estimation Method,” NASA/TM-2017-219627/VOL1, Jun. 2017. Accessed: May 14, 2024. [Online]. Available: https://ntrs.nasa.gov/citations/20170005851
22. R.E. Gillian, “Aircraft noise prediction program user’s manual,” in NASA-TM-84486, in NASA Technical Memo, 1982. Accessed: Dec. 19, 2017. [Online]. Available: https://ntrs.nasa.gov/search.jsp?R=19830007879
23. K.B. Kontos, B.A. Janardan, and P.R. Gliebe, “Improved NASA-ANOPP Noise Prediction Computer Code for Advanced Subsonic Propulsion Systems,” NASA-CR-195480, Aug. 1996. Accessed: Dec. 21, 2021. [Online]. Available: https://ntrs.nasa.gov/citations/19960048499
24. M.R. Fink, “Airframe Noise Prediction Method,” UNITED TECHNOLOGIES RESEARCH CENTER EAST HARTFORD CT, UTRC/R77-912607-11, Mar. 1977. Accessed: Dec. 19, 2017. [Online]. Available: http://www.dtic.mil/docs/citations/ADA039664
25. W.H. Herkes and R.W. Stoker, “Wind Tunnel Measurements of the Airframe Noise of a High-speed Civil Transport,” in 36th Aerospace Sciences Meeting & Exhibit, American Institute of Aeronautics and Astronautics, 1998. [Online]. Available: https://arc.aiaa.org/doi/pdfplus/10.2514/6.1998-472
26. International Civil Aviation Organization, Annex 16 - Environmental Protection - Volume I - Aircraft Noise | ICAO Store. Accessed: May 14, 2024. [Online]. Available: https://store.icao.int/en/annex-16-environmental-protection-volume-i-aircraft-noise
27. J.J. Berton, “Simultaneous Use of Ground Reflection and Lateral Attenuation Noise Models,” Journal of Aircraft, vol. 59, no. 2, pp. 536–543, Mar. 2022, doi: 10.2514/1.C036488.
28. J.E. Bridges, D. Stephens, and J.J. Berton, “Quantifying Uncertainty of Landing and Takeoff Noise for Commercial Supersonic Aircraft,” in 28th AIAA/CEAS Aeroacoustics 2022 Conference, American Institute of Aeronautics and Astronautics, 2022. doi: 10.2514/6.2022-3051.
29. J.W. Slater, “SUPIN: A Computational Tool for Supersonic Inlet Design,” in 54th AIAA Aerospace Sciences Meeting, San Diego, California, USA: American Institute of Aeronautics and Astronautics, Jan. 2016. doi: 10.2514/6.2016-0530.
30. K.B.M.Q. Zaman and B.C. Heberling, “A Study of Flow and Noise from Supersonic Plug Nozzles,” in 2021 AIAA Aviation Forum, American Institute of Aeronautics and Astronautics, 2021.
31. J.H. Korth, “Optimization of Plug Nozzles Using CFD Informed Design Space Querying,” in AIAA SCITECH 2024 Forum, American Institute of Aeronautics and Astronautics, 2024. doi: 10.2514/6.2024-1776.

32. W.V. Banks, “Optimization of a Parametric Lobe Mixer for Internally Mixed Nozzles,” in AIAA AVIATION 2022 Forum, American Institute of Aeronautics and Astronautics, 2022. doi: 10.2514/6.2022-3261.
33. W.V. Banks, “Advanced Parametric Lobe Mixer Concepts for Internally Mixed Nozzles,” in AIAA AVIATION 2023 Forum, American Institute of Aeronautics and Astronautics, 2023. doi: 10.2514/6.2023-3469.
34. K.Q. Zaman and B. Heberling, “A study of flow and noise from supersonic plug nozzles,” in AIAA AVIATION 2021 FORUM, American Institute of Aeronautics and Astronautics. doi: 10.2514/6.2021-2304.
35. K.Q. Zaman and A.F. Fagan, “Flow, noise and thrust of supersonic plug nozzles,” in AIAA SCITECH 2024 Forum, American Institute of Aeronautics and Astronautics. doi: 10.2514/6.2024-2305.
36. K.B.M.Q. Zaman, J.H. Korth, A.F. Fagan, and J. Bridges, “Study of a plug nozzle for supersonic aircraft concepts,” in 30th AIAA/CEAS Aeroacoustics 2024 Conference, in Aeroacoustics Conferences, 30th AIAA/CEAS Aeroacoustics 2024 Conference, 2024.
37. E.M. Greitzer, T.S. Tan, and M.B. Graf, Internal Flow: Concepts and Applications. in Cambridge Engine Technology Series, no. 3. Cambridge University Press, 2010. [Online]. Available: DOI: https://doi.org/10.1017/CBO9780511616709
38. J.S. Preisser, “Airframe Noise Measurements on a Supersonic Transport Small-Scale Model,” Journal of Aircraft, vol. 17, no. 11, pp. 795–801, Nov. 1980, doi: 10.2514/3.57967.
39. M.R. Khorrami and E. Fares, “Toward noise certification during design: airframe noise simulations for full-scale, complete aircraft,” CEAS Aeronaut J, vol. 10, no. 1, pp. 31–67, Mar. 2019, doi: 10.1007/s13272-019-00378-1.
40. R. Ferris, J. Appelbaum, and M.R. Khorrami, “Simulations of a Full-Scale Aircraft with Installed Airframe Noise Reduction Technologies,” in 2018 AIAA/CEAS Aeroacoustics Conference, Atlanta, Georgia: American Institute of Aeronautics and Astronautics, Jun. 2018. doi: 10.2514/6.2018-2974.
41. B.M. Duda, R. Ferris, and M.R. Khorrami, “Simulation-Based Assessment of a Full-Scale Installed Quiet Landing Gear,” in 25th AIAA/CEAS Aeroacoustics Conference, Delft, The Netherlands: American Institute of Aeronautics and Astronautics, May 2019. doi: 10.2514/6.2019-2476.
42. M.R. Khorrami, P.A. Ravetta, D.P. Lockard, B.M. Duda, and R. Ferris, “Comparison of Measured and Simulated Acoustic Signatures for a Full-Scale Aircraft with and without Airframe Noise Abatement,” in 2018 AIAA/CEAS Aeroacoustics Conference, Atlanta, Georgia: American Institute of Aeronautics and Astronautics, Jun. 2018. doi: 10.2514/6.2018-2975.
43. NASA, “Quesst: The Vehicle.” Accessed: May 14, 2024. [Online]. Available: https://www.nasa.gov/quesst-the-vehicle/
44. R. Ferris, M. Sacks, D. Cerizza, A. Ribeiro, and M. R. Khorrami, “Aeroacoustic Computations of a Generic Low Boom Concept in Landing Configuration: Part 1 - Aerodynamic Simulations,” in AIAA AVIATION 2021 FORUM, in AIAA AVIATION Forum, American Institute of Aeronautics and Astronautics, 2021. doi: 10.2514/6.2021-2195.
45. A.F. Ribeiro, R. Ferris, and M.R. Khorrami, “Aeroacoustic Computations of a Generic Low Boom Concept in Landing Configuration: Part 2 - Airframe Noise Simulations,” in AIAA AVIATION 2021 FORUM, in AIAA AVIATION Forum, American Institute of Aeronautics and Astronautics, 2021. doi: 10.2514/6.2021-2196.
46. M.R. Khorrami et al., “Aeroacoustic Computations of a Generic Low Boom Concept in Landing Configuration: Part 3 - Aerodynamic Validation and Noise Source Identification,” in AIAA

AVIATION 2021 FORUM, in AIAA AVIATION Forum, American Institute of Aeronautics and Astronautics, 2021. doi: 10.2514/6.2021-2197.
47. P.A. Ravetta, M.R. Khorrami, B. Konig, and E. Fares, "Multiplanar Synthetic Arrays and Their Application to Full-Scale Landing Gear Noise Source Identification," in AIAA AVIATION 2021 FORUM, American Institute of Aeronautics and Astronautics. doi: 10.2514/6.2021-2163.
48. M.R. Khorrami, W.M. Humphreys, D.P. Lockard, and P.A. Ravetta, "Aeroacoustic Evaluation of Flap and Landing Gear Noise Reduction Concepts," in 20th AIAA/CEAS Aeroacoustics Conference, Atlanta, GA: American Institute of Aeronautics and Astronautics, Jun. 2014. doi: 10.2514/6.2014-2478.
49. J.E.F. Williams and D.L. Hawkings, "Sound Generation by Turbulence and Surfaces in Arbitrary Motion," Philosophical Transactions of the Royal Society of London. Series A, Mathematical and Physical Sciences, vol. 264, no. 1151, pp. 321–342, 1969, Accessed: May 14, 2024. [Online]. Available: https://www.jstor.org/stable/73790
50. P. Sijtsma, "CLEAN Based on Spatial Source Coherence," International Journal of Aeroacoustics, vol. 6, no. 4, pp. 357–374, 2007, Accessed: May 14, 2024. [Online]. Available: https://doi.org/10.1260/147547207783359459
51. AVEC, "AVEC_software_brochure.pdf." Accessed: May 14, 2024. [Online]. Available: https://www.avec-engineering.com/resources/AVEC_software_brochure.pdf
52. M.R. Khorrami, W.M. Humphreys, and D.P. Lockard, "An Assessment of Flap and Main Landing Gear Noise Abatement Concepts," in 21st AIAA/CEAS Aeroacoustics Conference, Dallas, TX: American Institute of Aeronautics and Astronautics, Jun. 2015. doi: 10.2514/6.2015-2987.
53. J.J. Berton, D.L. Huff, K. Geiselhart, and J. Seidel, "Supersonic Technology Concept Aeroplanes for Environmental Studies," in AIAA Scitech 2020 Forum, American Institute of Aeronautics and Astronautics. doi: 10.2514/6.2020-0263.
54. A.A. Svetgoff, D.B. Stephens, and E. Envia, "Inlet Radiated Noise Predictions for the NASA Source Diagnostic Test Fan Using Physics-Based Simulations," in 28th AIAA/CEAS Aeroacoustics 2022 Conference, in Aeroacoustics Conferences. , 2022. Accessed: May 10, 2024. [Online]. Available: https://arc.aiaa.org/doi/abs/10.2514/6.2022-2941
55. R.T. Biedron et al., "FUN3D Manual: 13.7," NASA/TM-20205010139, Nov. 2020. Accessed: Apr. 11, 2025. [Online]. Available: https://ntrs.nasa.gov/citations/20205010139
56. E. Envia, "Prediction of Inlet Tone Noise From Two-Stage Fans," in 30th AIAA/CEAS Aeroacoustics Conference (2024), in Aeroacoustics Conferences, American Institute of Aeronautics and Astronautics, 2024. doi: 10.2514/6.2024-3388.
57. F.F.T., "ACTRAN VI 2022 User's Guide," Jan. 2022.
58. D. Stephens, A.A. Svetgoff, and E. Envia, "Acoustics of a Supersonic Mach 1.4 Axisymmetric Spike Inlet," in AIAA AVIATION 2023 Forum, American Institute of Aeronautics and Astronautics, 2023. doi: 10.2514/6.2023-3207.
59. R. Woodward, C. Hughes, R. Jeracki, and C. Miller, "Fan Noise Source Diagnostic Test – Far-field Acoustic Results," in 8th AIAA/CEAS Aeroacoustics Conference & Exhibit, American Institute of Aeronautics and Astronautics. doi: 10.2514/6.2002-2427.
60. E. Envia, "Fan Noise Source Diagnostics Test - Vane Unsteady Pressure Results," in 8th AIAA/CEAS Aeroacoustics Conference & Exhibit, Breckenridge, Colorado: American Institute of Aeronautics and Astronautics, Jun. 2002. doi: 10.2514/6.2002-2430.
61. J. Premo and J. Yu, "22" ADP Fan Rig Liners Design Report," 2022.

62. M.G. Jones and T.L. Parrott, “Evaluation of a Multi-point Method for Determining Acoustic Impedance,” Mechanical Systems and Signal Processing, vol. 3, no. 1, pp. 15–35, Jan. 1989, doi: 10.1016/0888-3270(89)90020-4.
63. M. Dahl, Assessment of NASA’s Aircraft Noise Prediction Capability. in NASA Technical Publication. NASA NTRS, 2012. [Online]. Available: https://ntrs.nasa.gov/citations/20120012957
64. M.G. Jones, W.R. Watson, D.M. Nark, B.M. Howerton, and M.C. Brown, “A Review of Acoustic Liner Experimental Characterization at NASA Langley.” Apr. 01, 2020. Accessed: May 10, 2024. [Online]. Available: https://ntrs.nasa.gov/citations/20200003112
65. A.A. Svetgoff and D. Stephens, “Validation of Noise Propagation for Lined Inlets,” in AIAA AVIATION 2023 Forum, American Institute of Aeronautics and Astronautics, 2023. doi: 10.2514/6.2023-3502.
66. D. Stephens, “Fan Noise for a Concept Commercial Supersonic Transport,” in 53rd AIAA/SAE/ASEE Joint Propulsion Conference, in AIAA Propulsion and Energy Forum, American Institute of Aeronautics and Astronautics, 2017. doi: 10.2514/6.2017-4635.
67. E. Envia, “Prediction of Inlet Tone Noise from Two-Stage Fans,” in 30th AIAA/CEAS Aeroacoustics 2024 Conference, in Aeroacoustics Conferences, American Institute of Aeronautics and Astronautics, 2024.
68. D.B. Stephens, Svetgoff Alexander A., and E. Envia, “Acoustic Simulations of Two-Stage Fans Behind a Supersonic Inlet,” in AIAA SciTech Forum 2025, American Institute of Aeronautics and Astronautics, 2025.
69. D.B. Stephens and A. A. Svetgoff, “Flow and Acoustics Simulations of a Supersonic Engine Inlet,” in 30th AIAA/CEAS Aeroacoustics 2024 Conference, in Aeroacoustics Conferences, American Institute of Aeronautics and Astronautics, 2024.
70. D.B. Stephens, “Noise Correction for Supersonic Inlet Geometry,” E-20048, Nov. 2022. Accessed: May 07, 2024. [Online]. Available: https://ntrs.nasa.gov/citations/20220007033
71. M.F. Heidmann, “Interim prediction method for fan and compressor source noise,” E-8398, Jun. 1975. Accessed: Dec. 21, 2021. [Online]. Available: https://ntrs.nasa.gov/citations/19750017876
72. J.W. Hough and D.S. Weir, “Aircraft Noise Prediction Program (ANOPP) Fan Noise Prediction for Small Engines,” NASA-CR-198300, Apr. 1996. Accessed: Dec. 21, 2021. [Online]. Available: https://ntrs.nasa.gov/citations/19960042711
73. B. Magliozzi, “V/STOL Rotary Propulsion Systems Noise Prediction and Reduction. Volume II-Graphical Prediction Methods.,” FAA-RD-76-49, II, May 1976. Accessed: May 14, 2024. [Online]. Available: https://apps.dtic.mil/sti/citations/ADA027389
74. C.C. Kiris, J.A. Housman, M.F. Barad, C. Brehm, E. Sozer, and S. Moini-Yekta, “Computational Framework for Launch, Ascent, and Vehicle Aerodynamics (LAVA),” Aerospace Science and Technology, vol. 55, pp. 189–219, Aug. 2016, doi: 10.1016/j.ast.2016.05.008.
75. S. Gottlieb and C.-W. Shu, “Total variation diminishing Runge-Kutta schemes,” Math. Comp., vol. 67, no. 221, pp. 73–85, 1998, doi: 10.1090/S0025-5718-98-00913-2.
76. J.A. Housman, G.-D. Stich, and C.C. Kiris, “Jet Noise Prediction using Hybrid RANS/LES with Structured Overset Grids,” in 23rd AIAA/CEAS Aeroacoustics Conference, Denver, Colorado: American Institute of Aeronautics and Astronautics, Jun. 2017. doi: 10.2514/6.2017-3213.
77. G.-D. Stich, J.A. Housman, J.G. Kocheemoolayil, C.C. Kiris, and J.E. Bridges, “Large-Eddy Simulation of Jet Surface Interaction Noise,” in 25th AIAA/CEAS Aeroacoustics Conference, in Aeroacoustics Conferences, Delft, The Netherlands: American Institute of Aeronautics and Astronautics, 2019. doi: 10.2514/6.2019-2475.

78. G.-D. Stich, J.A. Housman, A.S. Ghate, and C.C. Kiris, “Jet Noise Prediction with Large-Eddy Simulation for Chevron Nozzle Flows,” in AIAA Scitech 2021 Forum, in AIAA SciTech Forum, American Institute of Aeronautics and Astronautics, 2021. doi: 10.2514/6.2021-1185.
79. G.-D. Stich, A.S. Ghate, J.A. Housman, and C.C. Kiris, “Wall Modeled Large Eddy Simulations for NASA’s jet noise consensus database of single-stream, round, convergent jets,” in AIAA SCITECH 2022 Forum, American Institute of Aeronautics and Astronautics, 2022. doi: 10.2514/6.2022-0684.
80. G.-D. Stich, A.S. Ghate, J.A. Housman, and C.C. Kiris, “Wall-Modeled Large-Eddy Simulation of Jet Noise in Flight Conditions,” in 28th AIAA/CEAS Aeroacoustics 2022 Conference, Southampton, UK: American Institute of Aeronautics and Astronautics, Jun. 2022. doi: 10.2514/6.2022-3002.
81. C.A. Brown and J. Bridges, “Small Hot Jet Acoustic Rig Validation,” in NASA/TM-2006-214234, in NASA Technical Memo, 2006. Accessed: Oct. 11, 2018. [Online]. Available: https://ntrs.nasa.gov/search.jsp?R=20060013451
82. G.-D. Stich, C. Ashby, O. Martin, J.A. Housman, and J.C. Duensing, “Noise Prediction of Multi-Stream Internally Mixed Jets with External and Internal Plugs using Large-Eddy Simulation,” in 30th AIAA/CEAS Aeroacoustics 2024 Conference, in Aeroacoustics Conferences, American Institute of Aeronautics and Astronautics, 2024.
83. J. Bridges, M.P. Wernet, and G.G. Podboy, “Plug20 Test Report,” NASA Technical Memo NASA/TM—2021-10291, Mar. 2021. [Online]. Available: https://ntrs.nasa.gov/citations/20210010291
84. G.-D. Stich, O.G. Martin, C. Ashby, J.A. Housman, and J. Duensing, “Noise Prediction of Multi-Stream Internally Mixed Jets With External and Internal Plugs Using Large-Eddy Simulation,” in 30th AIAA/CEAS Aeroacoustics Conference (2024), American Institute of Aeronautics and Astronautics, 2024. doi: 10.2514/6.2024-3377.
85. V.G. Mengle and W.N. Dalton, “Lobed Mixer Design for Noise Suppression Vol 1,” in NASA/CR—2002-210823/VOL1, in NASA Contractor Reports, 2002.
86. V.G. Mengle and W.N. Dalton, “Lobed Mixer Design for Noise Suppression Vol 2,” in NASA/CR—2002-210823/VOL2, in NASA Contractor Reports, 2002.
87. L. Garrison, W. Dalton, A. Lyrintzis, and G. Blaisdell, “On the Development of Semi-Empirical Noise Models for the Prediction of the Noise from Jets with Forced Mixers,” in 10th AIAA/CEAS Aeroacoustics Conference, 0 vols., in Aeroacoustics Conferences, American Institute of Aeronautics and Astronautics, 2004. doi: 10.2514/6.2004-2898.
88. B. Tester and M. Fisher, “A contribution to the understanding and prediction of jet noise generation by forced mixers: Part III Applications,” in 12th AIAA/CEAS Aeroacoustics Conference (27th AIAA Aeroacoustics Conference), 0 vols., in Aeroacoustics Conferences, American Institute of Aeronautics and Astronautics, 2006. doi: 10.2514/6.2006-2542.
89. V. Mengle, “Anomalous effect of nozzle length reduction on jet noise of forced mixers,” in 5th AIAA/CEAS Aeroacoustics Conference and Exhibit, 0 vols., in Aeroacoustics Conferences, American Institute of Aeronautics and Astronautics, 1999. doi: 10.2514/6.1999-1968.
90. V. Mengle, “Anomalous effect of nozzle length reduction on jet noise of forced mixers,” in 5th AIAA/CEAS Aeroacoustics Conference and Exhibit, Bellevue, WA, U.S.A.: American Institute of Aeronautics and Astronautics, May 1999. doi: 10.2514/6.1999-1968.
91. B.S. Henderson, D.L. Huff, and J.J. Berton, “Jet Noise Prediction Comparisons with Scale Model Tests and Learjet Flyover Data,” in 25th AIAA/CEAS Aeroacoustics Conference, Delft, The Netherlands: American Institute of Aeronautics and Astronautics, May 2019. doi: 10.2514/6.2019-2768.

92. J. Fowler, D.K. Boyle, J. Revesz, and J. Cluts, “Use of an Uninhabited Aircraft System (UAS) for Atmospheric Observations During an Acoustic Flight Test,” in AIAA SCITECH 2024 Forum, American Institute of Aeronautics and Astronautics. doi: 10.2514/6.2024-0080.
93. B.S. Henderson and L.S. Hultgren, “Learjet 25D Jet Noise Flyover Measurements: Comparisons with Scale-Model Data,” in 30th AIAA/CEAS Aeroacoustics 2024 Conference, in Aeroacoustics Conferences, American Institute of Aeronautics and Astronautics, 2024.
94. L.S. Hultgren and B.S. Henderson, “Learjet 25D Jet-Noise Flyover Measurements: Uncertainty Analysis,” in 30th AIAA/CEAS Aeroacoustics 2024 Conference, in Aeroacoustics Conferences, American Institute of Aeronautics and Astronautics, 2024.
95. B.S. Henderson, “Single-Stream Empirical Jet-Noise Models Based on Scale-Model Data,” in AIAA SCITECH 2023 Forum, American Institute of Aeronautics and Astronautics, 2023. doi: 10.2514/6.2023-0022.
96. V. Mengle, “Finding excess noise in internally-mixed jets by varying free-jet speed,” in 5th AIAA/CEAS Aeroacoustics Conference and Exhibit, Bellevue, WA, U.S.A.: American Institute of Aeronautics and Astronautics, May 1999. doi: 10.2514/6.1999-1967.
97. A. Khavaran and J. Bridges, “Development of Jet Noise Power Spectral Laws Using SHJAR Data,” in 15th AIAA/CEAS Aeroacoustics Conference (30th AIAA Aeroacoustics Conference), 0 vols., in Aeroacoustics Conferences. , American Institute of Aeronautics and Astronautics, 2009. doi: 10.2514/6.2009-3378.
98. S. Martens, J. Morgenstern, and J. Bridges, “Supersonics N+2 System Validation Nozzle Test: GE Inverted Velocity Profile Nozzle Concept,” Oct. 18, 2011. Accessed: May 01, 2017. [Online]. Available: https://ntrs.nasa.gov/search.jsp?R=20150010383
99. J. Bridges, “Diagnosing Noise Features of Internally Mixed, External Plug Exhaust Systems,” in 2023 AIAA Aviation Forum, in 2023 AIAA Aviation Forum, San Diego, CA, U.S.A.: American Institute of Aeronautics and Astronautics, 2023.
100. J. Bridges, “Empirical noise modeling of internally mixed exhaust systems,” in 30th AIAA/CEAS Aeroacoustics 2024 Conference, in Aeroacoustics Conferences, 30th AIAA/CEAS Aeroacoustics 2024 Conference, 2024.
101. E. Envia, D. Huff, and C. Morrison, “Analytical assessment of stator sweep and lean in reducing rotor-stator tone noise,” in Aeroacoustics Conference, State College, PA, U.S.A.: American Institute of Aeronautics and Astronautics, May 1996. doi: 10.2514/6.1996-1791.
102. G.R. Busch and J.E. Bridges, “Reduction of Aircraft Noise Uncertainty for a Notional Supersonic Business Jet,” in AIAA SCITECH 2025 Forum, in AIAA SciTech Forum, American Institute of Aeronautics and Astronautics, 2025. doi: 10.2514/6.2025-1800.
103. A. Khavaran and J. Bridges, “SHJAR Jet Noise Data and Power Spectral Laws,” NASA TM, vol. 2009–215608, p. 63, 2009.